QUANTIFYING THE PROTECTIVE PROPERTIES AND ADHESION TO THE SUBSTRATE OF ULTRA-THIN MULTILAYER DIAMOND-LIKE CARBON COATINGS USING MOLECULAR DYNAMICS SIMULATION

by

Michael Robert Price

A dissertation submitted to the faculty of
The University of Utah
in partial fulfillment of the requirements for the degree of

Doctor of Philosophy

Department of Mechanical Engineering

The University of Utah

December 2017

The University of Utah Graduate School

STATEMENT OF DISSERTATION APPROVAL

The dissertation of **Michael Robert Price**

has been approved by the following supervisory committee members:

Bart Raeymaekers	, Chair	**July 17, 2017** Date Approved
Bruce K. Gale	, Member	**July 12, 2017** Date Approved
Meredith M. Metzger	, Member	**July 12, 2017** Date Approved
Valeria Lucero Molinero	, Member	**July 12, 2017** Date Approved
Ashley Spear	, Member	**July 12, 2017** Date Approved

and by **Timothy A. Ameel** , Chair/Dean of

the Department/College/School of **Mechanical Engineering**

and by David B. Kieda, Dean of The Graduate School.

ABSTRACT

Ultra-thin multilayer diamond-like carbon (DLC) coatings are used in precision engineering applications (including hard disk drives (HDDs)); their high hardness, chemical stability, and low friction coefficient in a range of environments allow protecting delicate substrate materials from damage, wear, and corrosion. A critical challenge when designing ultra-thin DLC coatings is understanding how they deform and delaminate from the substrate as a function of operating and coating design parameters including coating layer thickness and composition.

We use molecular dynamics simulations of the ultra-thin multilayer DLC coatings used in HDD recording heads, which consist of stacked layers of DLC and amorphous silicon (a-Si) on a Ni substrate, to quantify the effect of coating design parameters on the mechanical properties of the coating, plastic deformation of the substrate, and adhesion of the coating to the substrate. Based on the physical understanding gained from the simulations we derive design guidelines for ultra-thin multilayer DLC coatings.

We find that the hardness and Young's modulus of the coating increase with increasing DLC layer thickness and decreasing a-Si layer thickness because DLC and a-Si are the hardest and softest materials in the coating, respectively. We observe that plastic deformation of the Ni substrate for a constant mechanical load increases with increasing coating hardness because plastic deformation is increasingly preferential to the substrate with increasing coating hardness, causing the DLC coating to bend like a plate

into the plastically deformed substrate. We show that the presence of an intermediate a-Si layer is critical for improving adhesion of the DLC coating to the Ni substrate because bonding between Ni and DLC distorts the Ni lattice more than bonding between a-Si and Ni. Similarly, we observe that that an intermediate layer comprised of low sp^3-fraction DLC improves adhesion of high sp^3-fraction DLC to Si but not Ni substrates compared to coatings without an intermediate layer. For coatings with an intermediate a-Si layer, adhesion improves with decreasing a-Si layer thickness because less a-Si is present to plastically deform during loading, which displaces the coating failure region from the a-Si layer into the Ni substrate.

TABLE OF CONTENTS

Chapters

LIST OF FIGURES

LIST OF TABLES

LIST OF SYMBOLS

N_w	Number of windings in coil of wire
H_m	Magnetic field induced by coil of wire
I	Current in coil of wire
ℓ	Length of wire
M	Magnetization of ferromagnetic material
H_c	Coercivity of ferromagnetic material
N	Number of atoms in a system
V	Volume of a system of atoms
$\mathscr{E}$	Total energy of a system of atoms
T	Temperature of a system of atoms
i	Atom id
j	Atom id
k	Atom id
l	Atom id
m	Atom id
r_{ij}	Distance between two atoms i and j
f_c	Cutoff function for interatomic potential
r_1	Lower limit for cutoff function f_c
r_2	Upper limit for cutoff function f_c

U_{LJ}	Lennard-Jones potential energy function
U_{MORSE}	Morse potential energy function
U_{TOTAL}	Total pairwise energy in a system
U_{ij}	Pairwise energy between two atoms i and j
$U_{TERSOFF}$	Tersoff potential energy function
U_{AIREBO}	AIREBO potential energy function
U_{REBO}	REBO potential energy function
$U_{TORSION}$	4-body torsional term in U_{AIREBO}
U_{MEAM}	MEAM potential energy function
ε	Lennard-Jones parameter
σ	Lennard-Jones parameter
D	Morse parameter
α	Morse parameter
r_0	Morse parameter
f_R	Repulsive pair interaction function
f_A	Attractive pair interaction function
b_{ij}	Neighbor-dependent term between atoms i and j in $U_{TERSOFF}$
ζ	Three-body function in $U_{TERSOFF}$
g	Angular function in $U_{TERSOFF}$
θ_{ijk}	Angle formed by three atoms i, j, and k
n	Number of bonds an atom can form
$\bar{b}_{ij}$	Neighbor-dependent term between atoms i and j in U_{REBO}
F_i	Embedding energy function in U_{MEAM}

$\bar{\rho}_i$	Electron density of atom i in U_{MEAM}
ϕ_{ij}	Pairwise energy between atoms i and j in U_{MEAM}
t	Time
Δt	Time difference between time steps
$\mathbf{r}_\mathrm{i}$	Position of atom i
$\mathbf{v}_\mathrm{i}$	Velocity of atom i
$\mathbf{a}_\mathrm{i}$	Acceleration of atom i
F_{ij}	Force between two atoms i and j
m_i	Mass of atom i
d	Cartesian direction, one of x, y, or z
t_1	Thickness of top coating layer
t_2	Thickness of intermediate coating layer
t_{sub}	Thickness of substrate
r_{tip}	Indenter tip radius
h	Indentation depth
P	Indentation force
h_{max}	Indentation depth at the inception of unloading
P_{max}	Indentation force at the inception of unloading
S	Unloading stiffness during indentation
h_c	Contact depth during indentation
r_c	Contact radius between indenter tip and DLC surface
A	Contact area between indenter tip and DLC surface
C	Oliver-Pharr curve-fit parameter

h_f	Oliver-Pharr curve-fit parameter
m_f	Oliver-Pharr curve-fit parameter
H	Hardness
E	Young's modulus
d_i	Displacement of an atom
f_C	Size of plastic zone in DLC layer
f_{Si}	Size of plastic zone in Si layer
f_{Ni}	Size of plastic zone in Ni substrate
e_{ind}	Total indentation energy
e_{pl}	Plastic indentation energy
d_{pl}	Depth of permanent indentation depression
v_y	Velocity in y-direction
v_x	Velocity in x-direction
p_c	Contact pressure
Δl	Change in bond length between two atoms
l_0	Equilibrium bond length between two atoms
N_{bonds}	Total number of bonds in a grid element
N_T	Number of bonds of each bond type
E_T	Cohesive energy of each bond type
F_{max}	Maximum force during shear or tension simulation
t_{max}	Time at which F_{max} occurs
t_0	Time after equilibriation at which shear or tension load is applied
γ_{crit}	Critical mean shear strain during shear or tension simulation

Δt_{load}	Time between t_0 and t_{max}
l_x	Length of simulation box in x-direction
w_c	width of shear region
w_{cs}	width of critical shear region

LIST OF ABBREVIATIONS

HDD	Hard disk drive
HDI	Head/disk interface
MD	Molecular dynamics
DLC	Diamond-like carbon
a-C	Amorphous carbon
ta-C	Tetrahedral amorphous carbon
DLC:H	Hydrogenated diamond-like carbon
MR	Magneto-resistive
GMR	Giant magneto-resistive
TMR	Tunneling magneto-resistive
PVD	Physical vapor deposition
CVD	Chemical vapor deposition
FCVA	Filtered cathodic vacuum arc
DFT	Density functional theory
FCC	Face-centered cubic
RDF	Radial distribution function
ABRA	Atomic bond rotation angle

ACKNOWLEDGEMENTS

I would like to thank my wife Ginger for all her support and patience throughout grad school and for encouraging me to continue to work hard and achieve my graduate degree. I would also like to thank my parents, Ginger's parents, and both of our families for their support, encouragement, and understanding during grad school. I would also like to thank my grandparents and Ginger's grandmothers for their support and optimism in my behalf.

I would also like to thank my advisor Bart Raeymaekers for his teaching, mentoring, and helping me to think critically and communicate clearly both through writing and presenting, and for providing the direction and help necessary to successfully carry out this research project. I would also like to thank my lab mates for their support, friendship, and commiseration throughout the long hours and busy challenges of grad school.

I would also thank Western Digital Corporation for their support of this research. The support and resources from the Center for High Performance Computing at the University of Utah are gratefully acknowledged. This work used the Extreme Science and Engineering Discovery Environment (XSEDE), which is supported by National Science Foundation grant number ACI-1548562.

CHAPTER 1

INTRODUCTION

1.1 Problem statement

Diamond-like carbon (DLC) is often used as a coating to protect substrate materials against damage due to corrosion or contact with other moving bodies. The high hardness, low friction coefficient, and chemical stability of DLC in a range of environments provide superior protection against wear and corrosion compared to many materials [1]. Because of these desirable properties, DLC coatings are used in a wide range of engineering applications, including hard disk drives [2], internal combustion engines [3], razor blades [4], medical implants [5], and MEMS/NEMS devices [6]. However, the amorphous atomic structure of DLC leads to high intrinsic compressive stress that increases with increasing DLC thickness [7], which combined with its chemical inertness leads to poor adhesion between DLC and many substrate materials. Attempts to mitigate these problems by modifying the composition of the coating [8–12] or pre- and postprocessing of the substrate and coating [2,12–15] have been shown experimentally to improve adhesion of DLC coatings to a range of substrates, but can damage delicate substrate materials or change the mechanical properties of the coating such that their wear or corrosion resistance is reduced [2,8,9,12,14]. Changing the structure of the coating, such as by using a multilayer rather than single-layer DLC coating, has been shown to improve adhesion of DLC coatings to various substrates without damaging the substrate or degrading the protective properties of the DLC layer itself [16–18]. However, when the coatings are several nanometers thick or less, it becomes increasingly difficult to experimentally measure their wear and delamination and to quantify the deformation of the coating and substrate caused by external loading due to contact with another moving body. Thus, there is a lack of understanding of how coating design parameters, including thickness and composition, affect the ability of an ultra-thin multilayer DLC coating to protect the substrate from plastic deformation and to resist delamination from the substrate, which understanding is critical for their design.

Hence, **the research objective of this dissertation** is to test the hypothesis that the protective properties of ultra-thin multilayer DLC coatings, including their ability to prevent plastic deformation of the substrate and their adhesion to the substrate, can be improved by tuning the design parameters of the coating. This will be achieved by quantifying the mechanical properties of the coating, quantifying the deformation of the coating and substrate due to combined normal and tangential loading, and quantifying adhesion of the coating during normal, tangential, and combined normal and tangential loading as a function of coating layer thickness and composition. We focus on the ultra-thin DLC coatings used in hard disk drives (HDDs), a practical application with a need for greater understanding of the protective properties of these coatings as a function of their design parameters. However, the results are not limited to this application and will help in the design of DLC coatings in a wide range of applications for which they are used.

1.2 Magnetic storage technologies

1.2.1 Industry background and motivation

Magnetic recording is based on the principles of electromagnetic induction and magnetic hysteresis, in which an electric current is converted into a magnetic field via a coiled wire and the resulting magnetic field magnetizes a ferromagnetic material according to a specified pattern. Figure 1.1 shows a length of wire coiled into N_w

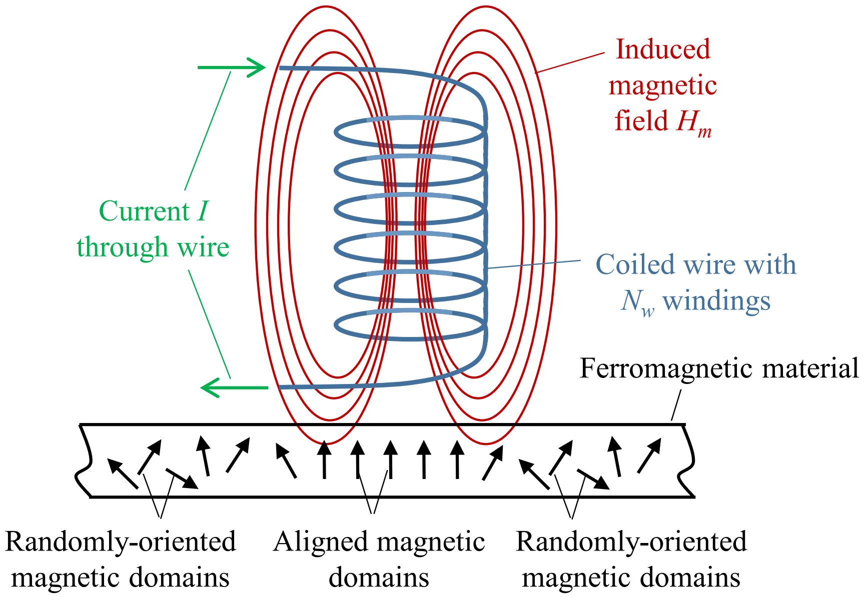

Figure 1.1 Length of coiled wire with N_w windings that induces a magnetic field of strength H_m when a current I is applied through the wire, placed near a ferromagnetic material.

windings that induces a magnetic field of strength H_m when a current I is applied through the wire, placed near a ferromagnetic material. The strength of the magnetic field induced by the wire depends on the number of windings N_w, the current I, and the length of the wire ℓ, as $H_m = N_w I/\ell$. The magnetic field magnetizes the ferromagnetic material by aligning the material's individual magnetic domains with the external magnetic field H_m. The degree of alignment, and thus, the resulting residual magnetization of the material, depends on the magnitude of the magnetic field H_m, the distance between the coil of wire and the magnetic material, and the previous orientation of the magnetic domains. The phenomenon in which a material's magnetization depends on its previous state is known as magnetic hysteresis. Figure 1.2 shows a magnetic hysteresis loop for the magnetization of a ferromagnetic material M as a function of the applied magnetic field H_m. At point A before an external magnetic field has been applied, the magnetic domains of the

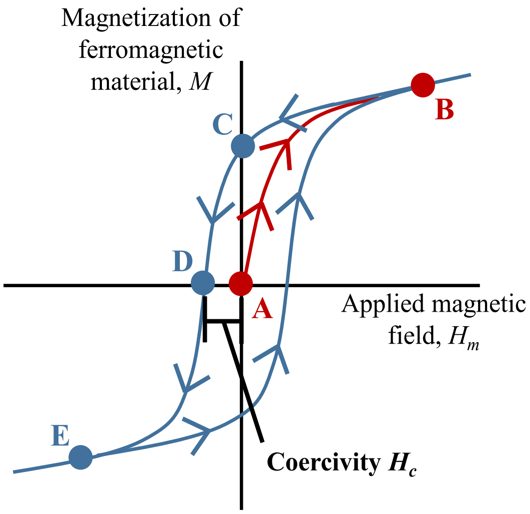

Figure 1.2 Magnetic hysteresis loop with the magnetization of a ferromagnetic material M as a function of the applied magnetic field H_m.

ferromagnetic material are randomly oriented, resulting in zero net magnetization. If an external magnetic field is applied, the magnetization follows the red curve and approaches point B with increasing H_m, at which point the ferromagnetic material has reached saturation and all available magnetic domains are aligned with the applied field. However, if the external magnetic field is then reduced, the magnetization of the ferromagnetic material follows a different (blue) path to point C. At this point, there is no external magnetic field ($H_m = 0$), but the ferromagnetic material remains magnetized ($M \neq 0$). In order to remove the magnetization of the material (point D), an opposite magnetic field must be applied of magnitude H_c, known as the material's coercivity, beyond which any further decrease in H_m towards point E again results in residual magnetization of the ferromagnetic material. Hence, for any value of H_m between points E and B the magnetization of the ferromagnetic material depends on the previous state of the material in addition to H_m. It is this phenomenon that allows one to magnetize a ferromagnetic material, or a region thereof, and recall that magnetization at a later point even in the absence of a continually applied external magnetic field. The possibility of using this property of magnetic materials to record audio was first suggested in 1888 by Oberlin Smith [19]. However, he did not succeed in actually creating a magnetic recording device, which was first achieved in 1899 by Valdemar Poulsen with the invention of the telegraphone [20]. Figure 1.3 (a) shows Oberlin Smith and Valdemar Poulsen and Figure 1.3 (b) shows a schematic of the key components of the telegraphone, reproduced from [19]. In a telegraphone, an electrical audio signal is converted into a fluctuating magnetic field through electromagnetic induction in a coil of wire, also referred to as the recording head (E in Figure 1.3 (b)), as shown in Figure 1.1. This

Oberlin Smith   Valdemar Poulsen

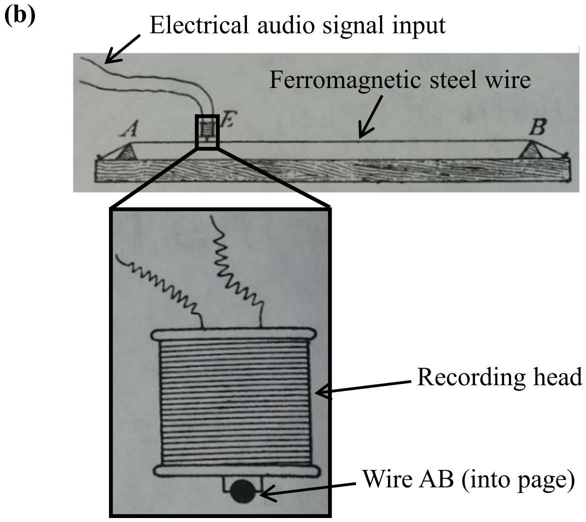

Figure 1.3 Invention of the telegraphone. (a) Oberlin Smith and Valdemar Poulsen, inventors of magnetic recording and (b) schematic of the key components of the telegraphone. Reproduced from [19].

fluctuating magnetic field magnetizes a ferromagnetic steel wire (AB in Figure 1.3 (b)), with varying magnitude and polarity, as the recording head is moved along the steel wire, thus storing a nonvolatile representation of the audio signal. The audio signal can be retrieved by moving the recording head back along the magnetized wire in the absence of a driving electrical signal, which thus inductively re-creates the original electrical audio signal from the magnetized wire. Magnetic wire recorders were popular through the mid-1950s, when tape recorders had become commercially viable on a large scale [19]. Figure 1.4 shows a schematic of a typical tape drive (see, e.g., [21]), including the supply and take-up reels for holding the magnetic tape before and after reading or writing, respectively, the recording head for reading and writing data, tension control and tension measuring rollers that ensure the desired tension in the tape as it is fed past the recording head, and the capstan and pinch roller that control the speed of the tape. Tape recorders use the same magnetic phenomena that wire recorders use for recording audio signals but differ in the medium used to store them, which for tape recorders consists of a layer of

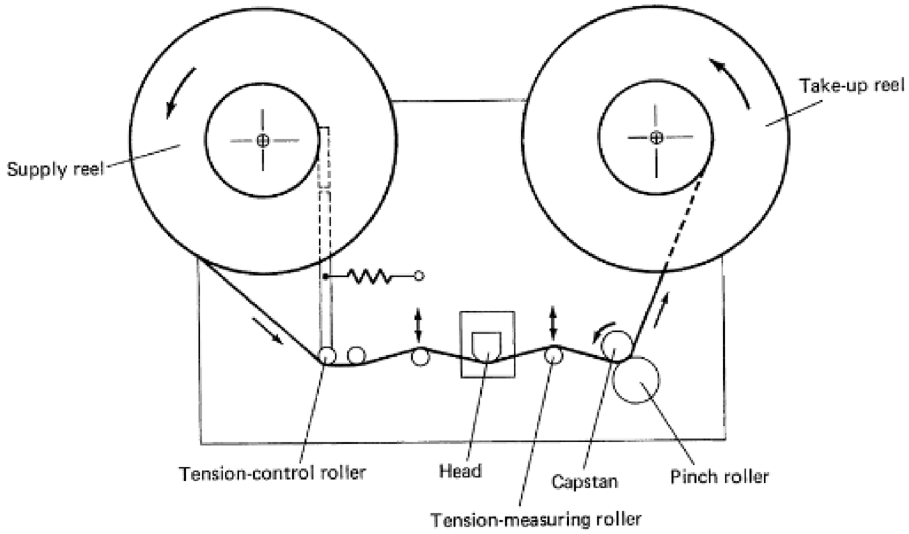

Figure 1.4 Schematic of a magnetic tape drive.

magnetic material bonded to flexible plastic tape [19]. Magnetic tape recorders largely replaced magnetic wire recorders due to the lower cost and lower chance of twisting or tangling of magnetic tape compared to magnetic wire [19,22]. Furthermore, a key advantage of magnetic tape over steel wire is the ability to optimize the magnetic properties of the recording medium independent of the mechanical properties of the tape [19]. Optimizations of the magnetic recording medium as well as developments such as digital audio and data recording, multiple-track magnetic tape, modifications to the types of mechanical, electrical, or optical components used to control tension in the tape, improved signal processing algorithms, and magneto-resistive (MR) and giant-MR (GMR) read elements continued throughout the remainder of the 20th century and continue today [21,23,24]. These developments are driven primarily by a desire for greater storage density (bytes/in^2 or bytes/in^3), cheaper data storage (bytes/dollar), and faster data access (bytes/second). Although magnetic tape recording has shown exponential improvement in storage density and cost [25], data access times are inherently limited for magnetic tape drives by the sequential nature of storing and retrieving data on spooled reels. Thus, the need for faster, and in particular, continuous random access to data led to the development of the HDD in 1956 with the introduction of the IBM RAMAC [26].

1.2.2 Hard disk drives

The fundamental magnetic phenomena used for storing and retrieving data are similar in an HDD compared to magnetic tape recording devices, but differ primarily in the use of a rigid disk rather than flexible tape to which the magnetic recording layer is bonded and, consequently, in the mechanical components necessary for controlling the motion of the disk and the magnetic read/write components when reading and writing the desired data. Figure 1.5 shows a schematic of an HDD, including the magnetic disks, spindle, suspension arm with attached read/write head, voice-coil actuator, signal processing and controls electronics, and enclosure. Digital data are stored in circumferential tracks along the top and bottom surfaces of the magnetic disk, which consists of a magnetic material on an aluminum or glass substrate [20]. Multiple magnetic disks are stacked on the spindle to increase data storage capacity. When reading or writing data, the spindle spins the magnetic disks at a velocity of 5,400-15,000 rpm [20,26], the voice-coil actuator moves the suspension arm above (below) the desired circumferential data track on the top (bottom) of the disk, and data is transduced using the read/write head as described previously for magnetic wire recording. Writing data to the disk is achieved by using inductive coils that magnetize distinct regions, or domains, of the disk. However, unlike the first magnetic recording devices, HDDs store data digitally, with the polarity of each magnetized domain representing one data bit, and thus, increasing data density of HDDs requires decreasing the size of these magnetized

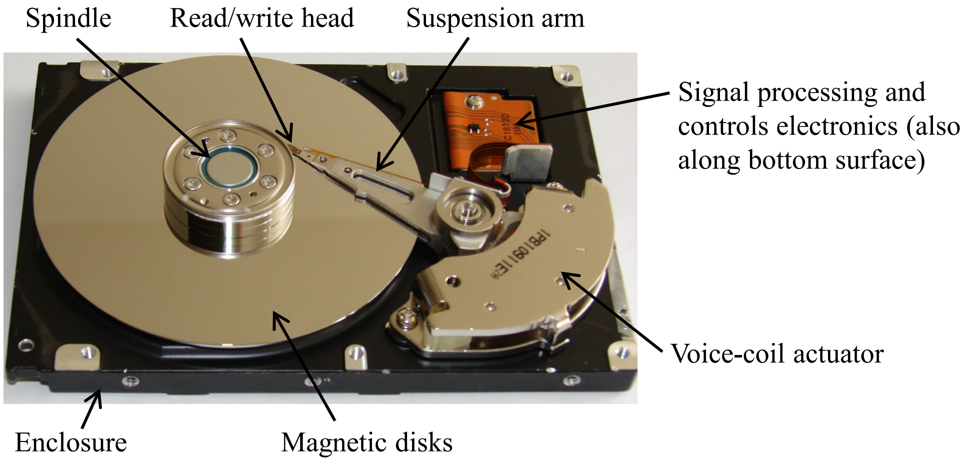

Figure 1.5 Schematic of an HDD. Modified from the public-domain image https://commons.wikimedia.org/wiki/File:01b-hard-drive-cover-removed.JPG.

domains. This has dictated much of the evolution in HDD design since they were first introduced in 1956, in part because decreasing the size of the magnetic domain decreases the strength of the magnetic field it creates when it has been magnetized, and thus makes it increasingly difficult to read and write the data to and from the disk. Evolutionary developments in the inductive coil technology of read/write heads helped compensate for this until the early 1990s, at which point fundamental limits in the ability to inductively determine the polarity of the magnetic domains on the disk led to the implementation of MR read elements in HDDs [20]. GMR read elements and tunneling-MR (TMR) read elements followed in subsequent decades [19,20]. Further decreases in bit size were achieved in the mid-2000s by changing the orientation of the magnetic moments of the bits on the disk from horizontal to perpendicular with respect to the surface of the disk [20,27]. Challenges with the persistence of the magnetization of the domains, and thus, with the data stored on magnetic disks, also occur with decreasing domain size, which have led to the use of magnetic materials with increasing magnetic coercivity on the disk [20]. However, as the size of the magnetic domains on the disk decreases further, the materials approach the superparamagnetic limit, below which the polarity of the domains may spontaneously reverse, destroying the data stored in the HDD. Therefore, current research in HDD technology aims to push the effect of the superparamagnetic limit to increasingly smaller magnetic domains through the implementation of read/write heads that locally and temporarily heat the disk and thus lower its coercivity during writing (heat-assisted magnetic recording) or by physically patterning the magnetic disk with pre-defined magnetic islands (bit-patterned media) [20,27].

1.2.3 Protection of HDD recording heads

The challenges associated with decreasing the size of magnetic domains on the disk have not been solved through changes in read/write head and magnetic disk technologies alone, but have also required decreasing the spacing between the head and the disk. Figure 1.6 shows a schematic of the head/disk interface (HDI) in an HDD. The disk is comprised of a magnetic layer on a substrate covered with a DLC layer and lubricant (sub)mono-layer to protect against corrosion of the delicate magnetic materials and against accidental contact with the recording head during read and write operations. The recording head is comprised of the magnetic read/write components including the write coils, GMR element, top pole, and magnetic NiFe shields on an alumina substrate. A protective DLC coating is also used on the recording head, which consists of a DLC layer and an amorphous Si (a-Si) layer that improves adhesion between the DLC layer and the magnetic materials and substrate of the recording head. The distance between the outermost surfaces of the head and disk is the flying height. The distance between the magnetic read/write components of the head and the magnetic layer of the disk is the magnetic spacing. Decreasing the magnetic spacing between the magnetic read/write components of the head and magnetic layer of the disk improves their magnetic coupling,

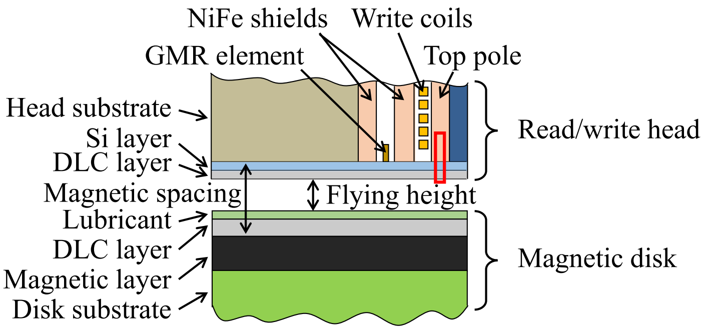

Figure 1.6 Schematic of the head/disk interface in an HDD.

requiring less energy for the write coils on the head to magnetize the magnetic domains on the disk when writing data and making the read element on the head more sensitive to the polarity of the magnetic domains on the disk when reading data. However, decreasing the magnetic spacing requires decreasing both the flying height and the thickness of the protective DLC coatings on the head and disk. The flying height decreased from 20 μm in the 1956 IBM RAMAC to 1-2 nm in today's state-of-the-art HDDs [26,28,29], and the protective DLC coatings, which have been used in HDDs since the 1990s, are less than 2 nm thick in state-of-the-art HDDs [30–32]. The likelihood of contact between the head and the disk increases with decreasing flying height, and the likelihood of coating removal and thus, damage to the magnetic components of the head and disk due to wear or corrosion, increases with decreasing coating thickness. Experimental results show that damage due to contact between the head and disk occurs primarily on the recording head near the top pole [33,34], including the region indicated by the red box in Figure 1.6, thus, one focus of current HDD research is how to design increasingly thinner DLC coatings for the recording head that remain intact due to accidental contact with the disk and that are able to protect the delicate magnetic components beneath them throughout the lifetime of an HDD.

1.3 DLC coatings

1.3.1 Diamond-like carbon (DLC)

Carbon forms multiple allotropes including diamond, graphite, fullerenes, nanotubes, graphene, glassy carbon, and DLC, which differ not in chemical composition but in their atomic structure, i.e., in the physical arrangement of their constituent carbon atoms and the types of carbon-carbon bonds that form between them [35]. Figure 1.7

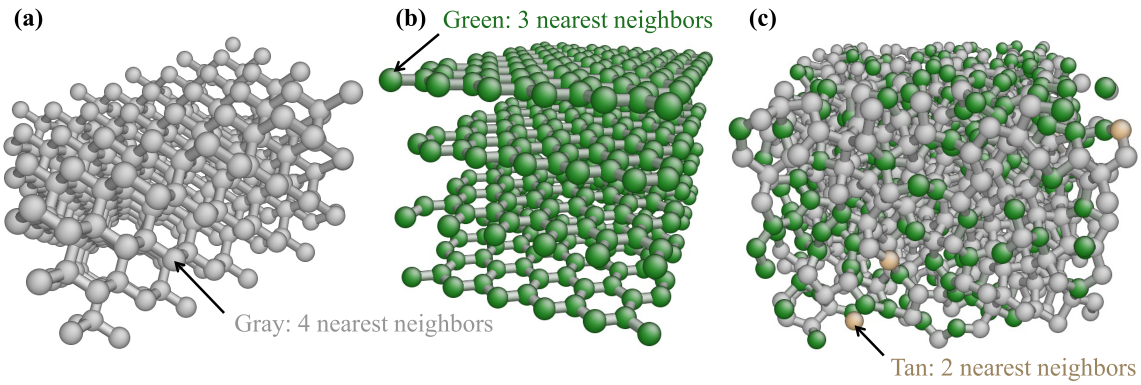

Figure 1.7 Atomic structure of three carbon allotropes. These include (a) diamond, (b) graphite, and (c) DLC.

shows the atomic structure of diamond and graphite, the most common allotropes of carbon, and DLC, the overcoat material used on HDD recording heads. Four-coordinated, three-coordinated, and two-coordinated carbon atoms are shown as gray, green, and tan, respectively. Diamond is comprised of a diamond cubic arrangement of carbon atoms that form sp^3-hybridized bonds with the four nearest-neighbor carbon atoms (Figure 1.7 (a)). Graphite is comprised of sheets of hexagonally-bonded carbon atoms that form sp^2-hybridized bonds with three nearest-neighbor carbon atoms (Figure 1.7 (b)). Despite their equivalent chemical composition, the properties of diamond and graphite such as their chemical, optical, mechanical, and tribological properties are different and span those of many common engineering materials. For example, diamond is the hardest naturally-occurring material, displaying a hardness of approximately 100 GPa [36], whereas graphite has a hardness of less than 1 GPa [37]. However, when sliding over another material, graphite may have a lower coefficient of friction than that of diamond [38–40]. Alternatively, diamond-like carbon (DLC) is a form of carbon in which the atomic structure is amorphous and the carbon atoms form a mixture of sp, sp^2, and sp^3-hybridized bonds (Figure 1.7 (c)). Its mechanical properties are intermediate between those of diamond and graphite, and vary depending on the fraction of sp^3-hybridized carbon-carbon bonds and the amount of hydrogen and/or other dopants in the material. Like diamond, DLC is chemically stable in a range of environments, although analogous to its mechanical properties, its chemical properties vary according to its composition, including sp^3 fraction, hydrogen content, and other dopants. The sp^3 fraction, hydrogen content, and other dopants in a DLC coating depend on the deposition technique and can be controlled by tuning the parameters of the deposition process. Many deposition processes have been implemented since the first DLC coatings were described in the 1950s. DLC coatings did not gain much attention until the 1970s, and began to be used in large-scale industrial and manufacturing applications in the mid-1980s [35]. The development of DLC deposition technology led to the implementation of various physical vapor deposition (PVD) and chemical vapor deposition (CVD) techniques including plasma-enhanced CVD (PECVD) [41], ion-beam deposition [42], sputtering [43], filtered cathodic vacuum arc (FCVA) [44], and pulsed laser deposition (PLD) [45]. Chemical deposition techniques function by decomposing a hydrocarbon precursor gas, and typically form DLC coatings that contain hydrogen (DLC:H). Physical deposition techniques typically involve vaporizing material from a solid target, such as graphite, and can form hydrogen-free DLC films if the target material is hydrogen-free. Deposition parameters can be varied to control the sp^3 fraction within a range that depends on the deposition technique. Sputtering, for example, cannot provide as high an sp^3 fraction as FCVA or PLD, which have been used to create DLC films with greater than 80% sp^3 fraction [9]. Films with low to intermediate sp^3 fraction (< 40-50%) are referred to as amorphous carbon (a-C) and those with a larger sp^3 fraction are known as tetrahedral amorphous carbon (ta-C), although no standardized usage exists, and the terms DLC, a-C, and ta-C are often used differently by different authors [46]. ta-C has properties that approach those of diamond, whereas a-C is more graphite-like. If hydrogen is present the films are classified as DLC:H, or a-C:H and ta-C:H depending on sp^3 fraction. Other dopants such as Ti, B, S, Si, Cr, F, W, N, or O [1,6] can be included in the deposition process and change the properties of the resulting DLC film. These dopants can be used to decrease the friction coefficient [47], decrease the intrinsic compressive stresses [7], or improve adhesion between DLC and the substrate [48]. However, their inclusion can negate other beneficial properties of DLC coatings, including reducing the hardness of the DLC coating [7].

1.3.2 Use of DLC as a protective coating

Because of the tunability of the mechanical and chemical properties of DLC and the corresponding range of tribological benefits such as low friction, low wear rates, and corrosion resistance that they provide in a range of environments, they are used as protective coatings in many engineering applications [6,35]. For example, DLC coatings are used to coat automobile engine components to reduce friction and increase maximum load carrying capacity of gears [3], in articulating knee and hip implants to reduce wear and corrosion in artificial joint implants [5], in beverage containers to decrease their permeability [46], on razor blades to decrease friction and improve their longevity [35], and in HDD recording heads and magnetic disks to prevent wear and corrosion as discussed in section 1.2.3 [49]. However, challenges exist that limit the effectiveness of DLC coatings or preclude their use in many applications because of high residual compressive stress due to the deposition process. This residual stress increases with increasing sp^3 fraction and increasing coating thickness, and leads to cracking, brittle fracture, and delamination of DLC coatings [1,6]. Furthermore, the chemical stability that prevents corrosion of DLC coatings in many environments also prevents strong bonding between DLC coatings and many substrates. Thus, an intermediate layer comprised of a material that bonds well to both DLC and the substrate material is often used to improve adhesion between a DLC coating and its substrate. However, it is difficult to predict and measure how multilayer DLC coatings deform under external loading and thus, how coating design parameters such as composition and thickness affect its resistance to separation from the substrate due to the external loading. These difficulties increase with decreasing coating thickness, particularly when the coating is less than several nanometers thick and deformation of the coating is dominated by atomic-scale effects. Hence, researchers have turned to atomic-scale modeling techniques to understand the behavior of ultra-thin DLC coatings under external loading.

1.4 Molecular dynamics

1.4.1 Overview of molecular dynamics

Molecular dynamics (MD) is an atomic-scale, stochastic modeling technique in which individual atoms are represented as classical particles that behave according to Newton’s laws of motion. Thus, MD is used to calculate trajectories of each atom as the system evolves over time, and is therefore better suited for simulating dynamic events such as external loading of DLC coatings than are other simplified atomistic approaches such as Monte Carlo simulations that do not explicitly include a measure of time. Furthermore, the simplified classical approach used in MD simulations can be used to simulate larger and more complex systems than can be simulated using more accurate quantum mechanical approaches such as density functional theory (DFT). Although the classical approximation of the atom used with MD does not account for quantum phenomena, many of these phenomena, such as bonding between atoms, can be accurately modeled through the use of appropriately-selected interatomic potentials. Furthermore, the discipline of statistical mechanics provides a framework for justifying the representation of atoms as classical particles by showing the relationship between a system's available quantum states and that system's thermodynamic properties that is valid for a wide range of systems (see, e.g., [50,51]).

1.4.2 Thermodynamics and statistical mechanics

Statistical mechanics is based on the quantum-mechanical understanding that energy is quantized rather than continuous, and that therefore, only certain quantum states are available to a given system. The total number of available states increases with increasing system energy and with increasing system complexity, i.e., with increasing number of atoms and increasing interactions between them. Owing to the difficulty in solving the Schrödinger equation for many-body systems, it is currently impossible to model or describe every quantum state for any but the simplest systems. This is especially true for macroscopic systems, in which the number of atoms is of the order of 10^{23} and the number of interactions between them and thus, the number of quantum states available, is exponentially larger. Indeed, the number of states available to even a system of noninteracting particles for all but its lowest energy levels is on the order of 10^N, where N is the number of particles in the system [50]. However, many macroscopic systems can be fully characterized with only a few thermodynamic variables such as temperature, pressure, and volume. The seeming discrepancy between the more than 10^N

different quantum states available to a system and the relatively few thermodynamic variables necessary to characterize that system can be reconciled statistically using the theoretical construct of an ensemble. Just as a system is a collection of particles, an ensemble is a collection of systems, in which each system has identical thermodynamic properties but a different quantum state compared to the other systems in the ensemble. Figure 1.8 shows a representation of an ensemble of systems in which every system has equal number of atoms *N*, volume *V*, and energy $\mathscr{E}$ (in arbitrary units) but different distributions of that energy within each system. The total number of systems in the ensemble is equal to the number of quantum states available to the original system upon which the ensemble is based, and each available state is represented by a different system within the ensemble. Using the fact that an ensemble can be made arbitrarily large by

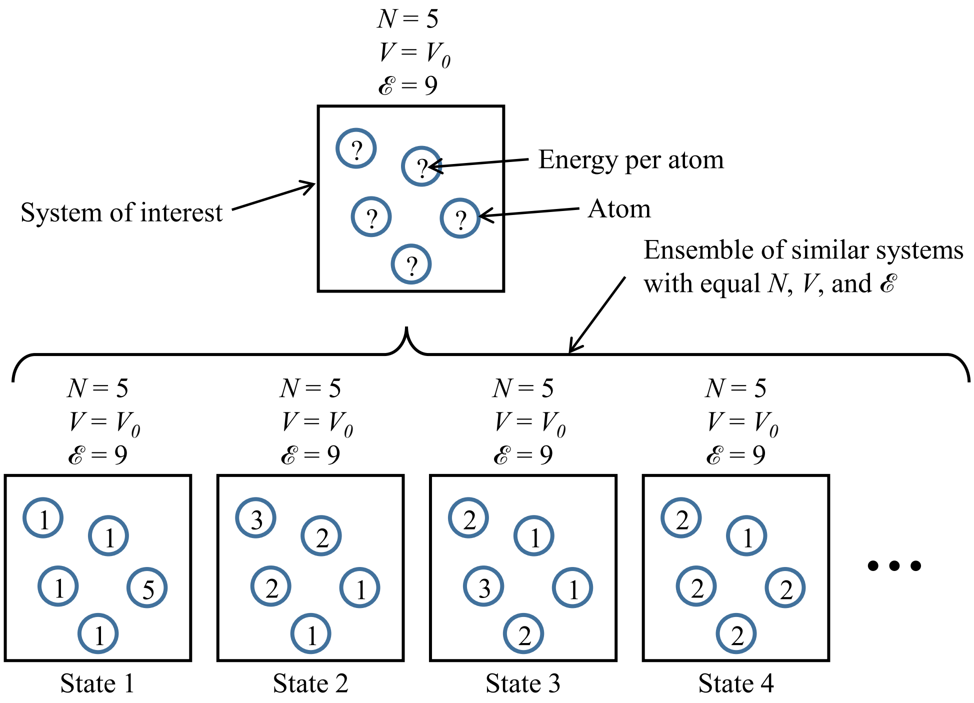

Figure 1.8 Ensemble of systems with equal number of atoms *N*, volume *V*, and energy $\mathscr{E}$ (in arbitrary units) but different distributions of that energy within each system.

scaling the size of the size of its constituent systems, and the fact that certain statistical relations can be greatly simplified for large systems, one can calculate the distribution of quantum states in the ensemble, including which states are most likely and which states have a negligible effect on the thermodynamic properties of the system, e.g., which energy distributions are statistically unlikely to ever occur. The information contained in the probability distribution of a system's quantum states is known as the system's partition function, and provides the link between a system's quantum states and its macroscopic thermodynamic properties. The partition function is directly related to a subset of the system's thermodynamic properties according to the boundary conditions specified for the systems that comprise the ensemble, and thus, it is possible to construct different ensembles depending on which thermodynamic properties are most useful for a given application. For example, the ensemble in which the number of atoms N, volume V, and energy $\mathcal{E}$ are specified is the microcanonical or $NV\mathcal{E}$ ensemble, and the ensemble in which the number of atoms N, volume V, and temperature T of the constituent systems are specified is the canonical or NVT ensemble. Furthermore, with a knowledge of the partition function for a given system, any mechanical or thermodynamic property of a system can be related to its available quantum states [50]. Hence, one can model the thermodynamic and mechanical properties of a system in accordance with its quantum behavior so long as these relationships are not violated. However, even with such a relationship defined between a system's quantum states and its macroscopic properties, calculating the actual properties of interest requires the solution of the N-body Schrödinger equation of the system unless an accurate simplification of the atomic interactions can be found. For many atomistic simulation techniques, including MD, this simplification takes the form of interatomic potentials.

1.4.3 Interatomic potentials

Interatomic potentials are functions that describe atoms and their interactions as classical particles in a potential energy field. Types of available interatomic potentials range from simple, two-body potentials in which the energy between two atoms depends only on the distance between them, to more complex many-body potentials in which the energy between two atoms changes as a function of distance between them, the number and type of additional neighboring atoms, the angles between all nearest-atom pairs, the rotation of the atoms about the axis between them, or their electric charge. Figure 1.9 shows the potential energy U_{LJ} or U_{MORSE} between two atoms calculated using the Lennard-Jones potential or Morse potential, respectively, two commonly used two-body potentials, as a function of the distance $\boldsymbol{r}_{ij}$ between two atoms i and j. These functions take the following forms:

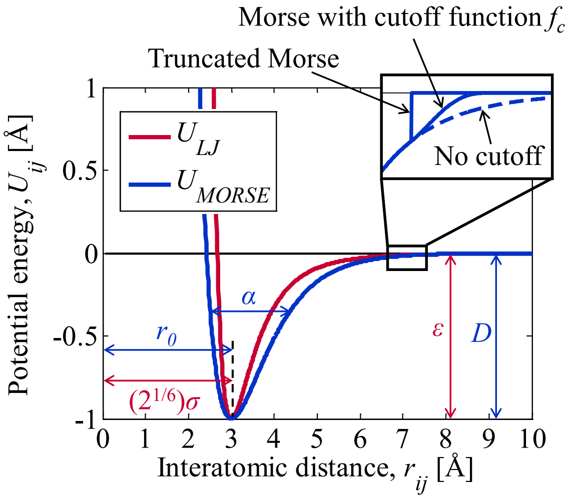

Figure 1.9 Potential energy U_{LJ} or U_{MORSE} between two atoms calculated using the Lennard-Jones potential or Morse potential, respectively, as a function of the distance $\boldsymbol{r}_{ij}$ between two atoms i and j.

$$U_{LJ}(r_{ij}) = 4\varepsilon\left[\left(\frac{\sigma}{r_{ij}}\right)^{12} - \left(\frac{\sigma}{r_{ij}}\right)^{6}\right], \quad (1.1)$$

$$U_{MORSE}(r_{ij}) = D\left[e^{-2\alpha\left(r_{ij}-r_0\right)} - 2e^{-\alpha\left(r_{ij}-r_0\right)}\right], \quad (1.2)$$

where U_{LJ} or U_{MORSE} is the potential energy between atoms i and j, and ε, σ, D, α, and r_0 are tunable parameters that depend on the particular material being modeled. The energy between two atoms is negligible at large r_{ij}, but becomes increasingly negative, or attractive, with decreasing r_{ij} until reaching a minimum at the equilibrium distance, which corresponds to the equilibrium bond length for a pair of atoms. Thus, although no interatomic bonds are explicitly modeled, two atoms can be considered to be bonded when the distance between them is approximately equal to their equilibrium bond length [52]. The interatomic energy increases exponentially with decreasing r_{ij} when it is less than the equilibrium bond length, which represents the high repulsive forces that exist between the nuclei of two atoms at small distances. The total pairwise potential energy U_{TOTAL} in the system is a summation of the pairwise energy U_{ij} between each pair of atoms i and j:

$$U_{TOTAL} = \frac{1}{2}\sum_{i}\sum_{j\neq i} U_{ij}\ , \quad (1.3)$$

where U_{ij} is the pairwise energy from, e.g., the Lennard-Jones or Morse potential, $U_{ij} = U_{LJ}$ or $U_{ij} = U_{MORSE}$. Often, because the interaction energy between two atoms is negligible when their distance is large (e.g., $r_{ij} \approx 7\sigma$ for U_{LJ}), the interatomic potentials are cut off beyond a specified value of r_{ij} to limit the number of calculations that must be performed in large systems. This cutoff is preferably implemented over a range of r_{ij} to prevent a discontinuous jump in the potential energy function caused by a simple truncation of the potential energy function, as shown in the inset of Figure 1.8, and is implemented by multiplying the interatomic potential function U_{LJ} or U_{MORSE} by a cutoff function f_C that transitions smoothly from 1 to 0 over a desired range of r_{ij}, such as:

$$f_C(r_{ij}) = \begin{cases} 1 & r_{ij} < r_1 \\ \frac{1}{2} + \frac{1}{2}\cos\left[\pi\left(\frac{r_{ij} - r_1}{r_2 - r_1}\right)\right] & r_1 \le r_{ij} \le r_2\,, \\ 0 & r_{ij} > r_2 \end{cases} \tag{1.4}$$

where r_1 and r_2 are the lower and upper limits of the desired cutoff region. Two-body interatomic potentials such as U_{LJ} and U_{MORSE} are less accurate representations of the actual interactions between two atoms than more complex, many-body interatomic potentials, but are often used because of their computational simplicity and thus, their ability to model large systems efficiently. However, their limited accuracy, in particular their inability to account for an atom's local bonding environment and their lack of angular forces that control bond angles, limits the types of materials and atomic phenomena they can model to cases such as simple gases, close-packed crystalline solids, or some surface phenomena. Angular forces and local bond environment are important for modeling open atomic structures, i.e., those with a high fraction of empty space, such as carbon-based or other diamond-cubic materials, including the DLC and a-Si layers that comprise the coating of an HDD recording head. Interatomic potentials with these bond environment and angular terms include the Tersoff [53], AIREBO [54], and modified embedded atom method (MEAM) potentials [55]. Their shape is similar to the functions shown in Figure 1.9 for two isolated atoms or between two atoms in equilibrium. However, bond-environment screening functions and angular terms affect the magnitude of the interaction energy between an atom and any nearby atoms such that the interaction energy between an atom and its neighbors is minimized for all neighbors except the n closest atoms with which the atom can form the desired bond angles, where n is the number of bonds the atom can form. For example, the Tersoff potential is used primarily for modeling C, Si, and Ge, and therefore is parameterized to favor tetrahedral and trigonal bonding, in which each atom bonds with three or four nearest neighbors. It takes the following form:

$$U_{TERSOFF}(r_{ij}) = f_C(r_{ij})\left[f_R(r_{ij}) + b_{ij} f_A(r_{ij})\right], \quad b_{ij} = \zeta\left(\sum_{k\neq i,j} g\left(\theta_{ijk}\right)\right), \tag{1.5}$$

where f_R and f_A are the repulsive and attractive components of the pairwise interactions, respectively, and f_C is a cutoff function (see Equation 1.4). Like the two terms that comprise the Morse potential (Equation 1.2), f_R and f_A take the form of an exponential, and thus the b_{ij} term is the primary difference between the Tersoff and Morse potentials. b_{ij} is a function of the angles θ_{ijk} formed by an atom i, its neighbor j, and each remaining nearby atom k, and thus, is an angular term that reduces the magnitude of the attractive pairwise component of the energy f_A for atom pairs that do not form favorable tetrahedral or trigonal bond angles with other nearby atoms, i.e., unfavorable interactions have $\theta_{ijk} \neq$ 109.5° and $\theta_{ijk} \neq$ 120°. The functional forms and parameters of ζ and g define these favorable bond angles, the details of which are described in [53]. Figure 1.10 shows a schematic of the interactions between a group of carbon atoms i, j, k, l, and m modeled with the Tersoff potential. Atoms i, k, l, and m represent atoms in a plane of graphite (see Figure 1.7 (b)) with trigonal sp^2 bonding. If a fifth atom, atom j, is placed near atom i as shown in Figure 1.10, the term b_{ij} between them would tend towards 0 due to the angle θ_{ijk} being far from 120° (and far from 109.5°). Note that b_{ij} is a sum over all nearby three-body interactions (see Equation 1.5), thus also accounts for the angle between atoms j, i,

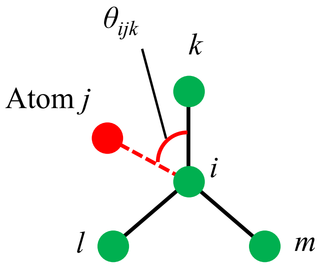

Figure 1.10 Schematic of the interactions between a group of carbon atoms *i*, *j*, *k*, *l*, and *m* modeled with the Tersoff potential.

and *l* (θ_{ijl} as labeled in Figure 1.10), etc. Given the unfavorable position of atom *j* with respect to atom *i* and its other neighboring atoms, b_{ij} and thus, the attractive term $b_{ij}f_A(r_{ij})$ in Equation 1.5 would be negligible and the interaction between atoms *i* and *j* would be repulsive, pushing atom *j* away from atom *i* and towards a more favorable position.

Like the Tersoff potential, the AIREBO potential was developed primarily to model carbon in a wide range of bonding configurations. Depending on the composition of the system of interest, it is more versatile and in some cases more accurate than the Tersoff potential, particularly when modeling C-H bonding, but is not commonly used for modeling Si-Si and Si-C interactions and requires more computation than the Tersoff potential. The AIREBO takes the following form:

$$U_{AIREBO} = U_{REBO} + U_{LJ} + U_{TORSION}, \tag{1.6}$$

where U_{REBO} is a Tersoff-style pair function (Equation 1.5), U_{LJ} is a Lennard-Jones pair function (Equation 1.1), and $U_{TORSION}$ is a four-body torsional term that controls the rotation of atomic pairs about their bond axis. The Tersoff-style U_{REBO} differs from the Tersoff potential in that the b_{ij} term of the Tersoff potential is replaced with $\overline{b}_{ij}$ in U_{REBO}, where $\overline{b}_{ij}$ is the average of the b_{ij} terms for atom *i* and atom *j*, i.e. $\overline{b}_{ij} = (b_{ij}+b_{ji})/2$. This accounts for the bonding environments of both atom *i* and atom *j*, whereas the Tersoff potential accounts only for the environment of atom i when calculating its contribution to the potential energy of the system. Thus, the AIREBO potential more accurately models the radical orbitals that form when a 3-coordinated carbon atom bonds to a four-coordinated carbon atom, and more accurately models the difference between conjugated and nonconjugated double C-C bonds compared to the Tersoff potential [54]. Furthermore, the functional forms and parameters of ζ (see Equation 1.5) differ in U_{REBO} compared to $U_{TERSOFF}$, with more information about an atom's local bonding environment calculated with U_{REBO}. Because U_{REBO} and $U_{TERSOFF}$ emphasize local bonding in network solids such as diamond, graphite, and DLC, the cutoff function f_C and the screening functions inherent in ζ truncate atomic interactions in most atomic structures much closer to each atom than is typical for nonscreened and long-range potentials, such as the Lennard-Jones or Morse potentials. Thus, U_{REBO} and $U_{TERSOFF}$ do not accurately model long-range interactions, which are important for some atomic structures such as near the surface of bulk carbon. The AIREBO potential corrects for this by superimposing a longer-range Lennard-Jones potential U_{LJ} on top of the U_{REBO} pairwise bonding term. However, this U_{LJ} term contains additional switching parameters that exclude atom pairs that are close together and have large interaction energy due to the U_{REBO} term. Thus, it describes the long-range but not the short-range portion of the Lennard-Jones potential. The torsional term $U_{TORSION}$ is important primarily for hydrocarbon chains with C-C bonds that are constrained against torsional rotations by hybridized atomic orbitals, but is not important when modeling dense solids such as diamond, graphite, or DLC.

The Tersoff and AIREBO potentials were designed primarily to model the many possible configurations of C-C, C-Si, Si-Ge, and C-H bonds, which are comprised of primarily covalent bonds. Hence, they are not as commonly used for modeling materials in which the pairwise interactions are primarily not covalent, such as metals. The embedded atom method (EAM) potential is an interatomic potential developed primarily for modeling metals [56]. Baskes enhanced the EAM potential by adding angular dependence so that it can be used to model an expanded range of materials, including systems with both metallic and covalent materials. The resulting potential is thus known as the modified EAM or MEAM potential [55] and takes the following form:

$$U_{MEAM} = F_i\left(\overline{\rho_i}\right) + \frac{1}{2}\sum_{j \neq i} \phi_{ij}\left(r_{ij}\right), \tag{1.7}$$

where $\overline{\rho_i}$ is the background electron density at the location of atom i due to its neighbors, F_i is an embedding function that describes how much energy is required to embed atom i at a location with the background electron density $\overline{\rho_i}$, and ϕ_{ij} is the pair energy between atoms i and j separated by a distance r_{ij}, similar to the attractive exponential term in the Morse or Tersoff potential. The functional form and parameters of F_i give the MEAM potential its angular dependence, and are described in [55]. $\overline{\rho_i}$ accounts for every atom j that interacts with atom i, hence, the total pairwise potential energy for the MEAM potential is a single summation over every atom i in the system, unlike the double summation over atoms i and j as shown in Equation 1.3. The MEAM potential has been parameterized for a wide range of elements and atomic structures, including face-centered cubic (FCC) solids, body-centered cubic solids, diamond cubic solids, and diatomic gases [55]. It has been parameterized to model carbon and silicon, but is not as accurate at describing covalent bonding as the Tersoff or AIREBO potentials, particularly when the atoms are far from their equilibrium lattice positions, such as in amorphous solids like DLC or a-Si [57]. The limitation in the number and type of materials that can be accurately modeled by the Tersoff, AIREBO, and MEAM potentials is in fact inherent to all interatomic potentials, and is due to the intrinsic link between the functional form of the potential and the description of atomic behavior, and thus, a material's bulk properties. Thus, it is often impossible to use a single interatomic potential to accurately model a multicomponent system with MD. Figure 1.11 shows two techniques to model the interface between materials that are each modeled most accurately using different interatomic potentials, such as the Tersoff and MEAM potentials for Si and Ni, respectively. Figure 1.11 (a) shows the simplest technique to model an interface between two different materials, which consists of modeling each material with the most accurate interatomic potential available for that material in the configuration of interest and calculating cross-species interactions with a simple two-body potential such as the Lennard-Jones or Morse potential (see, e.g., [58,59]). The primary benefit of this technique is that it can be used with any combination of materials and interatomic potentials that comprise the multicomponent system. However, although it provides

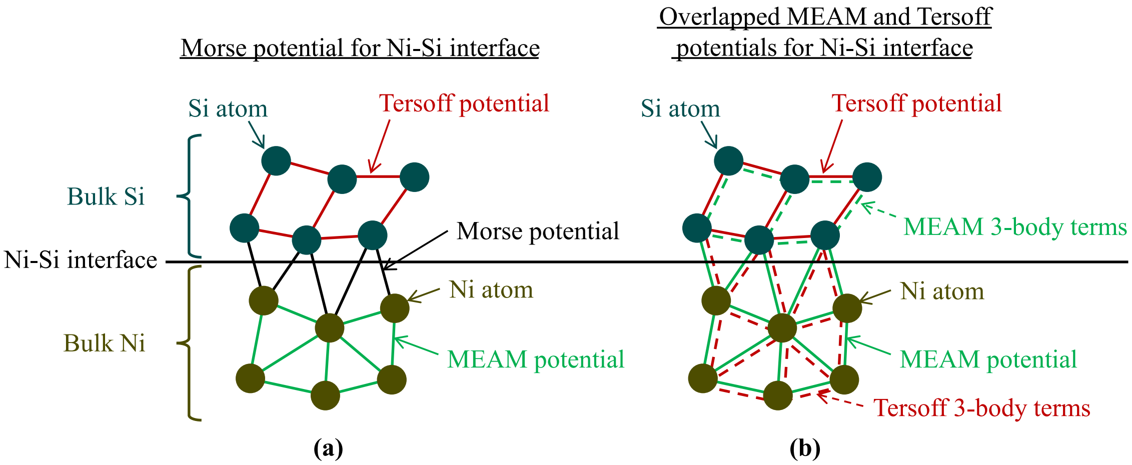

Figure 1.11 Two techniques to model the interface between materials that are each modeled most accurately using different interatomic potentials, such as the Tersoff and MEAM potentials for Si and Ni, respectively.

sufficient accuracy for modeling some phenomena, use of the two-body potential suffers from the same limitations discussed above for systems in which angular forces and the effect of local bonding environment play an important role in calculating atomic interactions. Figure 1.11 (b) shows another approach for modeling an interface between materials that is possible only for some systems for which the different many-body interatomic potentials are parameterized to model each material in the system. Similar to the first approach (Figure 1.11 (a)), each material is modeled with the most accurate potential available for that material, but is also included in the many-body calculations of the other interatomic potentials used in the model. As shown in Figure 1.11 (b) when modeling the interface between bulk silicon and bulk nickel using the Tersoff and MEAM potentials, respectively, both materials are described using both potentials, provided that the parameters of each potential are modified such that the pair interaction between each pair of atoms atom is only calculated once. Thus, to ensure that the Tersoff potential is used to model bulk Si and the MEAM potential is used to model bulk Ni and the Ni-Si interactions, one must modify the parameters of f_A and f_R (Equation 1.4) so that they contribute to the system's energy for Si-Si but not Ni-Ni and Ni-Si interactions, and the parameters of F_i and ϕ_{ij} (Equation 1.7) so that they contribute to Ni-Ni and Ni-Si interactions but not Si-Si interactions. This calculates pairwise energies only once per pair of atoms, while correctly modeling second-neighbor interactions and angular terms via the b_{ij} and $\overline{\rho}_i$ terms. This approach has been used to overlap the AIREBO and Tersoff potentials and the Tersoff and MEAM potentials for modeling material interfaces in this study. The specific potential parameters used are included in the Appendix.

1.4.4 The time evolution of a system of atoms

Determining the time evolution of an atomic system requires more than defining a material's behavior via an interatomic potential, because an interatomic potential describes the interaction of atoms in space but not in time. Time is modeled in MD by determining the forces on each atom at a given time and integrating Newton's equations of motion to update each atom's position accordingly. In theory, given an initial position and velocity for each atom in the system and an equation(s) for the interactions between them, one can find an exact solution that describes the trajectory of each atom through all time, although in practice this is not possible due to the complexity of the coupled interactions between the atoms [60]. Thus, MD uses a finite difference numerical integration technique in which time is discretized into a series of time steps, and the trajectory of each atom is calculated along these discrete time steps. This integration algorithm typically assumes constant energy between each time step, and thus, in many cases the most useful ensemble for defining thermodynamic properties of the system in MD is the microcanonical or $NV\mathscr{E}$ ensemble, although modified algorithms exist that allow one to define the system in terms of a different ensemble. Hence, many numerical integration algorithms are possible (see, e.g., [51,60]). A commonly-used $NV\mathscr{E}$ integration algorithm in MD is the velocity Verlet algorithm, and is popular because it exhibits energy conservation, time reversibility, and is computationally efficient, all of which are critical for MD integration algorithms [51,60]. The velocity Verlet algorithm is a modification of the Verlet algorithm, which is a fourth-order integration algorithm based on a Taylor series expansion of an atom's position, $\mathbf{r}_i(t)$:

$$\mathbf{r}_i\left(t+\Delta t\right)=\mathbf{r}_i\left(t\right)+\left(\Delta t\right)\mathbf{v}_i\left(t\right)+\frac{1}{2}\left(\Delta t\right)^2\mathbf{a}_i\left(t\right)+\cdots, \tag{1.8}$$

where t is the current time step, Δt is the difference between time steps, $t + \Delta t$ is the next time step to be calculated, and $\mathbf{r}_i$, $\mathbf{v}_i$, and $\mathbf{a}_i$ are an atom's position, velocity, and acceleration, respectively. By combining the equations of the Taylor expansion for $t + \Delta t$ and t - Δt, one can cancel the third-order terms and obtain a simple, fourth-order accurate expression for an atom's predicted position as a function of its position and acceleration only:

$$\mathbf{r}_i\left(t+\Delta t\right)=2\mathbf{r}_i\left(t\right)-\mathbf{r}_i\left(t-\Delta t\right)+\left(\Delta t\right)^2\mathbf{a}_i\left(t\right). \tag{1.9}$$

However, the terms with $\mathbf{v}_i(t)$ also disappear, thus, one limitation of the Verlet algorithm is the need for extra calculations if one wants to determine an atom's velocity, which is necessary for determining the atom's kinetic energy and thus, the temperature of the system. A further drawback to the Verlet algorithm as formulated in Equation 1.9 is the loss of precision that can occur when adding a term with $(\Delta t)^2$ to the difference between two much larger terms, particularly for small time steps [60]. These difficulties have been overcome by Swope et al. [61], who presented a modified Verlet algorithm, known as the velocity Verlet algorithm. In their formulation, one first calculates an atom's position at t + Δt using:

$$\mathbf{r}_i\left(t+\Delta t\right)=\mathbf{r}_i\left(t\right)+\left(\Delta t\right)\mathbf{v}_i\left(t\right)+\frac{1}{2}\left(\Delta t\right)^2\mathbf{a}_i\left(t\right), \tag{1.10}$$

assuming $\mathbf{r}_i(t)$, $\mathbf{v}_\mathrm{i}(t)$, and $\mathbf{a}_i(t)$ are known at the current time step t. Then, the velocity at the intermediate step $t + (1/2)\Delta t$ is calculated using:

$$\mathbf{v}_i\left(t+\frac{1}{2}\Delta t\right)=\mathbf{v}_i\left(t\right)+\frac{1}{2}\left(\Delta t\right)\mathbf{a}_i\left(t\right). \tag{1.11}$$

Finally, the atom's velocity at $t + \Delta t$ is calculated using

$$\mathbf{v}_i\left(t+\Delta t\right)=\mathbf{v}_i\left(t+\frac{1}{2}\Delta t\right)+\frac{1}{2}\left(\Delta t\right)\mathbf{a}_i\left(t+\Delta t\right). \tag{1.12}$$

This requires a knowledge of the atom's acceleration at the next time step, $\boldsymbol{a}_i(t + \Delta t)$, which is calculated using the atom's position at the next time step $t + \Delta t$ (Equation 1.10) and Newton's second law:

$$\mathbf{a}_i\left(t\right)=\frac{\sum_j \mathbf{F}_{ij}}{m_i}, \tag{1.13}$$

where m_i is the mass of the atom and $\Sigma_j(\mathbf{F}_{ij})$ is the sum of the forces $\mathbf{F}_{ij}$ on the atom due to each of the surrounding atoms j. The force of an atom j on atom i is determined using:

$$\mathbf{F}_{ij,d}=-\frac{\partial U_{ij}}{\partial r_{ij}}\frac{\partial r_{ij}}{\partial d}\hat{\boldsymbol{d}}, \tag{1.14}$$

where U_{ij} is the potential energy function that describes the interaction between atom i and atom j, such as U_{LJ}, $U_{Tersoff}$, etc, and d is the Cartesian direction x, y, or z. Equations 1.10-1.14 provide $\mathbf{r}(t + \Delta t)$, $\mathbf{v}(t + \Delta t)$, and $\mathbf{a}(t + \Delta t)$ for an atom at the next desired time step $t + \Delta t$, and are solved simultaneously for every atom in the system, thus providing all the data necessary for calculating the state of the system at the time step $t + \Delta t$. The time step $t + \Delta t$ is then taken to be the current time step, and the process is successively repeated until the atomic trajectories have been calculated over the desired number of time steps, which thus describe the evolution of the system in time. Because of the approximate nature of the numerical integration technique and the finite precision inherent when using a computer to iteratively use the velocity Verlet algorithm, errors propagate through the system and thus, the numerical solution increasingly deviates from the exact solution with increasing number of time steps. A large time step would thus be desirable to simulate long time scales with the fewest number of time steps possible, and thus, minimize round-off error. However, the truncation error due to truncation of the Taylor expansion (Equation 1.8) increases with increasing time step. Thus, an optimal time step should balance the need to minimize these types of error, and thus, maximize accuracy, which must in turn be balanced with the desire to minimize the total calculation time. The optimal time step is usually taken to be approximately an order of magnitude smaller than the vibrational period of the highest-frequency atomic vibration in the system [60]. In practice, the round-off error is often small over the time scales simulated in actual MD simulations, and although it causes a system to deviate from its exact trajectory, these deviations have a statistically negligible effect on the thermodynamic properties of the system, particularly when the system is controlled through appropriate thermodynamic boundary conditions.

Although the velocity Verlet algorithm updates positions and velocities of each atom from one time step to the next, it does not provide a description of their initial positions or velocities. The initial positions of each atom depend upon the material being modeled, e.g., they are placed at FCC lattice sites when modeling FCC metals. In many cases, preliminary work is required to determine the initial positions of each atom in a complex system. The initial velocities of each atom are typically unknown, and thus are randomly assigned from a Gaussian or uniform distribution. The actual distribution used for the initial velocity assignments is not important because the distribution of the atoms' velocities rapidly approaches the Maxwell-Boltzmann distribution expected at the system's specified temperature, independent of the initial velocity distribution [60]. Uncertainty in the initial configuration of the system and the time required for the system to reach equilibrium necessitate the use of an initial equilibration period during which the positions, velocities, and other system properties are tightly controlled until the expected behavior of the system in equilibrium is observed, after which point the system will remain stable indefinitely or until numerical error or externally-applied changes cause the system to become unstable.

1.4.5 Computational considerations

When coupled with the processing power of a modern supercomputer, MD becomes a powerful tool that can simulate systems with millions of atoms for millions of time steps or more. Although these corresponding time and length scales are fast compared to many observable phenomena and small compared to macroscopic systems, they allow MD to simulate important but complex atomic-scale phenomena or to be used as a bridge that can help atomistically explain the behavior of macroscopic systems. One of the primary advantages in using a supercomputer is its ability to spatially partition the system of interest across many processors and thus, simulate a much larger simulation than would be possible with a single processor in a given amount of time. However, an inherent drawback to the numerical integration algorithm is that each time step is calculated for the entire system at once and depends successively upon all previous time steps. Thus, the use of multiple processors cannot be used to partition the simulation in time as it can partition it in space, and thus does not directly facilitate longer simulation times compared to a single processor. Furthermore, even for a modern supercomputer, it is not feasible to repeatedly calculate the NxN interactions between pairs of atoms in an N-body system when N is greater than a few hundred or thousand atoms. Hence, some computational simplifications must be implemented to reduce the total number of calculations required. This often involves calculating interactions between an atom and only those within a limited distance, such as by using a cutoff for interatomic potentials (Equation 1.4), and by simulating only a fraction of the actual physical system of interest. These solutions require the use of neighbor lists that keep track of which atoms are near each other and well-defined boundary conditions for the simulation that represent bulk material around a limited simulation volume. Often, a simulation volume is a fixed volume in space or a periodic repetition of that volume that simulates a larger volume of material than would otherwise be feasible. The need to accurately model boundary conditions, track neighbor lists, calculate interactions between only the atoms specified by those neighbor lists, implement the integration algorithm, partition the simulation volume across many processors on a supercomputer, and ensure accurate communication across processors, requires software that is complex to write, debug, verify, and use. Furthermore, the efficiency of the algorithms becomes increasingly important with increasing numbers of atoms within an MD model. Thus, it is often impractical to write new MD code for each different MD model, and many researchers take advantage of available open-access MD codes that are designed such that one can specify the desired materials and/or phenomena to be modeled while implementing previously optimized and efficient MD algorithms. We use the LAMMPS code [62], which is open source and maintained by Sandia National Labs. LAMMPS provides efficient implementation of many common MD algorithms and interatomic potentials, but requires additional tools for pre- and postprocessing the MD simulations to create initial configurations of complex systems, visualize the trajectories of atoms calculated by the software, and compute desired system properties from the atomic trajectories.

1.4.6 Calculating physical properties from MD trajectories

MD data consist of snapshots of the system at a series of discrete time steps. The three categories of data most useful to this study consist of global thermodynamic data, per-atom values, and pairwise values. Global thermodynamic data such as temperature, pressure, and total energy are useful for quantifying the state of the entire system and verifying its stability, i.e., verifying that the time step is small enough to prevent energy drift when no energy is being explicitly added to or removed from the simulation volume. Per-atom values such as position, potential energy, volume, and coordination number, and pairwise values such as bond length, bond energy, and bond type between atom pairs can be compared at different time steps of a MD simulation to determine which atoms have been displaced, how much their energy has changed, how much a distance between two atoms has changed (bond length), and how the direction of the axis between two atoms has changed (bond rotation) due to a specified external load. Thus, deformation within a material can be quantified by comparing per-atom and pairwise values at a desired time step to those values at a desired reference time step. For example, Figure 1.12 shows the position of an atom $\mathbf{r}_i$ as a function of time t at discrete time steps Δt. The displacement of atom i, $\Delta\mathbf{r}_i$, can be determined by comparing its position at two distinct time steps as indicated. However, the systems modeled using MD, including those discussed in this study, are much smaller than the ensemble sizes used to relate a system's thermodynamic properties to the motion of its constituent particles, and thus, there is non-negligible statistical fluctuation in the thermodynamic properties of a simulated system as a function of time. Furthermore, thermal vibrations occur for each atom when a system is at a nonzero temperature. These fluctuations affect the accuracy of

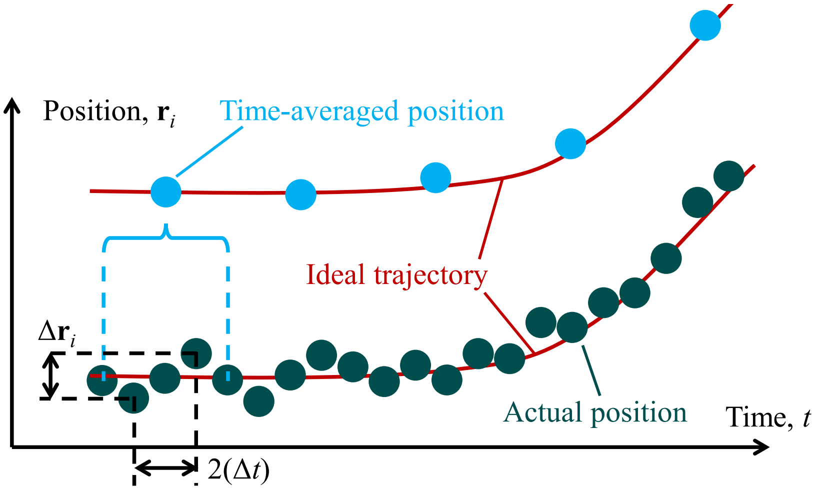

Figure 1.12 The position of an atom $\mathbf{r}_i$ as a function of time t at discrete time steps Δt.

the calculations for the properties of interest, and thus, the displacement $\Delta\mathbf{r}_i$ shown in Figure 1.12 is much larger than it would be in the absence of these fluctuations, represented by the atom's ideal trajectory. This uncertainty can be reduced by time averaging the properties of interest, which can reduce the uncertainty in the corresponding calculation, as represented by the time-averaged atomic positions in Figure 1.12. This is possible because the phenomena of interest in a MD simulation typically occur over much longer time scales than the atomic vibrations that limit the maximum allowable time step. Indeed, it is often unnecessary to record data at every time step in a simulation, and only a subset of the time steps in a simulation need be recorded. Furthermore, for many properties of interest, spatial averaging can be used in addition to time averaging to reduce the uncertainty due to statistical uncertainty. For these properties, the per-atom or pairwise value is averaged over all nearby atoms or atom pairs, respectively, and thus, provides a local average of the desired property throughout the system. Thus, the number of time steps for which data must be computed and recorded depends on the time scale of the phenomena of interest and of the amount of statistical variation in the properties being measured and thus, on the degree of time averaging and spatial averaging to be performed.

1.5 Structure of the dissertation

The remainder of the dissertation builds on the concepts introduced in this chapter to achieve the research objective and is organized as follows. In Chapter 2, we simulate nanoindentation of an ultra-thin multilayer DLC coating to determine how the mechanical properties of the coating and its ability to prevent plastic deformation of the coating and substrate change as a function of coating design parameters. In Chapter 3, we simulate combined normal and tangential loading of an ultra-thin multilayer DLC coating, representing contact between a recording head and magnetic disk in an HDD, to determine the effect of coating design parameters on the coating's ability to prevent plastic deformation and delamination during a realistic contact event between two surfaces. In Chapter 4, we simulate simple shear, tension, and nanoscratch tests of an ultra-thin multilayer DLC coating to determine the effect of coating design parameters on the adhesion of the coating to the substrate and on the coating's ability to resist plastic deformation due to combined normal and tangential loading that leads to future delamination. Finally, in Chapter 5 we summarize the conclusions of this work.

1.6 References

[1] Charitidis C. a., 2010, "Nanomechanical and Nanotribological Properties of Carbon-Based Thin Films: A Review," Int. J. Refract. Met. Hard Mater., **28**(1), pp. 51–70.

[2] Carey M. J., Maat S., Chandrashekariaih S., Katine J. A., Chen W., York B., and

Childress J. R., 2011, “Co_2MnGe-Based Current-Perpendicular-To-The-Plane Giant-Magnetoresistance Spin-Valve Sensors For Recording Head Applications,” J. Appl. Phys., **109**(9), p. 93912.

[3] Hauert R., 2004, “An Overview on the Tribological Behavior of Diamond-Like Carbon In Technical and Medical Applications,” Tribol. Int., **37**(11-12), pp. 991–1003.

[4] Grill A., 1999, “Diamond-Like Carbon : State of the Art,” Diam. Relat. Mater., **8**(2-5), pp. 428–434.

[5] Dearnaley G., and Arps J. H., 2005, “Biomedical Applications of Diamond-Like Carbon (Dlc) Coatings: a Review,” Surf. Coatings Technol., **200**(7), pp. 2518–2524.

[6] Erdemir A., and Donnet C., 2006, “Tribology of Diamond-Like Carbon Films: Recent Progress and Future Prospects,” J. Phys. D. Appl. Phys., **39**(18), pp. R311–R327.

[7] Robertson J., 2002, “Diamond-Like Amorphous Carbon,” Mater. Sci. Eng. R Reports, **37**(4-6), pp. 129–281.

[8] Gioti M., Logothetidis S., and Charitidis C., 1998, “Stress Relaxation and Stability in Thick Amorphous Carbon Films Deposited in Layer Structure,” Appl. Phys. Lett., **73**(2), pp. 184–186.

[9] Fallon P. J., Veerasamy V. S., Davis C. A., Robertson J., Amaratunga G. A. J., Milne W. I., and Koskinen J., 1993, “Properties of Filtered-Ion-Beam-Deposited Diamondlike Carbon As a Function of Ion Energy,” Phys. Rev. B, **48**(7), pp. 4777–4782.

[10] Zhao F., Li H. X., Ji L., Mo Y. F., Quan W. L., Zhou H. D., and Chen J. M., 2009, “Structural, Mechanical and Tribological Characterizations of a-C:H:Si Films Prepared by a Hybrid Pecvd and Sputtering Technique,” J. Phys. D. Appl. Phys., **42**(16), p. 165407.

[11] Chhowalla M., Yin Y., Amaratunga G. A. J., McKenzie D. R., and Frauenheim T., 1996, “Highly Tetrahedral Amorphous Carbon Films With Low Stress,” Appl. Phys. Lett., **69**(16), p. 2344.

[12] Ferrari a. C., Kleinsorge B., Morrison N. a., Hart a., Stolojan V., and Robertson J., 1999, “Stress Reduction and Bond Stability During Thermal Annealing of Tetrahedral Amorphous Carbon,” J. Appl. Phys., **85**(10), p. 7191.

[13] Shum P. W., Zhou Z. F., and Li K. Y., 2003, “Optimisation of Carbon Implantation Pre-Treatments on the Adhesion Strength of Amorphous Carbon Coatings on AISI 440C Steel Substrates,” Surf. Coatings Technol., **166**(2–3), pp. 213–220.

[14] MoberlyChan W. J., Adams D. P., Aziz M. J., Hobler G., and Schenkel T., 2007, “Fundamentals of Focused Ion Beam Nanostructural Processing: Below, At, and Above the Surface,” MRS Bull., **32**(5), pp. 424–432.

[15] Wu W.-J., and Hon M.-H., 1999, “The Effect of Residual Stress on Adhesion of Silicon-Containing Diamond-Like Carbon Coatings,” Thin Solid Films, **345**(2), pp. 200–207.

[16] Srisang C., Asanithi P., Siangchaew K., Pokaipisit A., and Limsuwan P., 2012, “Characterization of SiC in DLC/a-Si Films Prepared by Pulsed Filtered Cathodic Arc Using Raman Spectroscopy and XPS,” Appl. Surf. Sci., **258**(15), pp. 5605–5609.

[17] Voevodin A. a., Walck S. D., and Zabinski J. S., 1997, “Architecture of Multilayer Nanocomposite Coatings with Super-Hard Diamond-Like Carbon Layers For Wear Protection At High Contact Loads,” Wear, **203**–**204**, pp. 516–527.

[18] Chen K. W., and Lin J. F., 2009, “The Study of Adhesion and Nanomechanical Properties of DLC Films Deposited on Tool Steels,” Thin Solid Films, **517**(17), pp. 4916–4920.

[19] Daniel E. D., Mee C. D., and Clark M. H., eds., 1999, *Magnetic Recording: the First 100 Years*, IEEE Press, New Jersey.

[20] Wood R., 2009, “Future Hard Disk Drive Systems,” J. Magn. Magn. Mater., **321**(6), pp. 555–561.

[21] Bhushan B., 1990, *Tribology and Mechanics of Magnetic Storage Devices*, Springer-Verlag, New York.

[22] Pugsley D. W., 1946, “Wire Recording,” Electr. Eng., **65**(7), pp. 316–321.

[23] Raeymaekers B., 2005, “Study of Lateral Tape Motion and Tape Transients,” PhD Thesis, University of California, San Diego.

[24] Ohkoshi S. ichi, Namai A., Yoshikiyo M., Imoto K., Tamazaki K., Matsuno K., Inoue O., Ide T., Masada K., Goto M., Goto T., Yoshida T., and Miyazaki T., 2016, “Multimetal-Substituted Epsilon-Iron Oxide β-$Ga_{0.31}Ti_{0.05}Co_{0.05}Fe_{1.59}O_3$ for Next-Generation Magnetic Recording Tape in the Big-Data Era,” Angew. Chemie - Int. Ed., **55**(38), pp. 11403–11406.

[25] Dee R. H., 2008, “Magnetic Tape For Data Storage: An Enduring Technology,” Proc. IEEE, **96**(11), pp. 1775–1785.

[26] Abramovitch D., and Franklin G., 2002, “A Brief History of Disk Drive Control,” Control Syst. IEEE, **22**(April), pp. 28–42.

[27] Yuan Z. M., Liu B., Zhou T., Goh C. K., Ong C. L., Cheong C. M., and Wang L.,

2009, “Perspectives of Magnetic Recording System At 10 Tb/in^2,” IEEE Trans. Magn., **45**(11), pp. 5038–5043.

[28] Wang Y., Wei X., Liang X., Yin S., Zi Y., and Tsui K., 2016, “An In Situ Measurement Method for Electric Potential at Head – Disk Interface Using a Thermal Asperity Sensor,” **52**(1), pp. 2–7.

[29] Matthes L. M., Knigge B. E., de Callafon R. A., and Talke F. E., 2016, “Near Contact Thermal Flying Height Control in Hard Disk Drives,” IEEE Trans. Control Syst. Technol., **25**(1), pp. 39–46.

[30] Donnet C., and Erdemir A., eds., 2008, *Tribology of Diamond-like Carbon Films: Fundamentals and Applications*, Springer Science and Business Media, US.

[31] Kimock F. M., Brown D. W., and Finke S. J., 1999, “The Evolution of Ion-Beam Diamond-like-Carbon Technology into Data Storage, Sunglasses, Sliders, and now Disks,” Datatech, **Volume**, pp. 69–77.

[32] Yasui N., Inaba H., Furusawa K., Saito M., and Ohtake N., 2009, “Characterization of Head Overcoat For 1 Tb/in^2 Magnetic Recording,” IEEE Trans. Magn., **45**(2), pp. 805–809.

[33] Lee S., and Yeo C. D., 2012, “Microwear Mechanism of Head Carbon Film During Head Disk Interface Sliding Contact,” Tribol. Int., **45**(1), pp. 30–37.

[34] Song D., Kvitek R., and Schnur D., 2006, “Inspection of Pole Tip Diamondlike Carbon Wear Due to Heater-Induced Head-Disc Contact,” J. Appl. Phys., **99**(8), pp. 2004–2007.

[35] Vetter J., 2014, “60 Years of DLC Coatings: Historical Highlights and Technical Review of Cathodic Arc Processes to Synthesize Various DLC Types, and Their Evolution For Industrial Applications,” Surf. Coatings Technol., **257**, pp. 213–240.

[36] Li Q., Ma Y., Oganov A. R., Wang H., Wang H., Xu Y., Cui T., Mao H. K., and Zou G., 2009, “Superhard Monoclinic Polymorph of Carbon,” Phys. Rev. Lett., **102**, p. 175506:1-4.

[37] Patterson J. R., Catledge S. A., Vohra Y. K., Akella J. J., and Weir S. T., 2000, “Electrical and Mechanical Properties of C70 Fullerene and Graphite under High Pressures Studied Using Designer Diamond Anvils,” Phys. Rev. Lett., **85**, pp. 5364–5367.

[38] Schwarz U. D., Zworner O., Koster P., and Wiesendanger R., 1997, “Quantitative Analysis of the Frictional Properties of Solid Materials At Low Loads: I. Carbon Compounds,” Phys.Rev.B., **56**(11), pp. 6987–6996.

[39] Mate C. M., McClelland G. M., Erlandsson R., and Chiang S., 1987, “Atomic-Scale Friction of a Tungsten Tip on a Graphite Surface,” Phys. Rev. Lett., **59**(17),

pp. 1942–1945.

[40] Grillo S. E., and Field J. E., 2000, “The Friction of CVD Diamond At High Hertzian Stresses: the Effect of Load, Environment and Sliding Velocity,” J. Phys. D. Appl. Phys., **33**(6), pp. 595–602.

[41] Bruno P., Cicala G., Losacco A. M., and Decuzzi P., 2004, “Mechanical Properties of PECVD Hydrogenated Amorphous Carbon Coatings Via Nanoindentation and Nanoscratching Techniques,” Surf. Coatings Technol., **180–181**, pp. 259–264.

[42] Boyd K. J., Marton D., Todorov S. S., Al-Bayati A. H., Kulik J., Zuhr R. A., and Rabalais J. W., 1995, “Formation of C–N Thin Films by Ion Beam Deposition,” J. Vac. Sci. Technol. A Vacuum, Surfaces, Film., **13**(1995), pp. 2110–2122.

[43] Park Y. S., and Hong B., 2008, “Characteristics of Sputtered Amorphous Carbon Films Prepared by a Closed-Field Unbalanced Magnetron Sputtering Method,” J. Non. Cryst. Solids, **354**(52–54), pp. 5504–5508.

[44] Martin P. J., and Bendavid A., 2001, “Review of the Filtered Vacuum Arc Process and Materials Deposition,” Thin Solid Films, **394**(1–2), pp. 1–15.

[45] Patsalas P., Kaziannis S., Kosmidis C., Papadimitriou D., Abadias G., and Evangelakis G. A., 2007, “Optimized Pulsed Laser Deposition by Wavelength and Static Electric Field Control: the Case of Tetrahedral Amorphous Carbon Films,” J. Appl. Phys., **101**, p. 124903:1-7.

[46] Casiraghi C., Robertson J., and Ferrari A. C., 2007, “Diamond-Like Carbon For Data and Beer Storage,” Mater. Today, **10**(1–2), pp. 44–53.

[47] Podgornik B., Hren D., and Vižintin J., 2005, “Low-Friction Behaviour of Boundary-Lubricated Diamond-Like Carbon Coatings Containing Tungsten,” Thin Solid Films, **476**(1), pp. 92–100.

[48] Deng H., Scharf T. W., and Barnard J. a., 1997, “Adhesion Assessment of Silicon Carbide, Carbon, and Carbon Nitride Ultrathin Overcoats by Nanoscratch Techniques,” J. Appl. Phys., **81**(8), p. 5396.

[49] Lee K. M., Yeo C. D., and Polycarpou a. a., 2007, “Nanomechanical Property and Nanowear Measurements For Sub-10-Nm Thick Films in Magnetic Storage,” Exp. Mech., **47**(1), pp. 107–121.

[50] McQuarrie D. A., 2000, *Statistical Mechanics*, University Science Books, California.

[51] Frenkel D., and Smit B., 2002, *Understanding Molecular Simulation*, Academic Press, California.

[52] Gao G. T., Mikulski P. T., and Harrison J. a, 2002, “Molecular-Scale Trobology of

Amorphous Carbon Coatings: Effects of Film Thickness, Adhesion, and Long-Range Interactions," J. Am. Chem. Soc., **124**(21), pp. 7202–7209.

[53] Tersoff J., 1989, "Modeling Solid-State Chemistry: Interatomic Potentials For Multicomponent Systems," Phys. Rev. B, **39**(8), pp. 5566–5568.

[54] Stuart S., Tutein A., and Harrison J., 2000, "A Reactive Potential For Hydrocarbons with Intermolecular Interactions," J. Chem. Phys., **112**(14), pp. 6472–6486.

[55] Baskes M. I., 1992, "Modified Embedded-Atom Potentials For Cubic Materials and Impurities," Phys. Rev. B, **46**(5), pp. 2727–2742.

[56] Daw M. S., and Baskes M. I., 1983, "Semiempirical, Quantum Mechanical Calculation of Hydrogen Embrittlement in Metals," Phys. Rev. Lett., **50**(17), pp. 1285–1288.

[57] Cook S. J., and Clancy P., 1993, "Comparison of Semi-Empirical Potential Functions For Silicon and Germanium," Phys. Rev. B, **47**(13), pp. 7686–7699.

[58] Peng P., Liao G., Shi T., Tang Z., and Gao Y., 2010, "Molecular Dynamic Simulations of Nanoindentation in Aluminum Thin Film on Silicon Substrate," Appl. Surf. Sci., **256**(21), pp. 6284–6290.

[59] Sung P. H., Wu C. D., and Fang T. H., 2012, "Investigation of Nanomechanical Properties of Al/Ni and Ni/Al Nanomultilayers Under Nanobending Using Molecular Dynamics Simulation," Comput. Mater. Sci., **56**(1), pp. 43–48.

[60] Leach A. R., 2001, *Molecular Modelling: Principles and Applications*, Pearson Education, London.

[61] Swope W. C., Andersen H. C., Berens P. H., and Wilson K. R., 1982, "A Computer Simulation Method For the Calculation of Equilibrium Constants For the Formation of Physical Clusters of Molecules: Application to Small Water Clusters," J. Chem. Phys., **76**(1), pp. 637–649.

[62] Plimpton S., 1995, "Fast Parallel Algorithms for Short-Range Molecular Dynamics," J. Comput. Phys., **117**(1), pp. 1–19.

CHAPTER 2

NANOINDENTATION OF ULTRA-THIN MULTILAYER DLC COATINGS USING MOLECULAR DYNAMICS SIMULATION

Modified with permission from [Price, M.R., Ovcharenko, A., Raeymaekers, B.: Qualitative evaluation of ultra-thin multilayer diamond-like carbon coatings using molecular dynamics nanoindentation simulations. Tribol. Lett. **62**, 1–10 (2016)].

2.1 Background

The mechanical properties of a DLC coating are often used to predict how the coating will resist plastic deformation such as wear, fracture, and delamination [1,2]. However, in a multilayer DLC coating, the mechanical properties depend on the mechanical properties of each different coating layer [3,4]. Furthermore, the amount of plastic deformation caused by an external load, the location of that plastic deformation within the coating or substrate, and the resulting mechanisms of coating failure depend on the thickness and composition of the coating layers [4,5]. Hence, to prevent wear and delamination of protective multilayer DLC coatings such as those used on HDD recording heads, it is important to understand how their mechanical properties change as a function of coating design parameters, including thickness and sp^3 fraction of the DLC layer and the thickness of the Si layer, and to understand how the coating's design parameters affect its ability to prevent plastic deformation of the coating and substrate due to external loading.

Mechanical properties of thin coatings are often determined using nanoindentation experiments. Indenting a surface with a hard tip while monitoring the force as a function of indentation depth enables calculating the hardness and Young's modulus of the material [6]. Several researchers have used nanoindentation to study the mechanical properties of DLC coatings. Sui and Cai [7] found that lowering the sp^3/sp^2 ratio of the DLC coating reduces hardness, whereas Beake and Lau [8] documented that increasing the thickness of a DLC coating increases hardness, similar to the findings of Ma et al. [9]. However, the thickness of the DLC coatings evaluated in these studies is on the order of 80 nm, which significantly exceeds the thickness of DLC coatings currently used in HDDs. Other researchers have focused specifically on evaluating the mechanical properties of DLC coatings used in HDDs. For instance, Lee et al. [2] measured the hardness and Young's modulus of sub-10 nm DLC coatings on magnetic disks and found that the mechanical properties measured near the surface are significantly affected by the coating layers below the DLC layer. Li and Bhushan [10] also found that the mechanical properties of magnetic disks depend on indentation depth due to the layered structure of the DLC and magnetic coatings. Hence, to reliably measure nanoscale mechanical properties of thin coatings, the indentation depth should not exceed 10-20% of the coating thickness [11]. However, as the thickness of DLC coatings in state-of-the-art HDDs approaches one to several nanometers, it becomes increasingly difficult to experimentally measure their mechanical properties. Thus, simulation tools such as molecular dynamics (MD) have gained popularity for evaluating the mechanical and tribological properties of ultra-thin coatings [12,13], even though the small size and time scales of MD simulations in addition to simplified material models often limit MD results to describing qualitative behaviors and trends rather than reproducing exact experimental results [12].

Several publications document using MD to simulate nanoindentation of crystalline [14,15] and noncrystalline [16–19] materials, although quantifying deformation remains difficult in amorphous materials due to the lack of an atomistic model for plastic flow [12]. Slufarzka et al. [16,17] modeled nanoindentation of amorphous SiC and found that nanoindentation damage is less localized in amorphous SiC than in cubic SiC and that inception of plastic deformation during nanoindentation occurs closer to the surface in the former than in the latter. Sinnot [18] simulated nanoindentation of DLC and found that the Young's modulus is in good agreement with experimental measurements. Wang and Komvopoulos [19] also modeled nanoindentation of DLC, and found that for indentations of less than 1 nm, the critical coating thickness for avoiding substrate effects is 3.5 nm. However, no studies exist that systematically evaluate and describe the effect of different coating parameters on the nanoscale mechanical properties of an ultra-thin multilayer DLC coating such as that used in a magnetic recording head in an HDD. Hence, the objective of this chapter is to determine the effect of coating design parameters, including thickness and composition, on the mechanical properties of the ultra-thin multilayer DLC coating of a magnetic recording head using nanoindentation simulations. This knowledge enables optimizing the coating parameters in terms of, e.g., maximum hardness or stiffness for a given thickness budget of the entire multilayer coating, and it allows deriving coating design guidelines for minimizing plastic deformation of the coating or substrate due to accidental contact with the disk. Although the emphasis of this paper is on magnetic recording heads used in HDDs, the results are relevant for any system in which the qualitative effect of coating parameters on the mechanical properties of a multilayer coating must be understood.

2.2 Methods

2.2.1 Model

Figure 2.1 shows the molecular dynamics model of a small section of the top pole of the recording head, as indicated by the red box in Figure 1.6. The MD model of the recording head consists of a bulk Ni substrate of thickness t_{sub} = 70 Å, covered with a DLC layer of thickness 12 Å $\leq t_1 \leq$ 18 Å. An a-Si layer of thickness 3 Å $\leq t_2 \leq$ 9 Å

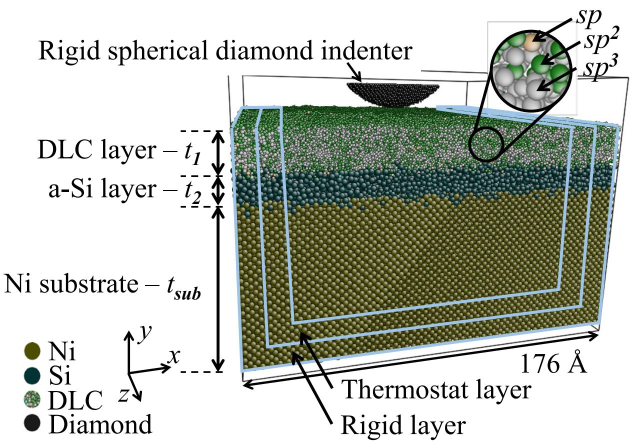

Figure 2.1 Molecular dynamics model of a small portion of the recording head, indicated by the red rectangular box in Figure 1.6.

improves adhesion between the DLC layer and Ni substrate. We have used Ni as the shield substrate material of the recording head instead of NiFe to simplify the computational model. Although the magnetic properties of NiFe and Ni are different, the mechanical properties such as hardness, Young's modulus, and Poisson ratio, which are of primary interest in this chapter, are similar [20–23]. The a-Si and DLC layers together comprise the protective coating, maintained at a combined thickness of $t_1 + t_2 = 21$ Å throughout this study. The fraction of sp^3-hybridized carbon atoms in the DLC layer on a recording head is approximately 70% (tetrahedral amorphous carbon, ta-C) [23]. However, to investigate the effect of the sp^3 fraction of the DLC layer on the mechanical properties of the protective coating, we perform the simulations for a DLC layer with 30% (amorphous carbon, a-C), 50%, and 70% (ta-C) sp^3 fraction. We model the indenter as a rigid spherical diamond tip with a radius of $r_{tip} = 35$ Å, which is 20% of the length of the 176 Å x 120 Å x 176 Å simulation box, chosen after a convergence study of the effect of box size and tip radius on the resulting mechanical properties. The model contains between 250,000 and 350,000 atoms, depending on t_1, t_2, and sp^3 fraction of the DLC layer. We hold the outer three atomic layers of the Ni substrate rigid and we maintain the three atomic layers immediately inward from the rigid layers at 300 K using a Langevin thermostat to simulate the presence of bulk material around the simulation box (see Figure 2.1). The remaining atoms are free to move according to classical mechanics and the microcanonical ensemble.

We create the MD model using a multistep annealing procedure, similar to the single-step annealing procedure used in other MD simulations of DLC [19,24]. We first create separate layers of DLC (30 Å) and a-Si (20 Å) by heating carbon and silicon atoms to 6000 K and 4000 K, respectively, and increasing the pressure to obtain the desired sp^3 fraction. We subsequently quench the amorphous phase to 300 K. We then place the a-Si layer between the DLC layer and the (100) plane of the Ni substrate and use a similar annealing procedure at the DLC-Si and Si-Ni interfaces. We remove the middle segments of the DLC and a-Si layers to decrease the thickness of each respective layer to the desired value of t_1 and t_2, and to ensure that all simulations will initiate from the same surface topography of the DLC coating. Finally, we bring the surfaces exposed by the removal of the middle of the DLC and a-Si layers into contact, and perform a final annealing procedure on the atomic layers nearest the exposed atoms. Using this multi-step annealing procedure, the atomic structure of the DLC surface and the interfaces between the layers are the same for different coatings and thus, the simulation results are only dependent on t_1 and t_2 and not the local atomic structure of the interfaces between the different material layers and the DLC surface topography.

We use the following interatomic potentials: MEAM [25,26] for Ni-Ni and Ni-Si interactions, Tersoff [27] for Si-Si, Si-C and C-C interactions, and 12-6 Lennard-Jones potential truncated at the zero-energy distance for the interactions between the indenter tip and the recording head so that we only consider repulsive interactions, simulating an indentation that neglects adhesion [28]. We use $\sigma = 1.5$ Å for the LJ parameter that represents the length of a bond between sp^2- and sp^3-hybridized carbon atoms [29]. Because the LJ potential is truncated at 1.5 Å, the results from the nanoindentation simulations are not sensitive to the LJ energy parameter ε, which we have set $\varepsilon = 1$ eV. We use the Sandia LAMMPS code to perform the nanoindentation simulations [30]. We maintain a time step of 0.25 fs throughout this work and perform equilibration at 300 K for 10 ps prior to all simulations.

2.2.2 Simulation procedure

Figure 2.2 (a) shows the indentation depth h versus time t of the nanoindentation procedure described by Oliver and Pharr [6], applied to a picosecond time scale. The purpose of the multiple load-unload cycle is to ensure that the unloading data used in the analysis is mostly elastic. However, due to the high computational cost of MD simulations, we use a modified nanoindentation procedure based on a single load and unload cycle as shown in Figure 2.2 (b), and similar to what others have used [28,31]. We have determined a difference of less than 6% between the hardness and Young's modulus obtained with both nanoindentation procedures, indicating that using a single-cycle procedure minimally affects the nanoindentation results for the coatings we have evaluated.

We perform indentation simulations of $3 \text{ Å} \leq h \leq 13 \text{ Å}$ deep, which does not exceed 13% of the thickness of the multilayer coating and non-rigid substrate atoms, to avoid that the rigid substrate atoms influence the results [11]. However, because the

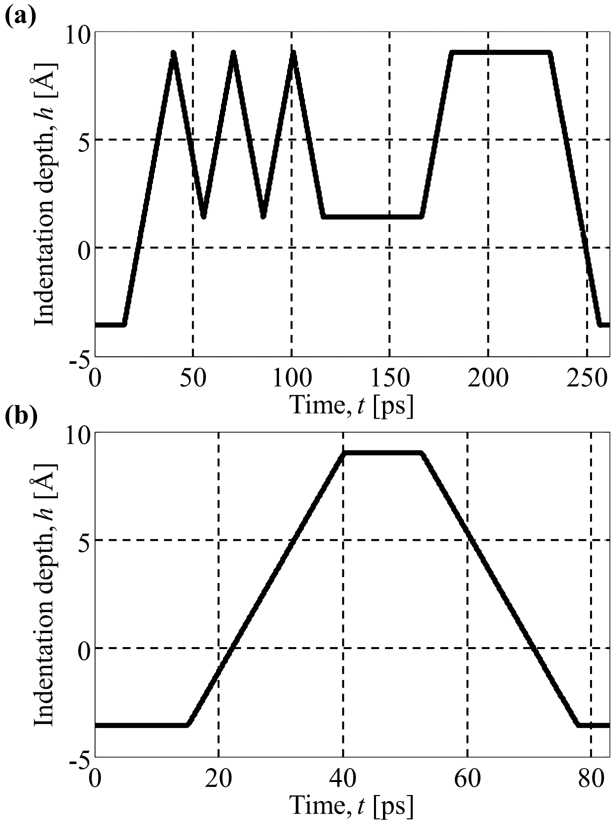

Figure 2.2 Nanoindentation procedures. These include the indentation depth as a function of time for (a) the Oliver and Pharr method applied to a picosecond time scale and (b) the modified method used in this study.

indentation depth significantly exceeds 10% of the thickness of the DLC layer, the results represent the mechanical properties of the entire multilayer coating and substrate, instead of the DLC layer by itself. The indenter moves with velocity $v_y = 50$ m/s as it follows the prescribed loading curve (Figure 2.2(b)), which is higher than in physical nanoindentation experiments, but is typical of nanoindentation simulations as discussed by, e.g., Noreyan et al. [31] and Nair et al. [32], who showed that the indentation velocity has a negligible effect on the results of MD nanoindentation simulations within the range of velocities used in their studies (2.5 m/s to 85.7 m/s).

2.2.3 Data analysis

Figure 2.3 (a) shows a typical force P versus indentation depth h nanoindentation result for a coating with t_1 = 15 Å (70% sp^3 fraction) and t_2 = 6 Å. First, we fit $P = C(h-h_f)^{m_f}$ to the unload portion of the curve where C, h_f, and m_f are curve-fit parameters determined using the least-squares method (curve-fit shown as black solid curve). Then, we calculate the hardness $H = P_{max}/A$ and Young's modulus $E = S/2\cdot(\pi/A)^{1/2}$, where A is the projected contact area between the indenter and the coating and $S = dP/dh$ is the unloading stiffness at the inception of unloading (h_{max}, P_{max}). The dashed black line is the tangent line to the unloading curve at (h_{max}, P_{max}), which we use together with an indenter tip geometry shape factor [6] to determine the contact depth h_c and the projected contact

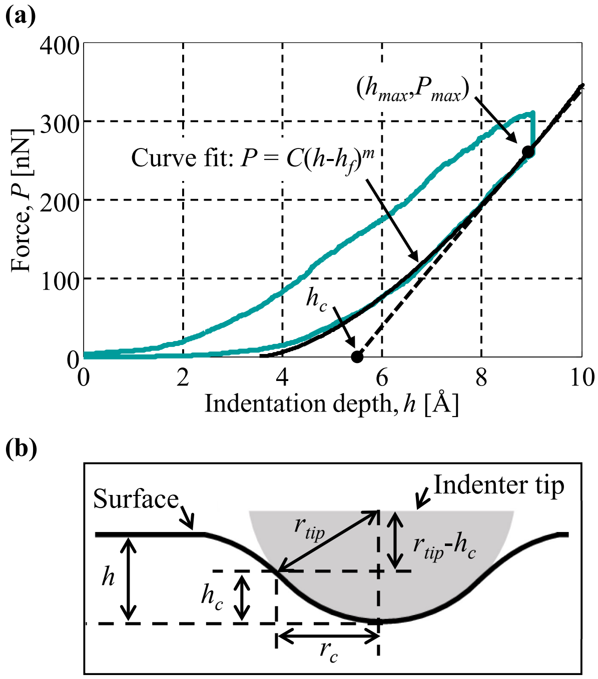

Figure 2.3 Important nanoindentation parameters. (a) Typical nanoindentation force versus indentation depth curve for a coating with t_1 = 15 Å (70% sp^3 fraction) and t_2 = 6 Å. The solid black line shows the curve fit to the unloading portion of the curve. The dashed black line is the tangent line to the unloading curve at (h_{max}, P_{max}) used to determine the contact depth h_c. (b) Schematic showing contact depth, h_c, indentation depth h, and contact radius r_c.

area A. Figure 2.3 (b) schematically illustrates the difference between the contact depth h_c and the indentation depth h, and defines the relationship between contact radius r_c and contact depth h_c as $r_c = [(r_{tip}^2-(r_{tip}-h_c)^2]^{1/2}$. Contact occurs when a coating atom experiences a nonzero force due to the presence of the indenter. We use the tangent line to the unloading curve to determine h_c (see Figure 2.3) and calculate the projected contact area $A = \pi r_c^2$. This method yields similar results than determining A directly from atomic coordinates but allows a continuous rather than discrete possible outcome for the measurement of A, and avoids fitting a minimum bounding circle to the contacting atoms, which may be inaccurate.

2.2.4 Deformation characterization

We quantify deformation of the multilayer coating and substrate by measuring the displacement of individual atoms d_i, relative to their initial positions, throughout the nanoindentation simulation. Figure 2.4 shows the atomic displacement in a plane of atoms along the centerline of the indenter, for a coating with $t_C = 15$ Å (70% sp^3 fraction)

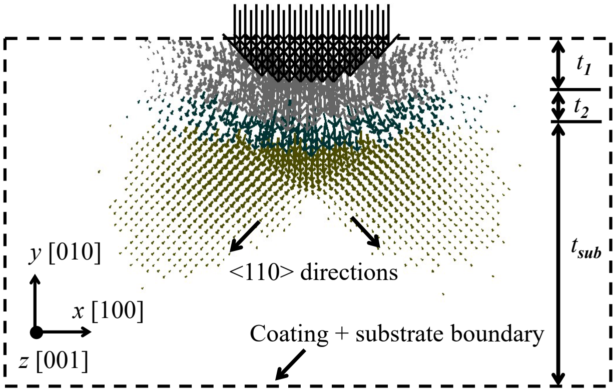

Figure 2.4 Displacement d_i of atoms during indentation. Shown as an arrow with length and thickness corresponding to the magnitude of d_i, and shown at maximum indentation depth of 9 Å for a coating with $t_1 = 15$ Å (70% sp^3 fraction) and $t_2 = 6$ Å.

and t_2 = 6 Å, at an indentation depth of 9 Å. The displacement d_i of each atom is represented by an arrow, whose direction and length represent the direction and magnitude of the displacement, respectively. We observe that the displacement of the atoms in the DLC and a-Si layers is radially symmetric about the center axis of the indenter tip, whereas the displacement of the Ni atoms is preferential to the <110> directions because of its FCC lattice. Some of the deformation caused by indentation is elastic and recovered upon unloading, the remainder is plastic. We quantify the plastic zone size as the fraction of atoms in each material layer of the coating and substrate (f_C, f_{Si}, and f_{Ni}) that undergo permanent displacement due to indentation. By comparing the coordinates of each atom at the initial time step of the simulation with those at a later time step but before indentation, we determine the probability density function (PDF) of the atomic displacement of each atom type due only to thermal motion. By comparing the PDFs before and after indentation, we determine the fraction of atoms that have moved further than what is expected due to thermal motion. Hence, this method distinguishes between atomic displacement resulting from thermal motion and that caused by indentation, and it does not rely on a cutoff distance to determine plastic deformation as in, e.g., [16], which does not account for small permanent displacements of atoms. Furthermore, the area under the force versus indentation depth loading curve represents the indentation energy e_{ind}, whereas the area contained between the loading and unloading curves represents the portion of the indentation energy that causes plastic deformation e_{pl} (see Figure 2.3 (a)). Hence, e_{pl}/e_{ind} quantifies the amount of plastic relative to total deformation [33].

2.3 Results and discussion

We have performed nanoindentation simulations of bulk Ni, a-Si, and DLC with 30% (a-C) and 70% (ta-C) *sp*^{3} fraction, using the procedure described in section 2.2.2. Table 2.1 shows the simulated hardness and Young's modulus of the bulk materials, which although higher than experimental results for Ni, ta-C, and a-C, are in good agreement with other simulation results [17,21,34–36]. The results of MD simulations are limited by the accuracy of the interatomic potentials used to describe the materials, and by the time scale and spatial domains that can be resolved.

We have also performed nanoindentation simulations of three different multilayer coatings (70% *sp*^{3} fraction DLC layer and a-Si layer) on a Ni substrate using the procedure described in section 2.2.2. Figure 2.5 (a) shows a schematic of the three coatings with varying t_1 and t_2 but constant total coating thickness $t_1 + t_2 = 21$ Å. Figure 2.5 (b) shows the hardness H and Figure 2.5 (c) shows the Young's modulus E of the multilayer coatings as a function of indentation depth h. The hardness and Young's modulus of the multilayer coating approaches that of bulk Ni with increasing indentation depth because the properties of the Ni substrate increasingly dominate the measurement, in agreement with [3,5,10]. We also observe that hardness and Young's modulus increase with increasing t_1, in agreement with experimental results [7,8]. This is because the DLC

Table 2.1 Simulated hardness and Young's modulus of the individual materials that comprise the multilayer coating of the recording head in an HDD.

Material	Hardness [GPa]	Young's modulus [GPa]
Ni (100)	20	202
a-Si	9	157
ta-C (70% *sp*^{3} fraction)	195	1221
a-C (30% *sp*^{3} fraction)	120	788

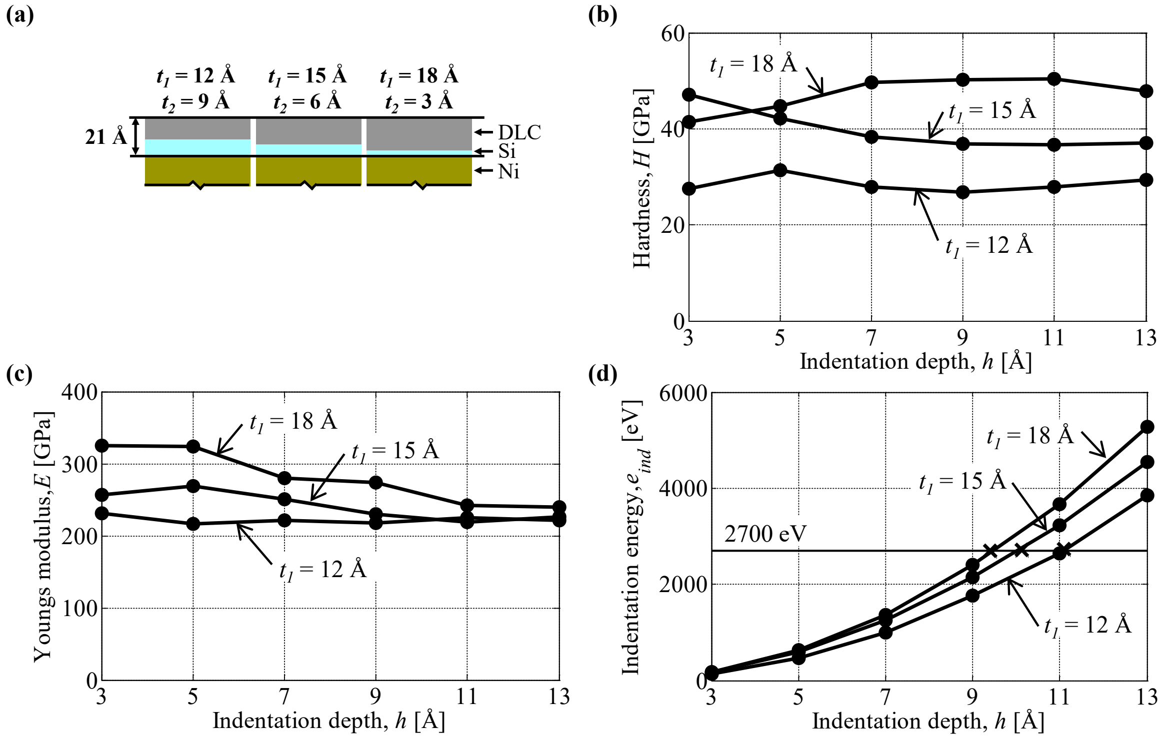

Figure 2.5 Hardness, Young's modulus, and indentation energy as a function of indentation depth. (a) Schematic of three coatings with varying t_1 and t_2 and with constant total coating thickness, and (b) hardness H, (c) Young's modulus E, and (d) indentation energy e_{ind} as a function of indentation depth for the coatings shown in (a) with 70% sp^3 fraction DLC.

layer has the highest hardness and Young's modulus of the three materials (see Table 2.1) and, therefore, its effect on hardness and Young's modulus of the multilayer coating increases with increasing thickness. Furthermore, the hardness and Young's modulus decrease with increasing t_2, because the a-Si layer has the lowest hardness and Young's modulus of the three materials (see Table 2.1) and the increasing a-Si layer thickness comprises an increasing fraction of the total thickness of the multilayer coating. The hardness depends on t_1 and t_2 for all indentation depths because hardness measurements for hard-on-soft coatings are affected by the substrate when the indentation depth is greater than 10% of the thickness of the coating, or when the hardness mismatch between coating and substrate causes yielding of the substrate before yielding of the coating [11].

This is in qualitative agreement with the experimental results of Lee et al. [2] for nanoindentation of DLC-coated magnetic disks.

To quantify the effect of the stochastic nature of MD simulations on the results, we have performed twelve separate indentations of the coating with t_1 = 15 Å, t_2 = 6 Å, h_{max} = 9 Å, and 70% sp^3 fraction DLC layer, which is an intermediate case of the parameter ranges shown in Figure 2.5. We have varied the initial distribution of atomic positions and velocities, and re-made the multilayer coating using the procedure described in section 2.2.1 to vary the surface topography of the amorphous DLC coating. We find that the coefficient of variation of the hardness and Young's modulus is 7.3% and 3.4%, respectively. In addition, we have performed a similar analysis of the same coating for the shallowest indentation depth h_{max} = 3 Å, and find a coefficient of variation of 15.5% and 1.7% for hardness and Young's modulus, respectively. The increased coefficient of variation for the shallowest indentation is because the indentation force decreases with decreasing indentation depth, thus reducing the signal-to-noise ratio. From this analysis, we conclude that the variation of the results due to the stochastic nature of MD is smaller than the differences in hardness and Young's modulus results for the different coatings shown in Figure 2.5 (b)-(c), except for the hardness determined for the shallowest indentation depths.

Figure 2.5 (d) shows the indentation energy e_{ind} as a function of the indentation depth h. We observe that the indentation energy increases with increasing indentation depth because more material must be displaced. Additionally, the indentation energy increases with increasing t_1 and decreasing t_2 for constant indentation depth because of the increasing hardness of the multilayer coating. Thus, we will evaluate plastic deformation of the coatings of Figure 2.5 (a) for (1) constant indentation depth, and (2) for constant indentation energy. We have chosen an indentation energy e_{ind} = 2700 eV, indicated by a horizontal line in Figure 2.5 (d), in the middle of the range we have investigated.

Figure 2.6 (a)-(c) show the fraction of permanently displaced C (f_C), Si (f_{Si}), and Ni (f_{Ni}) atoms after indentation of the three multilayer coatings shown in Figure 2.5 (a) as a function of indentation depth h. Analogous to the analysis of the data in Figure 2.5, we compute the coefficient of variation for f_C, f_{Si}, and f_{Ni} to be 4.6%, 2.6%, and 9.6%, respectively. We observe that f_C, f_{Si}, and f_{Ni} increase with increasing indentation depth, f_C

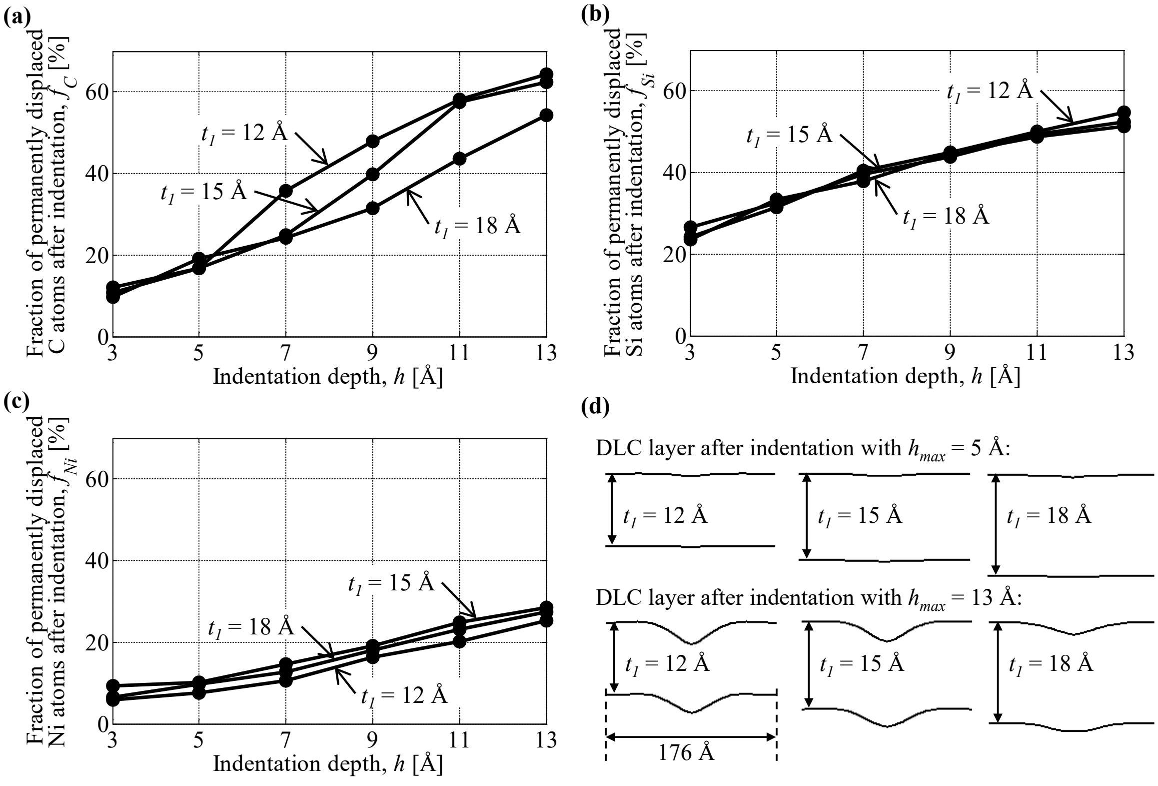

Figure 2.6 Fraction of permanently displaced atoms. Fraction of permanently displaced (a) C atoms f_C, (b) Si atoms f_{Si} , and (c) Ni atoms f_{Ni} after indentation as a function of indentation depth h for the three multilayer coatings of Figure 2.5 (a), and (d) contour of DLC layer after indentation with h_{max} = 5 Å and 13 Å.

increases with decreasing DLC layer thickness t_1, and f_{Si} and f_{Ni} are nearly independent of t_1. Because the hardness of the DLC layer decreases with decreasing t_1 (see Figure 2.5 (b)), it provides less resistance to plastic deformation [4]. This is in agreement with the experimental results of Yasui et al. [5] that show increasing hardness and decreasing plastic deformation of DLC-coated magnetic media with increasing DLC layer thickness. Figure 2.6 (d) shows the contour of the DLC layer of the three coatings after indentation with h_{max} = 5 Å and 13 Å, respectively, illustrating that the increase in plastic deformation of the DLC layer f_C with decreasing t_1 and increasing indentation depth results from the indenter beginning to penetrate through the DLC layer rather than bending or compressing it.

Figure 2.7 (a) shows the fraction of permanently displaced C (f_C), Si (f_{Si}), and Ni (f_{Ni}) atoms after indentation with a constant indentation energy e_{ind} = 2700 eV as a function of DLC layer thickness t_1. Figure 2.7 (b) shows the contour of the DLC layer after indentation with e_{ind} = 2700 eV, indicating the depth of the permanent indentation depression d_{pl}, and Figure 2.7 (c) shows the depth of the permanent indentation depression d_{pl} and the fraction of indentation energy causing plastic deformation e_{pl}/e_{ind} as a function of t_1 for constant indentation energy e_{ind} = 2700 eV.

From Figure 2.7 (a) we observe that the fraction of C (f_C) and Si (f_{Si}) atoms permanently displaced by the indentation decreases with increasing t_1. In addition, from Figure 2.7 (b) and (c) we observe that the fraction of the indentation energy causing plastic deformation decreases with increasing t_1, which results in decreasing depth of the permanent depression after indentation d_{pl}. Hence, for a constant total coating thickness budget, increasing the fraction of the coating comprised of DLC and decreasing the

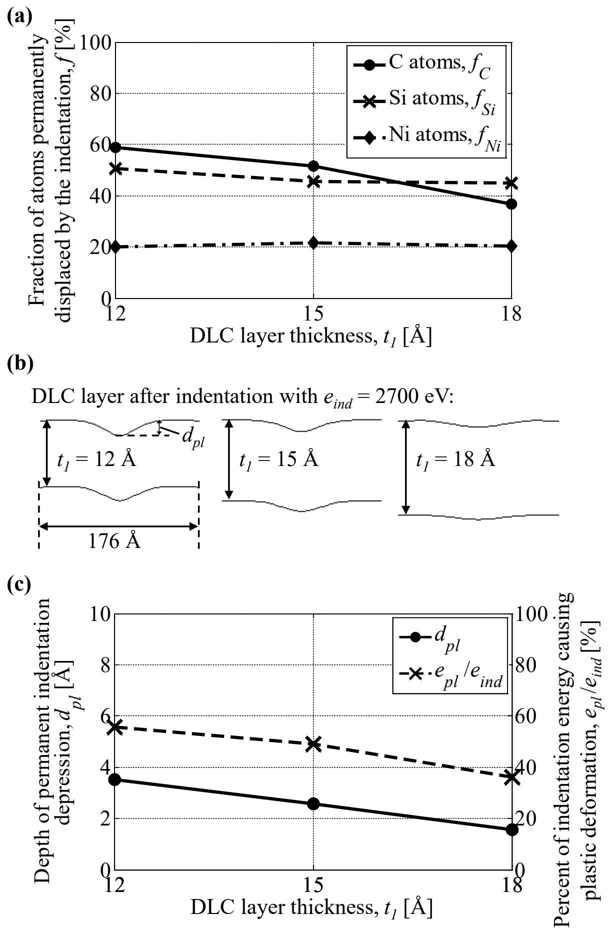

Figure 2.7 Effect of DLC layer thickness on a coating's resistance to plastic deformation. (a) Fraction of permanently displaced C (f_C), Si (f_{Si}), and Ni (f_{Ni}) atoms after indentation, (b) the contour of the DLC layer of each coating after indentation, and (c) the depth of the permanent indentation depression d_{pl} and the percent of indentation energy causing plastic deformation e_{pl}/e_{ind} as a function of the DLC layer thickness t_l for indentations with constant indentation energy e_{ind} = 2700 eV.

fraction comprised of a-Si will decrease plastic deformation in the coating resulting from an accidental contact between the recording head and magnetic disk, because the hardness of the coating increases. These results are in agreement with experimental results that document decreasing hardness with decreasing DLC layer thickness (e.g., [5]). We also observe that f_{Ni} is nearly independent of t_l because the coating thickness and indentation energy are constant and the indenter tip remains distant (> 8 Å, or 40% of the total coating thickness) from the Ni substrate for all indentations.

Figure 2.8 (a) and (b) show the hardness *H* and Young's modulus *E* of the multilayer coating, respectively, as a function of the sp^3 fraction of the DLC layer, for the three different multilayer coatings of Figure 2.5 (a), and for constant indentation energy e_{ind} = 2700 eV. From Figure 2.8, we observe that *H* and *E* first increase and then decrease with increasing sp^3 fraction of the DLC layer for the coatings investigated. This is different from the mechanical properties of DLC by itself, for which *H* and *E* increase monotonically with increasing sp^3 fraction (see Table 2.1 and [37]). We clarify this as follows. *H* and *E* of the multilayer coating increase with increasing *H* and *E* of a DLC layer of constant thickness t_1 and thus, with increasing sp^3 fraction of the DLC layer. However, with increasing mismatch between the mechanical properties of the DLC layer

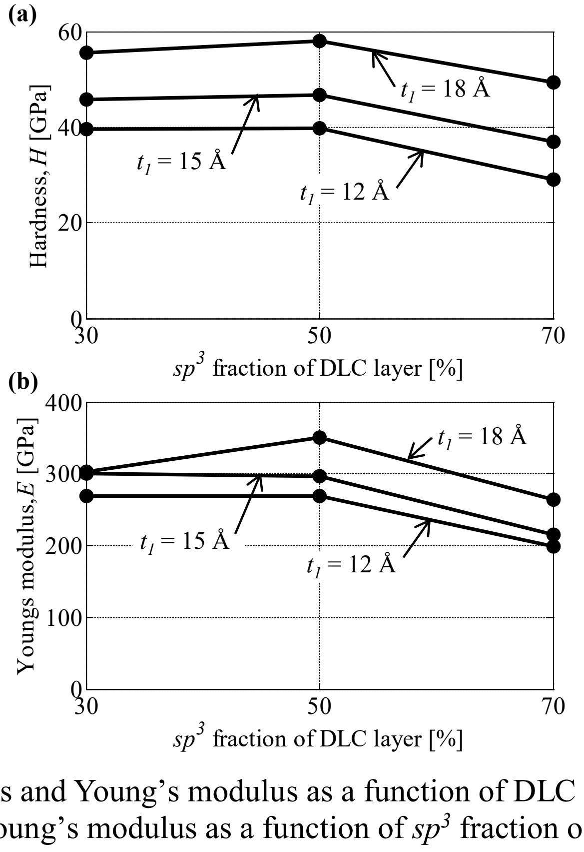

Figure 2.8 Hardness and Young's modulus as a function of DLC layer sp^3 fraction. (a) Hardness and (b) Young's modulus as a function of sp^3 fraction of the DLC layer and coating parameter t_1. Results are shown for constant indentation energy e_{ind} = 2700 eV and constant total coating thickness $t_1 + t_2$ = 21 Å.

and the material layers underneath, plastic deformation is increasingly preferential to the soft a-Si layer and Ni substrate, and the hard DLC layer bends into the fully plastic substrate [3] rather than being locally compressed under the indenter. This behavior has also been observed experimentally for nanoindentation [38] and scratch [39] tests, in which a diamond tip causes more local plastic deformation in *sp*^{2}-rich than in *sp*^{3}-rich DLC coatings of the same thickness, because plastic deformation of the substrate underneath the hard (*sp*^{3}-rich) coating causes the coating to bend into the substrate rather than being deformed by the indenter [39]. Figure 2.9 substantiates these observations.

Figure 2.9 (a)-(c) shows the local plastic strain in the multilayer coating with t_1 = 12 Å and t_2 = 9 Å after indentation with e_{ind} = 2700 eV, for a DLC coating with 30% *sp*^{3} fraction (Figure 2.9 (a)), 50% *sp*^{3} fraction (Figure 2.9 (b)), and 70% *sp*^{3} fraction (Figure 2.9 (c)). Figure 2.9 (d) shows the fraction of permanently displaced Ni atoms after indentation as a function of *sp*^{3} fraction of the DLC layer. From Figure 2.9 (a) we observe that the plastic strain in the coating with a DLC layer of 30% *sp*^{3} fraction occurs primarily in the DLC and a-Si layers, directly under the indenter tip. Plastic strain in the a-Si layer and Ni substrate increases with increasing *sp*^{3} fraction of the DLC layer (see Figure 2.9 (b) and (c)). Additionally, from Figure 2.9 (d) we observe that f_{Ni} increases due to the increasing plastic strain in the Ni substrate with increasing *sp*^{3} fraction of the DLC layer (Figure 2.9 (a)-(c)). Thus, Figure 2.9 further substantiates that plastic deformation is increasingly preferential to the substrate with increasing *sp*^{3} fraction of the DLC coating. This causes the hard coating to bend into the plastically deformed substrate rather than being compressed by the indenter and thus, results in reduced hardness and Young's modulus. These results are also in qualitative agreement with the results of Chen and

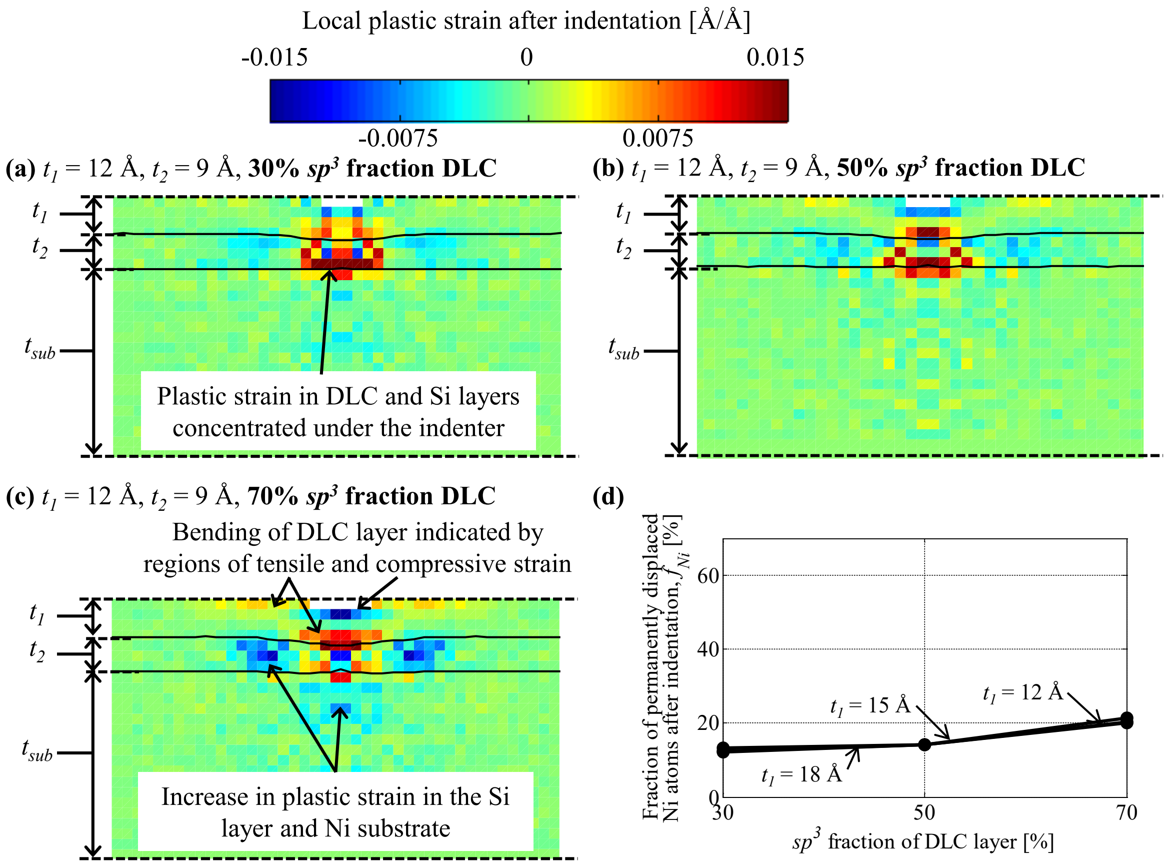

(a) $t_1 = 12$ Å, $t_2 = 9$ Å, **30%** sp^3 **fraction DLC**

(b) $t_1 = 12$ Å, $t_2 = 9$ Å, **50%** sp^3 **fraction DLC**

(c) $t_1 = 12$ Å, $t_2 = 9$ Å, **70%** sp^3 **fraction DLC**

(d)

Figure 2.9 Local plastic strain after indentation of the multilayer coating. Shown for $t_1 = 12$ Å and $t_2 = 9$ Å and (a) 30%, (b) 50%, and (c) 70% sp^3 fraction DLC, and (d) fraction of permanently displaced Ni atoms after indentation as a function of sp^3 fraction of the DLC layer. Constant indentation energy $e_{ind} = 2700$ eV is maintained.

Vlassak [4], which show increasing plastic deformation of the substrate with increasing coating hardness for a two-layer, hard-on-soft continuum model.

2.4 Conclusions

We have simulated nanoindentation of multilayer coatings consisting of a DLC layer on a Ni substrate, with a thin a-Si layer to improve adhesion between the DLC layer and Ni substrate. These multilayer coatings are used to protect the intricate magnetic structures of the recording head of a hard disk drive from accidental impact with the disk.

We conclude that the hardness and Young's modulus of the multilayer coating increase with increasing DLC layer and decreasing a-Si layer thickness, similar to experimental results obtained by others. DLC and a-Si are the hardest and softest materials of the multilayer coating, respectively, and increasing the thickness of each layer increases its fraction of the total thickness of the multilayer coating, which correspondingly affects its mechanical properties. Furthermore, the hardness and Young's modulus of the multilayer coating are a function of the sp^3 fraction and thus, the hardness of the DLC layer. However, maximizing the hardness of the multilayer coating is not sufficient to prevent deformation of the intricate recording structures embedded in the substrate of the recording head. Plastic deformation during indentation increasingly occurs in the a-Si layer and Ni substrate as opposed to in the DLC layer with increasing hardness of the DLC layer. As the plastically deformed a-Si and Ni layers are no longer able to support the external indentation load, the hard DLC layer bends like a plate, which reduces the hardness and Young's modulus of the multilayer coating.

Hence, to create a multilayer coating with maximum hardness and Young's modulus for a given thickness budget, we recommend increasing the thickness of the DLC layer, decreasing the thickness of the a-Si layer, and considering the hardness mismatch between the substrate and DLC layer to avoid that the coating bends into the plastically deformed substrate. Note that this analysis does not quantify the potential reduction or loss of adhesion between the DLC layer and Ni substrate with decreasing a-Si layer thickness. Hence, for HDD design the thickness of the DLC and a-Si layers should be increased and decreased, respectively, until the adhesive properties of the a-Si layer are compromised. To minimize plastic deformation of the magnetic substrate materials, plastic deformation of the coating should be increased, which can be achieved in part by decreasing the sp^3 fraction of the DLC layer. Decreasing the sp^3 fraction of the DLC layer may, however, decrease the hardness and Young's modulus of the multilayer coating and thus, a balance should be found between obtaining the desired hardness and Young's modulus to decrease wear of the coating, and minimizing the plastic deformation of the substrate.

2.5 References

1. Archard, J.F.: Contact and rubbing of flat surfaces. J. Appl. Phys. **24**, 981–988 (1953)

2. Lee, K.M., Yeo, C.D., Polycarpou, A.: Nanomechanical property and nanowear measurements for Sub-10-nm thick films in magnetic storage. Exp. Mech. **47**, 107–121 (2007)

3. Saha, R., Nix, W.D.: Effects of the substrate on the determination of thin film mechanical properties by nanoindentation. Acta Mater. **50**, 23–38 (2002)

4. Chen, X., Vlassak, J.J.: Numerical study on the measurement of thin film mechanical properties by means of nanoindentation. J. Mater. Res. **16**, 2974–2982 (2001)

5. Yasui, N., Inaba, H., Furusawa, K., Saito, M., Ohtake, N.: Characterization of head overcoat for 1 Tb/in^2 magnetic recording. IEEE Trans. Magn. **45**, 805–809 (2009)

6. Oliver, W.C., Pharr, G.M.: An improved technique for determining hardness and elastic modulus using load and displacement sensing indentation experiments. J. Mater. Res. **7**, 1564–1583 (1992)

7. Sui, J., Cai, W.: Mechanical properties and anti-corrosion behavior of the diamond-like carbon films. Surf. Coatings Technol. **201**, 1323–1327 (2006)

8. Beake, B.D., Lau, S.P.: Nanotribological and nanomechanical properties of 5–80 nm tetrahedral amorphous carbon films on silicon. Diam. Relat. Mater. **14**, 1535–1542 (2005)

9. Ma, X.G., Komvopoulos, K., Wan, D., Bogy, D.B., Kim, Y.S.: Effects of film thickness and contact load on nanotribological properties of sputtered amorphous carbon thin films. Wear. **254**, 1010–1018 (2003)

10. Li, X., Bhushan, B.: A review of nanoindentation continuous stiffness measurement technique and its applications. Mater. Charact. **48**, 11–36 (2002)

11. Hainsworth, S. V, Page, T.F.: Mechanical property data for coated systems - the prospects for measuring “coating only” properties using nanoindentation. Mater. Res. Soc. Symp. Proc. **436**, 171–176 (1997)

12. Szlufarska, I.: Atomistic simulations of nanoindentation. Mater. Today. **9**, 42–50 (2006)

13. Price, M.R., Ovcharenko, A., Thangaraj, R., Raeymaekers, B.: Deformation of ultra-thin diamond-like carbon coatings under combined loading on a magnetic recording head. Tribol. Lett. **57**, 3:1-9 (2015)

14. Szlufarska, I., Kalia, R.K., Nakano, A., Vashishta, P.: Nanoindentation-induced amorphization in silicon carbide. Appl. Phys. Lett. **85**, 378–380 (2004)

15. Szlufarska, I., Kalia, R.K., Nakano, A., Vashishta, P.: Atomistic mechanisms of amorphization during nanoindentation of SiC: A molecular dynamics study. Phys. Rev. B - Condens. Matter Mater. Phys. **71**, 1–11 (2005)

16. Szlufarska, I., Kalia, R.K., Nakano, A., Vashishta, P.: Atomistic processes during nanoindentation of amorphous silicon carbide. Appl. Phys. Lett. **86**, 1–4 (2005)

17. Szlufarska, I., Kalia, R.K., Nakano, A., Vashishta, P.: A molecular dynamics study of nanoindentation of amorphous silicon carbide. J. Appl. Phys. **102**, 023509:1-9 (2007)

18. Sinnott, S.B., Colton, R.J., White, C.T., Shenderova, O. a, Brenner, D.W., Harrison, J. a.: Atomistic simulations of the nanometer-scale indentation of amorphous-carbon thin films. J. Vac. Sci. Technol. A Vacuum, Surfaces, Film. **15**, 936 (1997)

19. Wang, N., Komvopoulos, K.: Nanomechanical and friction properties of ultrathin amorphous carbon films studied by molecular dynamcs analysis. ASME Conf. Proc. **2010**(44199), 393–395 (2010)

20. Deng, H., Minor, K.M., Barnard, J. a.: Comparison of mechanical and tribological properties of permalloy and high moment fetan thin films for tape recording heads. IEEE Trans. Magn. **32**, 3702–3704 (1996)

21. Ma, Z., Long, S., Pan, Y., Zhou, Y.: Creep Behavior and Its Influence on the Mechanics of Electrodeposited Nickel Films. J. Mater. Sci. Technol. **25**, 90–94 (2009)

22. Frick, C.P., Clark, B.G., Orso, S., Schneider, a. S., Arzt, E.: Size effect on strength and strain hardening of small-scale [1 1 1] nickel compression pillars. Mater. Sci. Eng. A. **489**, 319–329 (2008)

23. Klokholm, E., Aboaf, J. a.: The saturation magnetostriction of permalloy films. J. Appl. Phys. **52**, 2474–2476 (1981)

24. Gao, G.T., Mikulski, P.T., Harrison, J. a: Molecular-scale trobology of amorphous carbon coatings: effects of film thickness, adhesion, and long-range interactions. J. Am. Chem. Soc. **124**, 7202–7209 (2002)

25. Baskes, M.I.: Modified embedded-atom potentials for cubic materials and impurities. Phys. Rev. B. **46**, 2727–2742 (1992)

26. Baskes, M.I., Angelo, J.E., Bisson, C.L.: Atomistic calculations of composite interfaces. Model. Simul. Mater. Sci. Eng. **2**, 505–518 (1999)

27. Tersoff, J.: New empirical approach for the structure and energy of covalent systems. Phys. Rev. B. **37**, 6991–7000 (1988)

28. Walsh, P., Omeltchenko, A., Kalia, R.K., Nakano, A., Vashishta, P., Saini, S.: Nanoindentation of silicon nitride: A multimillion-atom molecular dynamics study. Appl. Phys. Lett. **82**, 118–120 (2003)

29. Lide, D.R.: A survey of carbon-carbon bond lengths. Tetrahedron. **17**, 125–134 (1962)

30. Plimpton, S.: Fast parallel algorithms for short-range molecular dynamics, J. Comp. Phys. **117**, 1-19 (1995)

31. Noreyan, a., Amar, J.G., Marinescu, I.: Molecular dynamics simulations of nanoindentation of β-SiC with diamond indenter. Mater. Sci. Eng. B Solid-State Mater. Adv. Technol. **117**, 235–240 (2005)

32. Nair, A.K., Parker, E., Gaudreau, P., Farkas, D., Kriz, R.D.: Size effects in indentation response of thin films at the nanoscale: A molecular dynamics study. Int. J. Plast. **24**, 2016–2031 (2008)

33. Kikuchi, N., Kitagawa, M., Sato, A., Kusano, E., Nanto, H., Kinbara, A.: Elastic and plastic energies in sputtered multilayered Ti–TiN films estimated by nanoindentation. Surf. Coatings Technol. **126**, 131–135 (2000)

34. Fang, T.H., Wu, J.H.: Molecular dynamics simulations on nanoindentation mechanisms of multilayered films. Comput. Mater. Sci. **43**, 785–790 (2008)

35. Follstaedt, D.M., Knapp, J. a., Myers, S.M.: Mechanical properties of ion-implanted amorphous silicon. J. Mater. Res. **19**, 338–346 (2004)

36. Grill, A.: Diamond-like carbon : state of the art. Diam. Relat. Mater. **8**, 428–434 (1999)

37. Casiraghi, C., Robertson, J., Ferrari, A.C.: Diamond-like carbon for data and beer

storage. Mater. Today. **10**, 44–53 (2007)

38. Charitidis, C. a.: Nanomechanical and nanotribological properties of carbon-based thin films: A review. Int. J. Refract. Met. Hard Mater. **28**, 51–70 (2010)

39. Charitidis, C., Logothetidis, S., Gioti, M.: A comparative study of the nanoscratching behavior of amorphous carbon films grown under various deposition conditions. Surf. Coatings Technol. **125**, 201–206 (2000)

CHAPTER 3

COMBINED NORMAL AND TANGENTIAL LOADING OF ULTRA-THIN MULTILAYER DLC COATINGS USING MOLECULAR DYNAMICS SIMULATION

Modified with permission from [Price, M.R., Ovcharenko, A., Thangaraj, R., Raeymaekers, B.: Deformation of ultra-thin diamond-like carbon coatings under combined loading on a magnetic recording head. Tribol. Lett. **57**, 3:1-9 (2015)]. © Springer 2015

3.1 Background

The nanoindentation simulation results discussed in Chapter 2 describe how the design parameters of an ultra-thin multilayer DLC coating affect the coating's mechanical properties and thus, can be used to predict the coating's resistance to plastic deformation due to external loading. However, the actual loading conditions experienced by protective DLC coatings, such as during the accidental contact between the recording head and magnetic disk of an HDD, often consist of components both normal and tangential to the surface of the coating. In these cases, the deformation of the coating is more complex than the deformation caused by only normal loading, i.e., more complex than the deformation caused by an indentation such as in Chapter 2. Hence, it is important to supplement the knowledge of a coating's mechanical properties with an understanding of how the coating will deform when subjected to combined normal and tangential loading.

Several published studies describe the deformation of ultra-thin multilayer DLC coatings caused by combined normal and tangential loading [1–4]. For instance, Prabhakaran and Talke [1] quantified the hardness and wear of DLC coatings on magnetic recording heads. They found good correlation between nanoindentation test, nanoscratch test, and contact-stop-start (CSS) wear test results but that scratch tests are better than nanoindentation tests for predicting wear resistance. Lee et al. [2] performed nanoindentation and nanoscratch tests on magnetic disks and also saw good agreement between nanoindentation hardness and wear resistance measurements, and that nanoscratch tests were affected less by the substrate than nanoindentation tests. Zhong et al. [3] performed wear tests on DLC coatings and determined a critical minimum coating thickness of 1.4 nm to ensure wear resistance under normal HDD operation for FCVA-deposited DLC coatings because a coating thinner than 1.4 nm did not significantly reduce the depth of the wear scars compared to those on an uncoated surface. However, Yasui et al. [4] also characterized sub-2 nm thick DLC coatings on the recording head and found that the coatings enhance wear resistance for coatings as thin as 1 nm. They also observed that the critical normal load for wear resistance during a nanoscratch test depends on the substrate material and the thickness of the DLC coating and that the results were similar for FCVA-deposited DLC coatings compared to coatings deposited using ion-assisted sputtering.

As the thickness of the ultra-thin protective DLC coatings is reduced further to accommodate decreasing the magnetic spacing between the recording head and the magnetic disk, experimental characterization becomes increasingly difficult. Consequently, MD has been used to study the mechanical properties of ultra-thin DLC coatings and their behavior under combined normal and tangential loading [5–8]. Ma et al. [5] used MD to investigate sliding of DLC coatings against a diamond counterface. They found that the low friction coefficient of the interface between DLC and diamond results from shear-induced graphitization of the DLC surface, migration of graphitized carbon layers across the sliding interface, and relative motion between the graphitized layers. Gao et al. [6] evaluated the tribological properties of DLC surfaces sliding against a diamond counterface as a function of the composition of the DLC layer and found that the tribological behavior is highly dependent on the sp^3/sp^2 ratio of the DLC layer. Wang and Komvopoulos [7] confirmed this observation. Additionally, Glosli et al. [8] emphasized, based on MD results, that for ultra-thin DLC coatings less than 5 nm thick, the mechanical properties are dominated by interfacial phenomena at the surface of the DLC coating. However, the primary focus of these MD studies is the interaction between the DLC layer and a rigid diamond counterface and not the adhesion between the DLC coating and the substrate.

Although minimizing wear and delamination of DLC coatings is of critical importance in many applications, no publications seem to exist that use MD to quantify the deformation and interfacial strength of the different layers of an ultra-thin multilayer DLC coating during combined normal and tangential loading. Several authors have used MD to study deformation of ultra-thin coatings and coating delamination from the substrate [9,10]. However, these studies do not model the materials, interfaces, or atomic structures of a multilayer DLC coating, such as those used in an HDD. Thus, the objective of this chapter is to evaluate the interfacial strength between the DLC coating, a-Si-layer, and Ni substrate as a function of thickness of the different coating layers and the contact pressure during combined normal and tangential loading of the recording head, and which represents accidental contact between the recording head and magnetic disk. We implement an MD model of a small three-dimensional portion of the HDI, simulating sliding contact between the DLC coating of the recording head and the disk, and we study the interfacial strength of the different coating layers under combined normal and tangential loading. Although we focus on the recording head in an HDD, this study also attempts to provide a general approach and framework for quantifying the strength of the interface between ultra-thin DLC coatings and a substrate.

3.2 Methods

3.2.1 *Model*

Figure 3.1 shows the MD model, which consists of a small three-dimensional section of a magnetic recording head, as indicated by the red rectangle in Figure 1.6, sliding against a hydrogen-terminated diamond counterface. The rigid hydrogen-terminated diamond counterface is used in place of a magnetic disk to reduce the computational cost of the MD simulations and because we focus on deformation of the recording head and not of the disk. However, the shear stress between the recording head and the hydrogenated diamond is similar to that between the head and disk surfaces in an HDD. The lubricant layer on the disk (see Figure 1.6) is not included in our model and thus, we simulate a worst-case scenario of head/disk contact with lubricant depletion. The recording head substrate consists of 47 Å of FCC Ni. Although Ni has different magnetic

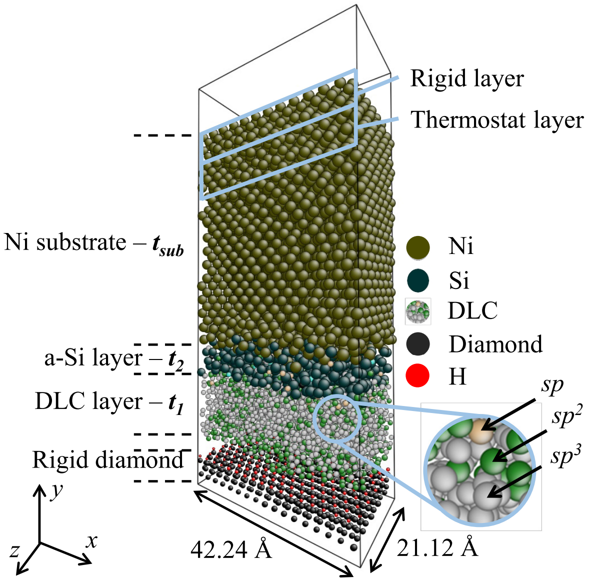

Figure 3.1 Molecular dynamics model of a small portion of the head-disk interface. This includes the different material layers of the recording head and the hydrogen-terminated diamond counterface, and their respective thickness. The magnified inset shows the different carbon hybridizations in the DLC layer.

properties than NiFe, its mechanical properties including hardness, Young's modulus, Poisson ratio, and lattice structure are similar [11–14]. Hence, the amount of deformation that occurs in the substrate due to external loading, and consequently in the DLC and a-Si layers, is not significantly affected by using Ni instead of NiFe. The Ni substrate is covered with an a-Si layer of thickness $3 \leq t_2 \leq 9$ Å and a ta-C layer of thickness $9 \leq t_1 \leq 18$ Å. The thickness of the a-Si and DLC layers are varied in this study by removing atoms from the middle of the respective layers, thereby ensuring that the DLC surface, and the DLC-Si and Ni-Si interfaces are consistent for coatings of different thickness. The sp^3-content of the DLC layer is 65% and is constant throughout this chapter. The DLC layer is formed using a heating and quenching procedure [6,7]. This process ensures a uniform sp^3 content throughout the DLC layer. The a-Si layer is created using a similar technique. The simulation box measures 42.24 x 100.00 x 21.12 Å in the x, y and z-directions, respectively, and the model contains between 6615 and 8434 atoms, depending on the thickness of the different coating layers. The boundary conditions of the MD model are periodic in the x and z-directions. The three outermost Ni atom layers in the y-direction are held rigid, and the three adjacent atom layers are maintained at 300 K using a Langevin thermostat to mimic the presence of surrounding bulk material. The hydrogen-terminated diamond counterface is held rigid throughout the simulation. The remaining atoms are free to move according to the microcanonical ensemble. The interatomic interactions are implemented with the following potentials: MEAM [10,15] for Ni-Ni and Ni-Si interactions, Tersoff [16] for Si-Si, Si-C, and C-C interactions, and AIREBO [17] for C-H and H-H interactions and overlap at the respective material interfaces as described in Section 1.4.3. We have used the Sandia LAMMPS code to perform the MD simulations [18]. A time step of 0.25 fs is used and equilibration at 300 K for 10 ps is performed for all simulations.

3.2.2 Simulation procedure

Figure 3.2 shows combined normal and tangential loading of the recording head on the disk, which simulates accidental contact. The diamond counterface moves relative to the recording head, at a constant speed of 75 m/s in the *x*-direction (step 1), which is similar to the highest relative velocity observed between recording head and disk in high-end server HDDs. The recording head is then loaded against the moving counterface until the desired contact pressure is reached (step 2), calculated as the ratio of the normal load between the recording head and the rigid counterface and the cross-sectional area of the simulation box (*x*-*z* plane). The moving counterface continuously slides against the head, resulting in combined normal and tangential loading (step 3). After sliding contact and combined loading, the head is separated from the moving counterface (step 4). The *x*-velocity of the disk is maintained constant until complete separation of head and counterface is obtained (step 5). We have performed simulations at a contact pressure p_c

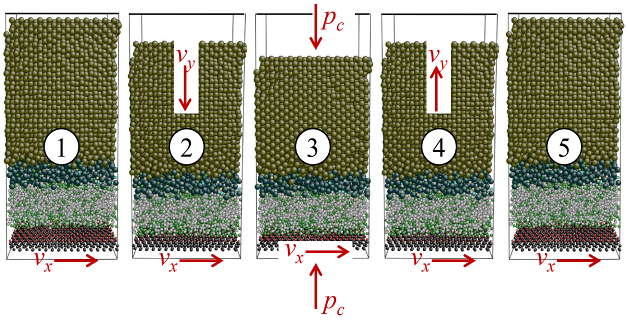

Figure 3.2 Schematic of combined normal and tangential loading procedure between the recording head and disk.

between the head and the counterface of 48 or 64 GPa. The values of p_c are realistic for typical head/disk impact and are calculated based on measured wear areas and contact loads [19,20]. They were also chosen to be similar in magnitude to the hardness of the coatings (see Figure 2.5) to give measurable deformation of the recording head in the short (130 ps) simulation time.

3.2.3 Deformation analysis

We quantify deformation of the different coating layers and their interfaces by evaluating the number and length of the interatomic bonds of each bond type, throughout the simulation, relative to their respective equilibrium bond length. A bond exists between two atoms when their separation is less than a cutoff distance that falls between their first and second nearest-neighbor distances [6]. The cutoff distance used for determining first-nearest neighbors and thus, bonded versus nonbonded interactions, is defined as the distance where the minimum between the first and second peaks of the radial distribution function (RDF) occurs for that bond type. Table 3.1 lists these cutoff values. The bond length is a function of the load, and changes in the bond length are used to quantify local strain in the coating. However, the bond cutoff is not affected by load,

Table 3.1 Bond length and cohesive energy of each of the bond types in the MD model. The bond length and bond cutoff distance is determined from the radial distribution functions (RDF). The equilibrium bond length is also given for each bond type.

Bond type	Equilibrium structure	Equilibrium structure bond length [Å]	RDF bond length [Å]	RDF bond cutoff [Å]	Cohesive energy [eV]
Ni-Ni	FCC	2.49 [10]	2.49	3.10	4.44 [22]
Ni-Si	l12	2.41 [10]	2.40	2.77	5.51 [23]
Si-Si	diamond	2.35 [16]	2.56	2.91	4.63 [24]
Si-C	3C-SiC	1.89 [16]	1.87	2.35	6.47 [25]
C-C	diamond	1.54 [28]	1.50	1.96	7.84 [26]

and remains unchanged throughout the simulation. The equilibrium bond length is determined as the location of the first peak in the radial distribution function when no load is present, i.e., when the system is in equilibrium. Figure 3.3 shows the equilibrium RDF, $g(r_{ij})$, of the C-C bond type as an example. The location of the first peaks in the equilibrium RDFs for all bond types in the simulation are within 1% of their respective equilibrium reference structures for all atomic interactions except Si-Si and C-C interactions. The location of the Si-Si peak results in an equilibrium bond length 8.7% larger than predicted by the reference structure, because the a-Si layer conforms to the Ni FCC lattice. The location of the C-C peak at 1.50 Å corresponds to the length of a bond between sp^3 and sp^2 hybridized C-C bonds [21], which is the prevailing structure in the amorphous mixture of sp^3- and sp^2-hybridized carbon atoms in the DLC layer.

We define deformation on the atomic scale as a change in the number of bonds, with a permanent change in the number of bonds indicating plastic deformation and a permanent decrease in the number of bonds between two coating layers indicating delamination or separation between those coating layers. Strain is calculated as the ratio

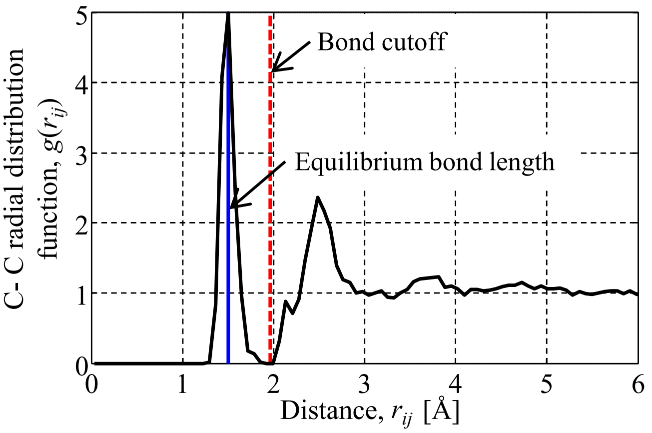

Figure 3.3 Radial distribution function for C-C interactions. Shown for a recording head coating with t_1 = 12 Å and t_2 = 3 Å. The values have been normalized with the value at r_{ij} = 6 Å.

of the change of the bond length between two atoms Δl and the equilibrium bond length between those atoms l_0. Local strain in the MD model is determined by overlaying a grid in the x-y plane on the recording head and calculating the average strain of all the bonds with x- and y-coordinates that fall into each grid element, i.e., $\Sigma(\Delta l/l_0)/N_{bonds}$ for each grid element, where the summation is over the total number of bonds N_{bonds} in the grid element. Residual strain is quantified by calculating the strain in the coating, before loading has occurred. It is a measure of the strain caused by the difference in bond length and local structure mismatch near the Ni-Si and Si-C interfaces. Changes in the total bond energy throughout the recording head are also used to quantify deformation. Bond energy is calculated as the summation of the product of the number of bonds of a particular type N_T multiplied with the cohesive energy of that type E_T (see Table 3.1), i.e., $\Sigma(N_T E_T)$.

3.3 Results and discussion

3.3.1 Residual strain

Figure 3.4 shows the mean residual strain in the recording head, prior to loading, as a function of t_2, for different values of t_1. The mean residual strain decreases with increasing t_2 but is almost independent of t_1. The mean equilibrium bond length of Si-Si bonds, which is 8.7% larger than the theoretical value (see Table 3.1), and the local strain visualizations (see Figure 3.4), indicate that most of the strain is localized at the Ni-Si and Si-C interfaces. The a-Si layer conforms to the amorphous structure of the DLC layer on one side and to the FCC lattice of Ni on the other side. As the thickness of the a-Si layer decreases, the transition from Ni to DLC occurs over a smaller distance, increasing the local strain in the a-Si layer and surrounding interfaces due to the mismatch between

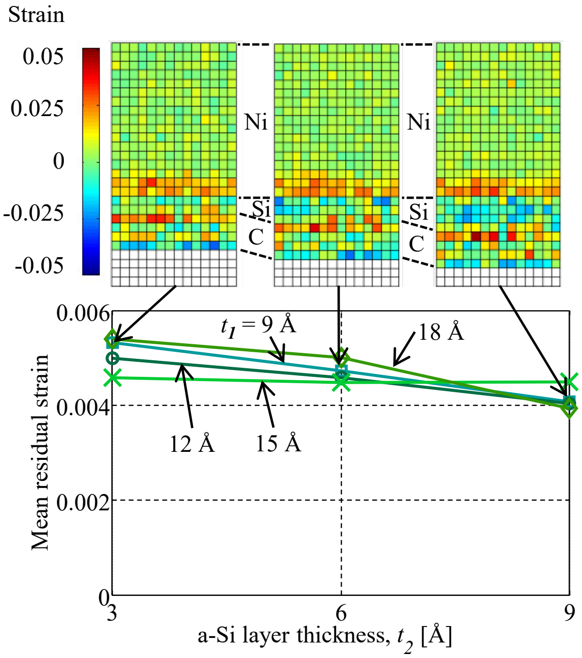

Figure 3.4 Mean residual strain in the recording head as a function of t_2 for different values of t_1. The corresponding plots of local residual strain are shown for the coatings with $t_1 = 9$ Å.

the Ni, a-Si and DLC atomic structures.

3.3.2 Deformation during combined loading

Figure 3.5 shows the instantaneous number of bonds for each bond type in the MD model, normalized with the initial number of bonds of that type, as a function of time during the combined loading simulation, for a DLC coating with $t_1 = 12$ Å and $t_2 = 3$ Å, and for contact pressure $p_c = 48$ GPa (Figure 3.5 (a)) and 64 GPa (Figure 3.5 (b)). The five steps shown in Figure 3.2 are represented by three regions in Figure 3.5. Region I corresponds to the initial equilibration and normal loading steps, region II corresponds to the combined normal and tangential loading, and region III corresponds to the unloading and separation steps. We observe that deformation occurs primarily in the Ni-Ni, Ni-Si,

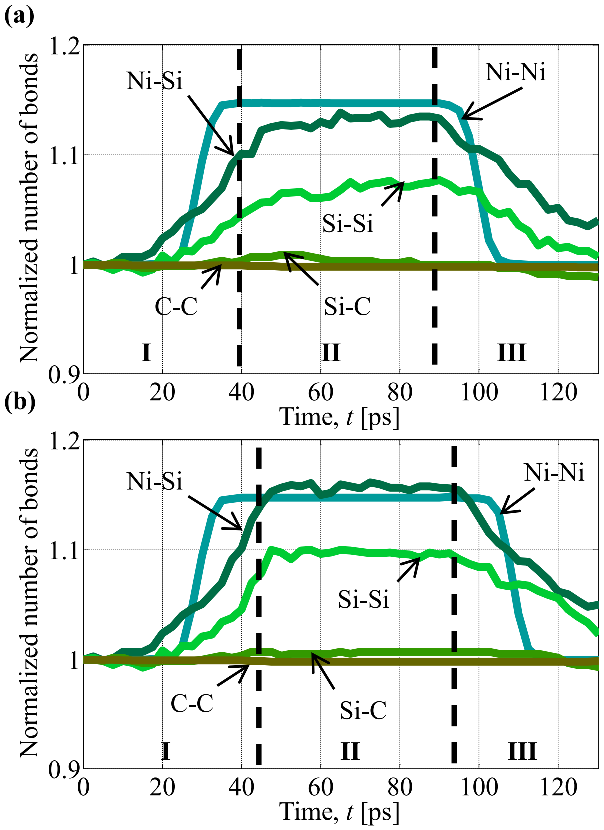

Figure 3.5 Instantaneous number of bonds of each bond type. Shown for a coating with t_1 = 12 Å and t_2 = 3 Å, normalized with the initial number of bonds of that type, versus time, for (a) p_c = 48 GPa and (b) p_c = 64 GPa

and Si-Si bonds during combined normal and tangential loading of the multilayer DLC coating by the moving counterface because these bond types display the lowest cohesive energies of the different bond types in the recording head (see Table 3.1) and thus, are easiest to deform. Although Ni-Ni bonds have the lowest cohesive energy, crystalline structures show higher intrinsic resistance to deformation compared to amorphous structures [27]. Hence, we observe deformation of the Ni-Si and Si-Si bonds before Ni-Ni bonds. As the load on the Ni substrate increases, the distance between second-nearest neighbor atoms is reduced such that it falls within the first-nearest neighbor atom cutoff. This results in the steep increase in Ni-Ni bonds in region I (Figure 3.5). The amorphous structure of the a-Si layer results in a gradual deformation of the Ni-Si and Si-Si bond types that increases with increasing contact pressure, as observed in Figure 3.5 (a) and (b). Limited deformation is observed in the Si-C interface and negligible deformation in the DLC layer. However, the normalized number of Si-C bonds is less than one after the combined loading procedure, indicating that there is a net loss of bonds and that this interface has therefore been weakened by the loading. We do not observe wear or delamination of the DLC coating, which is likely due to the extremely short duration of the simulations.

Figure 3.6 shows the instantaneous number of bonds for each bond type in the MD model, normalized with the initial number of bonds of that type, as a function of time during two combined loading and unloading cycles for a DLC coating with t_1 = 12 Å and t_2 = 3 Å, and for contact pressure p_c = 48 GPa. Although the number of bonds during loading are similar in the first and second loading cycles for most bond types, we observe that the number of Si-C bonds decreases with repeated loading/unloading cycles, weakening the interface. The normalized number of Si-C bonds remains less than one

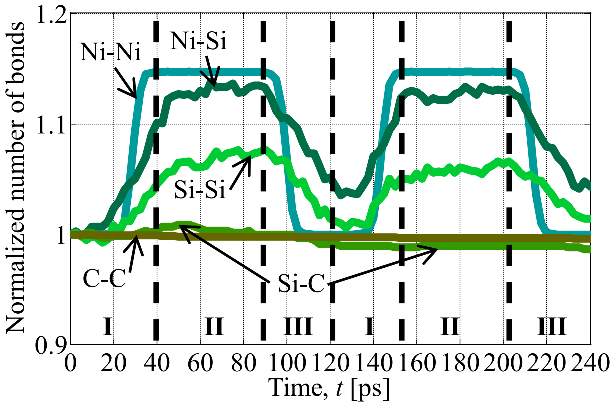

Figure 3.6 Instantaneous number of bonds of each bond type, normalized with the initial number of bonds of that type, versus time. Shown for p_c = 48 GPa during two cycles of combined loading and unloading

throughout the entire second combined loading/unloading procedure, and results in a further loss of nearly 1% of the Si-C bonds. Hence, this indicates that the Si-C damage is irreversible and may eventually lead to wear and delamination of the DLC layer.

Figure 3.7 shows the mean strain in the recording head during combined loading, i.e., calculated during region II in Figure 3.5, as a function of t_2 for different values of t_1 and for p_c = 48 GPa (Figure 3.7 (a)) and 64 GPa (Figure 3.7 (b)), respectively. The mean strain is negative due to compressive normal loading, and the magnitude increases with increasing contact pressure. The mean strain during loading becomes increasingly negative with increasing t_2, similar to the results for the mean residual strain, which decreases with increasing t_2. The higher residual tensile strain in the coatings with thinner

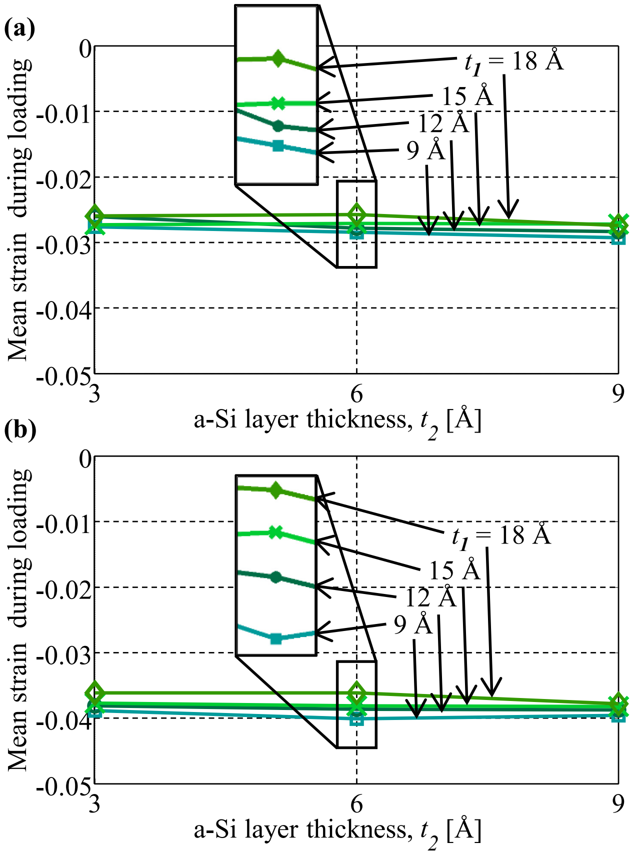

Figure 3.7 Mean strain in the recording head during combined loading. Shown as a function of t_2 for different values of t_1 and for (a) p_c = 48 GPa and (b) p_c = 64 GPa

t_2 counteract the compressive loading, decreasing the deformation caused by compressive loading. Hence, coatings with higher residual tensile strain show less compressive strain during compressive loading. The magnitude of the mean strain during loading also decreases with increasing t_1, indicating that a thick DLC layer prevents deformation of the substrate. Due to the high cohesive energy of C-C bonds (see Table 3.1), the DLC layer can absorb a large amount of energy compared to the rest of the coating without significantly deforming.

3.3.3 Permanent deformation

Permanent deformation of each bond type in the recording head is quantified as the final number of bonds after combined loading relative to the initial number of bonds of that type. Figure 3.8 (a), (b), and (c) shows the normalized final number of Ni-Si, Si-Si, and Si-C bonds, respectively, as a function of t_2, for different values of t_1 and for p_c = 64 GPa. In each case, the final number of Ni-Si and Si-Si bonds increases by 0 - 6% compared to the initial number of bonds, signifying strengthening of the Ni-Si interface. The final number of Si-C bonds changes by ±2% compared to the initial number of bonds indicating that in certain cases the Si-C interface is strengthened, and, in other cases, it is weakened by the combined external loading. During simulations with two combined loading cycles, such as the results shown in Figure 3.6, we observe a decrease in the number of Si-C bonds after two loading cycles compared to one, indicating permanent deformation that accumulates each loading cycle and eventually will lead to wear and delamination between the Si and DLC coating layers. The permanent deformation of the Ni-Si, Si-Si, and Si-C bonds seems nearly independent of t_1 and t_2 for the cases investigated, especially in light of the stochastic nature of the MD simulations. The

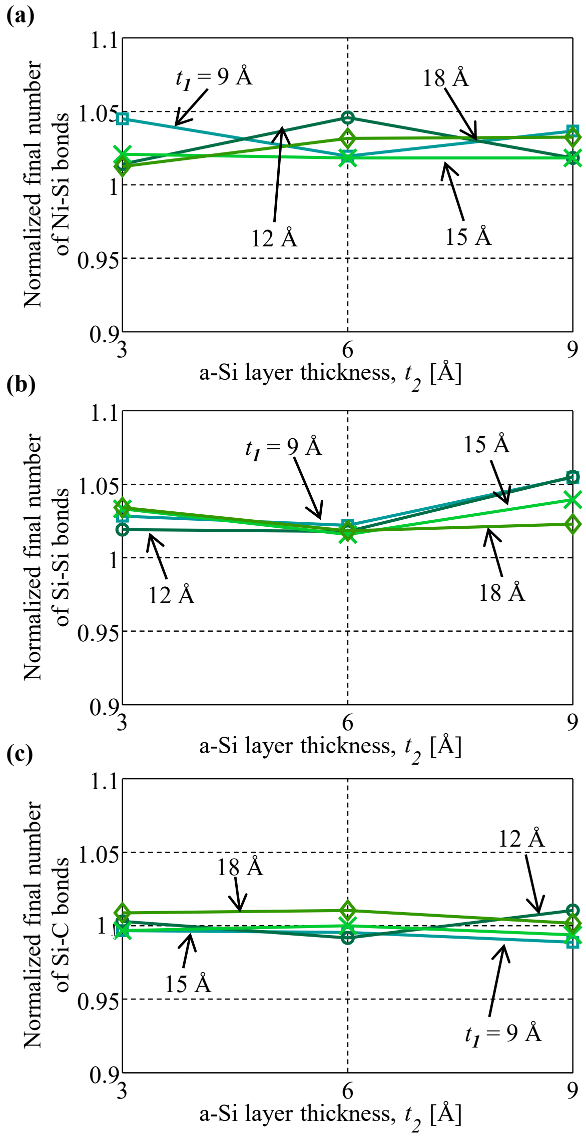

Figure 3.8 Final number of bonds. Final number of (a) Ni-Si bonds, (b) Si-Si bonds, and (c) Si-C bonds as a function of t_2 for different values of t_1, for the case of $p_c = 64$ GPa. The final number of bonds has been normalized with the initial number of bonds.

remaining bond types in the model, Ni-Ni and C-C, show negligible permanent deformation, and are therefore not shown in Figure 3.8. The C-C bonds have the highest cohesive energy compared to the other bond types and thus, no permanent deformation is observed. The increase in the Ni-Ni bonds during loading, due to the temporary close proximity of second-nearest neighbor atoms, is purely elastic and fully recovered once the compressive loading is removed and the Ni atoms relax back into their equilibrium positions in the FCC lattice. It is the amorphous structure of the Ni-Si and Si-C interfaces and the a-Si layer in combination with the relatively low cohesive energies of those bond types that cause the only significant permanent deformation to occur in the Ni-Si and Si-Si bonds and to a lesser extent, Si-C bonds.

Figure 3.9 shows the normalized final bond energy as a function of t_2 for different values of t_1 and for p_c = 64 GPa, normalized with the initial bond energy. It is a measure of the total permanent deformation in the coating, i.e., the change in energy due to the deformation of the individual bond types shown in Figure 3.7 (a)-(c). The final bond energy increases with increasing t_2 and decreasing t_1. The increase in final bond energy with increasing t_2 indicates that a thicker a-Si layer deforms more than a thinner a-Si layer at a given contact pressure. This deformation is due to the a-Si layer being the amorphous layer with the lowest cohesive energy. The increase in final bond energy with decreasing t_1 agrees with the results shown in Figure 3.7 and indicates that increasing t_1 improves protection of the substrate due to the high C-C cohesive energy. The effect of t_1 increases with increasing t_2, which indicates that decreasing the DLC layer thickness has

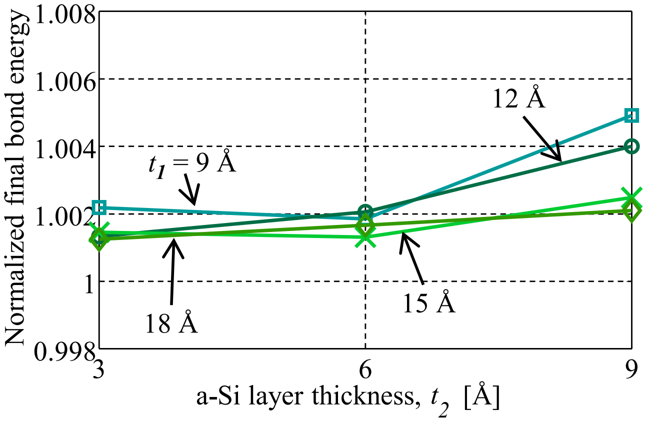

Figure 3.9 Final bond energy normalized with the initial bond energy as a function of t_2 for different values of t_1.

a bigger effect with increasing a-Si layer thickness. Thus, to optimize the strength of a DLC coating for a given coating thickness budget, it seems more effective to decrease t_2 before decreasing t_1.

3.4 Conclusions

We have investigated the deformation of the ultra-thin multilayer DLC coating during combined normal and tangential loading against a moving, rigid hydrogen-terminated diamond counterface, simulating accidental contact between a recording head and magnetic disk of an HDD. The mean residual strain in the recording head before loading decreases with increasing a-Si layer thickness but is independent of the DLC layer thickness, indicating that a thicker a-Si layer is desirable for reducing residual strain in the recording head. Deformation during combined loading and sliding occurs primarily in the Ni-Ni, Ni-Si, and Si-Si interactions, and is a function of the cohesive energy and atomic structure of the layers. This deformation increases with decreasing DLC layer thickness, indicating that a thicker DLC layer is desirable for protecting the recording head during combined loading and sliding contact. Permanent deformation is observed primarily in the Ni-Si and Si-C interfaces and in the a-Si layer and is also a function of the cohesive energy and atomic structure of the layers. Permanent loss of interatomic bonds between material layers is only observed in the Si-C interface, and increases with additional combined loading cycles. The total permanent deformation of the DLC coating increases with increasing a-Si layer thickness and decreasing DLC layer thickness. Hence, to minimize deformation of the DLC coating under combined loading, for a given coating thickness budget, it is preferable to decrease the thickness of the a-Si layer before decreasing the thickness of the DLC layer.

3.5 References

1. Prabhakaran, V., Talke, F.E.: Wear and hardness of carbon overcoats on magnetic recording sliders. Wear. **243**, 18–24 (2000)

2. Lee, K.M., Yeo, C.D., Polycarpou, A.: Nanomechanical property and nanowear measurements for Sub-10-nm thick films in magnetic storage. Exp. Mech. **47**, 107–121 (2007)

3. Zhong, M., Zhang, C., Luo, J., Lu, X.: The protective properties of ultra-thin diamond like carbon films for high density magnetic storage devices. Appl. Surf. Sci. **256**, 322–328 (2009)

4. Yasui, N., Inaba, H., Furusawa, K., Saito, M., Ohtake, N.: Characterization of head overcoat for 1 Tb/in^2 magnetic recording. IEEE Trans. Magn. **45**, 805–809 (2009)

5. Ma, T.-B., Hu, Y.-Z., Wang, H.: Molecular dynamics simulation of shear-induced graphitization of amorphous carbon films. Carbon N. Y. **47**, 1953–1957 (2009)

6. Gao, G.T., Mikulski, P.T., Harrison, J. a: molecular-scale trobology of amorphous carbon coatings: effects of film thickness, adhesion, and long-range interactions. J. Am. Chem. Soc. **124**, 7202–7209 (2002)

7. Wang, N., Komvopoulos, K.: Nanomechanical and friction properties of ultrathin amorphous carbon films studied by molecular dynamcs analysis. ASME Conf. Proc. **2010**(44199), 393–395 (2010)

8. Glosli, J.N., Belak, J., Philpott, M.R.: Ultra-thin carbon coatings for head-disk interface tribology. Mater. Res. Soc. Symp. Proc. **356**, 749–753 (1995)

9. Iwasaki, T., Miura, H.: Analysis of adhesion strength of interfaces between thin films using molecular dynamics technique. Mater. Res. Soc. Symp. Proc. **594**, 377–382 (2000)

10. Baskes, M.I., Angelo, J.E., Bisson, C.L.: Atomistic calculations of composite interfaces. Model. Simul. Mater. Sci. Eng. **2**, 505–518 (1999)

11. Deng, H., Minor, K.M., Barnard, J. a.: Comparison of mechanical and tribological properties of permalloy and high moment fetan thin films for tape recording heads. IEEE Trans. Magn. **32**, 3702–3704 (1996)

12. Ma, Z., Long, S., Pan, Y., Zhou, Y.: Creep Behavior and Its Influence on the Mechanics of Electrodeposited Nickel Films. J. Mater. Sci. Technol. **25**, 90–94 (2009)

13. Frick, C.P., Clark, B.G., Orso, S., Schneider, a. S., Arzt, E.: Size effect on strength and strain hardening of small-scale [1 1 1] nickel compression pillars. Mater. Sci. Eng. A. **489**, 319–329 (2008)

14. Klokholm, E., Aboaf, J. a.: The saturation magnetostriction of permalloy films. J. Appl. Phys. **52**, 2474–2476 (1981)

15. Baskes, M.I.: Modified embedded-atom potentials for cubic materials and impurities. Phys. Rev. B. **46**, 2727–2742 (1992)

16. Tersoff, J.: New empirical approach for the structure and energy of covalent systems. Phys. Rev. B. **37**, 6991–7000 (1988)

17. Stuart, S., Tutein, A., Harrison, J.: A reactive potential for hydrocarbons with intermolecular interactions. J. Chem. Phys. **112**, 6472–6486 (2000)

18. Plimpton, S.: Fast parallel algorithms for short-range molecular dynamics, J. Comp. Phys. **117**, 1-19 (1995)

19. Song, D., Kvitek, R., Schnur, D.: Inspection of pole tip diamondlike carbon wear due to heater-induced head-disc contact. J. Appl. Phys. **99**, 2004–2007 (2006)

20. Mate, C.M., Arnett, P.C., Baumgart, P., Dai, Q., Guruz, U.M., Knigge, B.E., Payne, R.N., Ruiz, O.J., Wang, G.J., Yen, B.K.: Dynamics of contacting head-disk interfaces. IEEE Trans. Magn. **40**, 3156–3158 (2004)

21. Lide, D.R.: A survey of carbon-carbon bond lengths. Tetrahedron. **17**, 125–134 (1962)

22. Bylander, D.M., Kleinman, L., Mednick, K.: Self-consistent energy bands and bonding of Ni_3Si. Phys. Rev. B. **25**, 1090–1095 (1982)

23. Bylander, D.M., Kleinman, L., Mednick, K., Grise, W.R.: Self-consistent energy bands and bonding of $NiSi_2$. Phys. Rev. B. **26**, 6379–6383 (1982)

24. Zirkelbach, F.: Atomistic simulation study on silicon carbide precipitation in silicon, (2011)

25. Bekaroglu, E., Topsakal, M., Cahangirov, S., Ciraci, S.: First-principles study of defects and adatoms in silicon carbide honeycomb structures. Phys. Rev. B - Condens. Matter Mater. Phys. **81**, 1–10 (2010)

26. Chelikowsky, J.R., Louie, S.G.: First-principles linear combination of atomic orbitals method for the cohesive and structural properties of solids: Application to diamond. Phys. Rev. B. **29**, 3470–3481 (1984)

27. Szlufarska, I., Kalia, R.K., Nakano, A., Vashishta, P.: A molecular dynamics study of nanoindentation of amorphous silicon carbide. J. Appl. Phys. **102**, 023509:1-9 (2007)

28. Robertson, J.: Diamond-like amorphous carbon. Mater. Sci. Eng. R Reports. **37**, 129–281 (2002)

CHAPTER 4

QUANTIFYING DELAMINATION OF ULTRA-THIN MULTILAYER DLC COATINGS FROM THEIR SUBSTRATE USING MOLECULAR DYNAMICS SIMULATION

Modified from [Price, M. R., Raeymaekers B.: Quantifying adhesion of ultra-thin multilayer DLC coatings to Ni and Si substrates using shear, tension, and nanoscratch molecular dynamics simulations. Acta Mater. **141**, 317-326 (2017)]. © Elsevier 2017

4.1 Introduction

One of the primary challenges in determining the atomistic mechanisms of delamination of an ultra-thin DLC coating is the time and length scales over which it occurs. No experimental techniques exist that can directly observe the motion of atoms that leads to delamination, but delamination is a process that occurs over time scales that are not feasible to model with MD. Although simulation results such as those discussed in Chapters 2 and 3 provide knowledge about how ultra-thin multilayer DLC coatings deform due to external loading and are useful in predicting which coating parameters are important in preventing the plastic deformation that may lead to wear or delamination, they do not actually model separation of the coating from the substrate. Hence, this chapter builds upon the results of the previous chapters and the experimental and simulated methods and results of many previous studies that investigate combined normal and tangential loading of ultra-thin DLC coatings and attempt to extend their longevity by quantifying and preventing or postponing delamination of the coating from the substrate.

A common experimental technique to quantify adhesion of a coating to its substrate is the nanoscratch test, in which a hard indenter tip is moved tangentially across the surface under a constant or steadily increasing load until coating failure occurs [1]. Coating failure may occur as radial cracking, through-thickness cracking, permanent deflection of the coating, delamination, or a combination of these mechanisms, depending on the hardness of the coating and substrate, thickness of the coating, and chemical adhesion between coating and substrate [1,2]. Determining the mechanisms of coating failure and quantifying the adhesion strength of the coating to the substrate is accomplished by analyzing changes in the normal load, tangential load, indenter depth, and friction coefficient during the scratch, and by examining the surface of the coating after the scratch to determine the scratch profile and the size, shape, and composition of any debris generated by the scratch. Nanoscratch tests show that failure of ultra-thin DLC coatings is determined primarily by the amount of plastic deformation in the substrate [3], which may lead to cracking and delamination of the coating [4,5]. Furthermore, adhesion of DLC coatings to the substrate depends on external load, residual stress in the coating, coating and substrate composition, and coating thickness [5–7].

Researchers have proposed a number of techniques to prevent, reduce, or postpone delamination of ultra-thin DLC coatings under external loading by reducing the residual stress in the DLC and improving adhesion of the DLC coatings to the substrate. Some of these techniques, such as carbon ion implantation into the substrate before coating deposition [8,9], modifying coating deposition parameters [10,11], doping the DLC [12–14], tuning the substrate temperature during deposition [15], and thermal annealing of coating and substrate after coating deposition [14,16] can change the mechanical properties of the coating and reduce its ability to protect the substrate, or can directly damage the substrate through ion bombardment, melting, or increased diffusion between regions of different materials [8,10,11,14,16]. Thus, these techniques are inadequate when such damage compromises the function of delicate substrate materials and nanostructures. Other techniques improve adhesion without affecting the mechanical properties of the DLC coating material or damaging the substrate, such as including nanocrystals of a metallic phase within the DLC coating [17–19], deposition of an intermediate layer between the DLC and the substrate [20–22], deposition of multiple, alternating layers of hard DLC and a softer material such as a metal or a softer DLC [21,23–25], or creating a composition gradient between the substrate and the DLC coating [21,26,27]. However, it is difficult to theoretically predict and experimentally determine how the different materials deform under external loading, and understand how that deformation leads to delamination, particularly when the coatings are several nanometers thick and the deformation of the coating is dominated by atomic-scale effects.

Molecular dynamics (MD) simulations have been used to simulate deformation and adhesion of ultra-thin multilayer coatings under combined normal and tangential loading. MD simulations of nanoscratch tests [28,29] and other normal and tangential loading cases [30–33] of DLC coatings provide descriptions of the change in atomic structure near the surface of the coating due to loading [28–30], the adhesion between the DLC coating and the contacting surface [31,32], and the friction coefficient during sliding [33]. However, these studies model either DLC only or a single-layer DLC coating on a substrate, and do not investigate adhesion of the DLC coating to the substrate. Other MD studies quantify adhesion between different materials or multiple layers in a coating, and find that MD correctly predicts the qualitative trends of adhesion strength between different materials [34–37]. However, the materials modeled are typically crystalline metals rather than amorphous DLC. No studies exist that evaluate atomic-scale deformation of an ultra-thin multilayer DLC coating under combined normal and tangential loading, to provide design guidelines to minimize deformation and delamination of the DLC coating for a given set of loading conditions. Hence, the objective of this chapter is to fill this gap and determine the effect of coating design parameters of an ultra-thin multilayer DLC coating, including thickness and composition of the layers, on the adhesion of the coating to the substrate. This will provide an understanding of how ultra-thin multilayer DLC coatings deform and separate from the substrate under external loading, and provide information on how to design DLC coatings to facilitate their use in engineering applications.

4.2 Methods

4.2.1 Model

We model the ultra-thin DLC coating of an HDD recording head, which contains an sp^3-fraction of approximately 70 % (i.e., tetrahedral amorphous carbon, ta-C [38]) and protects the magnetic read/write components from wear and delamination due to accidental contact with the disk [39,40]. Figure 4.1 shows the MD model of a small portion of the recording head, indicated by a red rectangle in Figure 1.6. The MD model consists of a Ni substrate of thickness t_{sub} and a multilayer DLC coating consisting of a DLC layer of thickness t_1 and an a-Si layer of thickness t_2. We model the top pole permalloy substrate material as Ni to simplify the computational model. Although the

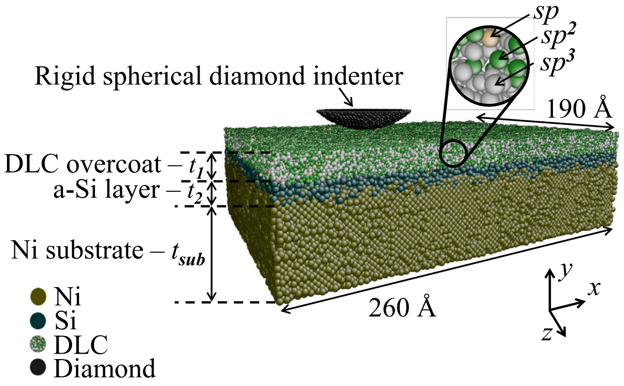

Figure 4.1 MD model of a small portion of the recording head, indicated by the red rectangular box in Figure 1.6.

magnetic properties of permalloy and Ni are different, their mechanical properties including hardness, Young's modulus, Poisson's ratio, and lattice structure are similar [41–44]. We model the rigid, spherical indenter with C atoms in a diamond lattice, and select the indenter tip radius of $r = 40$ Å and simulation volume of 260 x 100 x 190 Å^3 after a convergence study to ensure that boundary effects of the simulation box are negligible.

Figure 4.2 shows a schematic of the four different combinations of coating and substrate materials used in this study. We vary the thickness and composition of the coating layers t_1 and t_2 to systematically investigate their effect on adhesion of the coating to the substrate, which we measure as the force required to separate the coating from the substrate under tension or shear loading. Coating type I is similar to the DLC coating on a recording head in an HDD (Figure 4.1). We compare coating type I to type II to evaluate the effect of DLC sp^3 fraction on adhesion to the substrate. Coating types III-A and III-B are ta-C coatings on Ni and crystalline Si substrates, respectively, with a-C rather than a-Si as the material of the intermediate coating layer. We compare coating type III-A to type I to determine how adhesion of DLC coatings can be improved by modifying the properties of the DLC itself without the need for an intermediate layer of a different

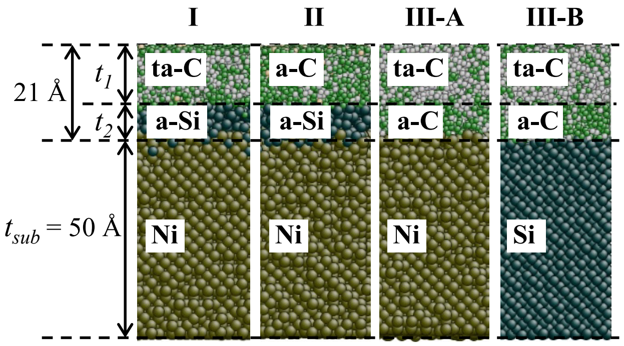

Figure 4.2 Different combinations of coating and substrate materials used in this study.

chemical composition, as observed by Anders et al. and Logothetidis et al. [23,25]. Additionally, we replace the Ni substrate (type III-A) with crystalline Si (type III-B), a substrate commonly used in MEMS devices, to compare the effect of substrate material on the adhesion of DLC coatings as a function of coating layer thickness. DLC is known to display strong adhesion to Si and weak adhesion to Ni [7].

We vary the thickness of the coating layers, $12 \leq t_1 \leq 21$ Å and $0 \leq t_2 \leq 9$ Å, while maintaining a constant total coating thickness of $t_1 + t_2 = 21$ Å, which is similar to the thickness of the protective coating on the recording head of an HDD. The substrate thickness t_{sub} remains 50 Å throughout this chapter. We use the following interatomic potentials in the MD model: MEAM [34,45,46] for Ni-Ni, Ni-Si, and Ni-C interactions and Tersoff [47] for Si-Si, Si-C, and C-C interactions except for the C-C interactions between the indenter tip and the coating, for which we use a Morse potential parameterization that has been used to describe the interactions between a diamond indenter and substrate during nanoscratch simulations, with $D = 0.435$ eV, $\alpha = 4.65$ Å, and $r_0 = 1.95$ Å [48]. We overlap the MEAM and Tersoff potentials at the corresponding material interfaces to account for the many-body terms of the potentials as described in Section 1.4.3. The model consists of approximately 330,000-450,000 atoms depending on coating thickness and composition. We use the Sandia LAMMPS code [49] for the MD simulations with a time step of 0.25 fs for all simulations.

We use a multistep annealing procedure to create the MD model similar to the single-step annealing procedure used by others to create DLC [31,50]. We create a 260 x 30 x 190 Å^3 block of DLC by heating diamond to 6000 K and rapidly quenching it, while controlling the pressure to tune the density and thus, the sp^3 fraction of the DLC. We use a similar annealing procedure to create a block of a-Si. We merge the material blocks to create a single- or multilayer coating ($t_2 = 0$ or $t_2 > 0$, respectively) on a substrate of crystalline Ni or Si, and perform the annealing procedure at the interface between the different material layers. We create coatings with layers of different thickness by removing atoms from the middle of each coating layer and annealing the layer back together. This procedure ensures that the atomic structure of the DLC coating surface and of the interfaces between material layers, including diffusion of atomic species into neighboring layers, are identical for all simulations. Thus, the simulation results are only dependent on the change in coating design parameters (e.g., layer thickness) and not on stochastic variation of the atomic structure at the material interfaces or surface of the DLC layer.

4.2.2 Simulation procedure

Figure 4.3 shows the three different simulation procedures used in this work, including simple shear, simple tension, and nanoscratch simulations to quantify the effect of simple and combined normal and tangential loading on the adhesion of the coating to the substrate. Figure 4.3 (a) illustrates the nanoscratch simulation procedure, similar to that used in other studies [51,52]. We press the indenter into the coating (v_y = -50 m/s) until reaching an indentation energy of 2700 eV, identical for all nanoscratch simulations. We then translate the indenter tangentially across the coating over a distance of 84.5 Å (v_x = 50 m/s). Finally, we remove the indenter from the coating (v_y = 50 m/s). 50 m/s is faster than what is typical for nanoindentation and nanoscratch experiments, but corresponds to the maximum relative velocity between the head and disk in an HDD [53]

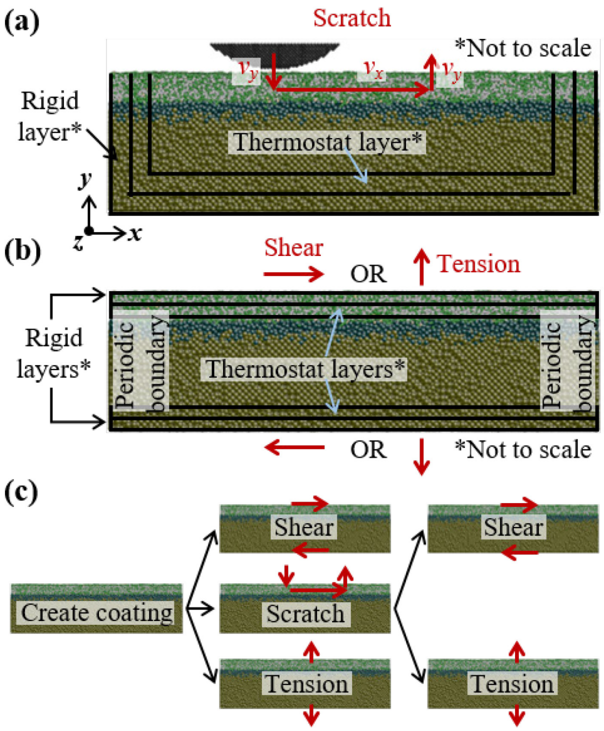

Figure 4.3 Schematic of the simulation procedures used. (a) Nanoscratch simulation procedure. (b) Shear and tension simulation procedure. (c) Schematic of the process for performing shear, tension, and nanoscratch simulations for each coating.

and falls within the range of indenter displacement rates used in other MD nanoscratch simulations, 20 m/s to 500 m/s (see e.g. [52,54–56]). Throughout the nanoscratch simulation, we hold the outer atomic layers along the sides and bottom of the simulation box rigid and maintain the next atomic layers inward at 300 K using a Langevin thermostat to simulate the bulk material around the simulation volume.

Figure 4.3 (b) shows the simulation procedure for simulating simple tension or shear loading, similar to the procedure used in other MD studies [56–58]. We hold the outer atomic layers in the *y*-direction rigid at the top and bottom of the coating and substrate, respectively, and maintain the next atomic layers inward at 300 K using a Langevin thermostat. For tension loading simulations, we move the upper rigid section of the coating upward (50 m/s) until the coating has fully separated from the substrate. For the shear loading simulations, we move the upper rigid section of the coating 20 Å in the *x*-direction (50 m/s). Because the simulation box boundaries are periodic in the *x*- and *z*-directions, the shear loading simulations do not fully separate the coating from the substrate, and bonds between atoms that are broken due to shear loading can be replaced by bonds between different atoms.

Figure 4.3 (c) shows a schematic of the process for performing simple shear, simple tension, and nanoscratch simulations for each coating of the desired coating composition and thickness. We perform independent shear, tension, and nanoscratch simulations on the coating, then perform second shear and tension simulations on the coating after it has undergone a nanoscratch simulation. A single scratch is insufficient to cause complete delamination of a DLC coating from the substrate, which typically only occurs after many cycles (see, e.g., [59]). Hence, we compare the shear and tension simulation results before and after the nanoscratch simulation to determine the damage and to evaluate which design parameters are most important in preventing damage that may lead to future delamination due to the combined normal and tangential loading (scratch).

4.2.3 Data analysis

Figure 4.4 shows a typical result of the *x*-force during shear loading and *y*-force during tension loading as a function of time for a ta-C and a-Si coating on a Ni substrate (type I) with t_2 = 3 Å. Following an initial equilibration period, shear or tension of the coating begins at time t_0. During shear simulations, the coating deforms until a maximum force F_{max} occurs at time t_{max}, at which point a shear band develops near the coating-substrate interface, the shear force decreases, and the coating begins to move in the *x*-

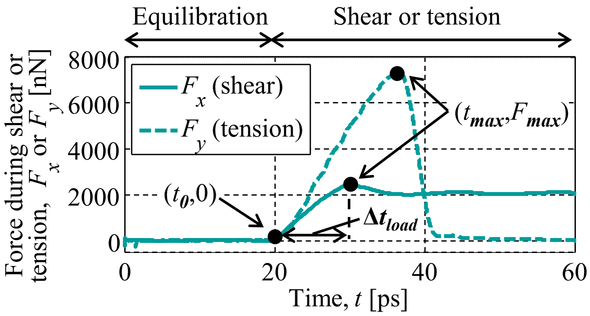

Figure 4.4 x-force during shear and y-force during tension as a function of time. Shown for a ta-C and a-Si coating on a Ni substrate (type I) with an intermediate a-Si layer of thickness $t_2 = 3$ Å.

direction. During tension simulations, the tension force decreases to zero after reaching F_{max} due to the complete separation of the coating from the substrate. Similar behavior is seen for all coatings. We compare F_{max} under shear and tension loading for different coating designs to determine the effect of coating design parameters on a coating's resistance to shear and tension loading. We compare F_{max} under shear and tension loading for the same coating, before and after a nanoscratch simulation, to determine the effect of coating design parameters on deformation due to combined normal and tangential loading. We calculate the critical mean shear strain γ_{crit}, defined as the shear strain at the inception of coating separation during the shear simulations, as $\gamma_{crit} = v_x(\Delta t_{load})/l_x$, where v_x is the shear velocity, Δt_{load} is the time between t_0 and t_{max}, and l_x is the length of the simulation box in the x-direction, and compare the effect of coating design parameters on the local displacement required for coating separation and thus, on the elasticity of the coating.

We quantify local shear strain by discretizing the simulation volume into grid elements and calculating a local average of the atomic bond rotation angle (ABRA). ABRA is a measure of the angle that a bond between two atoms has been rotated when atoms have been displaced due to loading, and is an indication of local shear strain [57]. Figure 4.5 (a) shows a schematic of the three-dimensional simulation volume discretization technique we use to calculate the average ABRA within each grid element. Each bond that exists at the beginning and end of the simulation contributes to the average ABRA for the grid element in which the bond's midpoint is located. Two atoms are considered to be bonded when the distance between them is less than a cutoff determined using the first minimum in the radial distribution function for the given bond type [31,60], including Ni-Ni, Ni-Si, Ni-C, Si-Si, Si-C, and C-C bonds. Figure 4.5 (b) shows a schematic of the one-dimensional simulation volume discretization technique that we use to quantify how properties including energy per atom, volume per atom, and bond length vary with coating depth and thus, due to changes in layer composition and

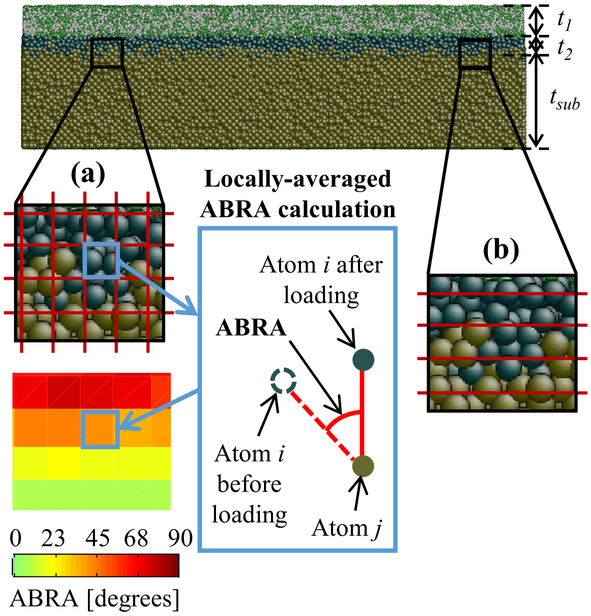

Figure 4.5 Simulation volume discretization techniques. (a) Schematic of the three-dimensional simulation volume discretization technique for calculating local averages of ABRA. (b) one-dimensional simulation volume discretization technique for quantifying how coating properties including energy per atom, volume per atom, and bond length vary with coating depth.

thickness.

4.3 Results and discussion

We have simulated simple shear, simple tension, and nanoscratch procedures for the coatings shown in Figure 4.2, to determine the effect of coating layer thickness and *sp*^{3} fraction on the adhesion of the coating to the substrate, and plastic deformation of the substrate. Although we model a particular application of ultra-thin DLC coatings for HDDs, the results find use in a wide range of applications in which similar protective coatings are used.

We first evaluate the effect of coating composition, including thickness of an intermediate a-Si layer, and the *sp*^{3} fraction of the DLC layer, on the adhesion of the DLC coating to the substrate, by determining the maximum force required to remove the coating from the substrate. Figure 4.6 shows the force F_{max} to separate ta-C (70% *sp*^{3}, type I) and a-C coatings (30% *sp*^{3}, type II) from a Ni substrate under shear loading (dashed line) and tension loading (solid line), as a function of the thickness of the

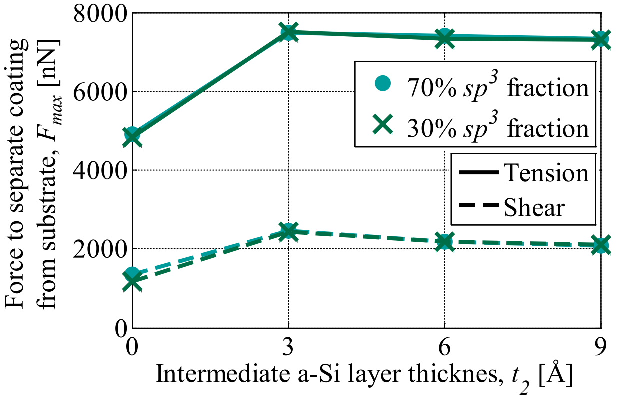

Figure 4.6 Force to separate ta-C and a-C coatings from a Ni substrate (types I and II) under shear and tension loading. Shown as a function of the thickness of the intermediate a-Si layer, and the *sp*^{3} fraction of the DLC coating.

intermediate a-Si layer, t_2. We observe that F_{max} is independent of the sp^3 fraction of the DLC layer over the range of parameters investigated. We also note that F_{max} is greater with an intermediate a-Si layer than without, and that for the coatings with an intermediate a-Si layer, F_{max} increases with decreasing intermediate layer thickness. This indicates that the presence of the a-Si layer improves the adhesion of DLC coatings to the Ni substrate, in agreement with the experimental observations by Holleck and Schier [61] and Li et. al. [27]. Furthermore, the results indicate that an optimum thickness of the intermediate a-Si layer exists.

Figure 4.7 shows the effect of the a-Si layer on the atomic structure of the Ni substrate near the coating-substrate interface to explain why the intermediate a-Si layer is critical for improving adhesion of a DLC coating to a Ni substrate. Figure 4.7 (a) shows a close-up view of the coating-substrate interface for a ta-C coating (type I) without and with an intermediate a-Si layer (t_2 = 0 Å and 3 Å, respectively). The Ni lattice is less apparent near the interface with ta-C than near the interface with a-Si, indicating that below the coating without an intermediate a-Si layer, the Ni atoms are further away from their equilibrium lattice positions compared to the coatings with an intermediate Si layer. This qualitative observation is quantified in Figure 4.7 (b), which shows the deviation from equilibrium of the energy per Ni atom, volume per Ni atom (estimated using the Voronoi algorithm [62]), and Ni-Ni bond length as a function of depth into the Ni substrate for the coatings shown in Figure 4.7 (a). We observe that the Ni substrate without an intermediate a-Si layer displays deviations from equilibrium ranging between -20% and 10% for energy per Ni atom, volume per Ni atom, and Ni-Ni bond length that penetrate > 7 Å into the substrate, whereas the Ni substrate with an intermediate a-Si

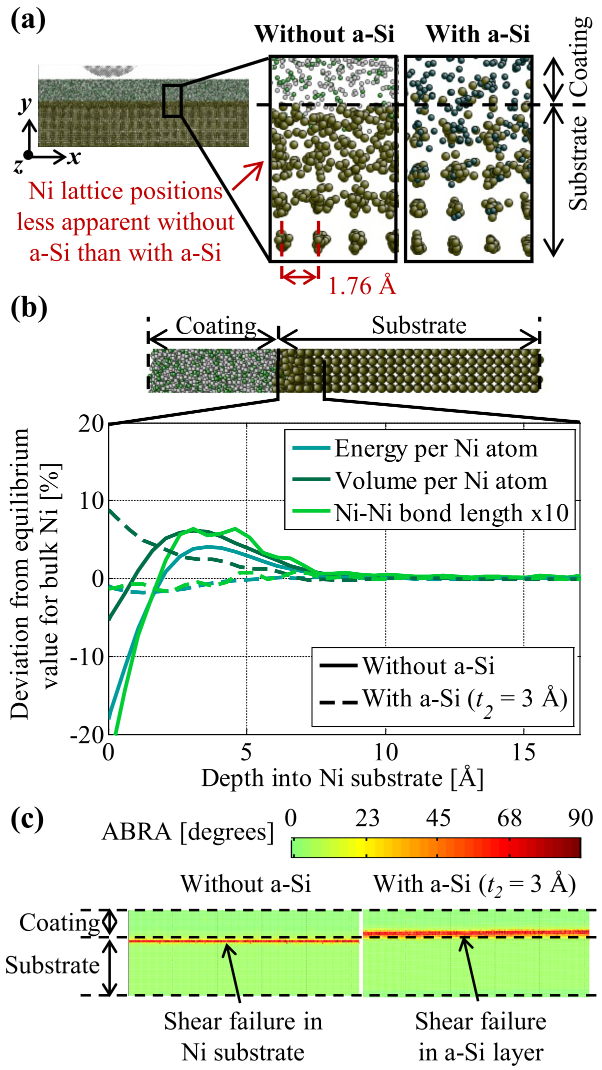

Figure 4.7 The effect of the a-Si layer on the atomic structure of the Ni substrate. (a) Close-up view of the coating-substrate interface for a ta-C coating without Si compared to with Si. (b) Deviation from equilibrium of the energy per Ni atom, volume per Ni atom, and Ni-Ni bond length as a function of depth into the Ni substrate for the coatings shown in (a). (c) Locally averaged ABRA for the coatings shown in (a).

layer shows deviation of < 3% from equilibrium except in volume per Ni atom, which increases near the coating-substrate interface. This is due to the existence of a FCC phase of Ni_3Si with a Ni-Si bond length that differs from the Ni-Ni bond length of the FCC Ni substrate by 3.4%, which is much less than the 18-22% difference between Ni-C and Ni-Ni bonds in their respective equilibrium atomic structures [34,46,63,64]. Thus, the presence of the intermediate a-Si layer causes the Ni lattice to be less distorted than when no intermediate a-Si layer is present.

Figure 4.7 (c) shows the locally-averaged ABRA for the coatings shown in Figure 4.7 (a) resulting from the shear loading described in Section 4.2.2. We observe permanent shear strain in the intermediate layer between Si atoms for all coatings with an intermediate a-Si layer, but in the substrate between Ni atoms for the coatings without an intermediate a-Si layer. This corresponds to the location of maximum deviation from equilibrium in energy per Ni atom, volume per Ni atom, and Ni-Ni bond length (see Figure 4.7 (b)). Therefore, coating failure without an intermediate a-Si layer occurs in the Ni substrate under lower shear and tensile loading than it would occur in an undistorted Ni lattice, or in the intermediate a-Si layer when it is present (see Figure 4.6).

Figure 4.8 shows a cross-section of the coating and substrate of a type I coating, and explains why the coatings with the thinnest intermediate a-Si have the greatest resistance to shear and tension loading (see Figure 4.6). Figure 4.8 (a) shows a snapshot of a typical shear simulation before and after shearing of a type I coating with t_1 = 30 Å and t_2 = 15 Å. We show a coating with a thickness greater than 21 Å for clarity of describing features that are not readily visible when $t_2 \leq 9$ Å. Atoms are colored as labeled in Figure 4.1 except for a thin band of atoms colored red according to their initial x-coordinate, to illustrate how each layer of the coating deforms due to shear loading. We observe that the Ni substrate and ta-C layer are unaffected by shear loading, but that the intermediate a-Si layer slips near the Ni-Si interface, and that the remainder of the intermediate a-Si layer has also plastically deformed, as evidenced by the position of the red-colored atoms. Figure 4.8 (b) shows the composition of the coating, the x-displacement of the atoms, and the normalized curvature of the x-displacement after shear

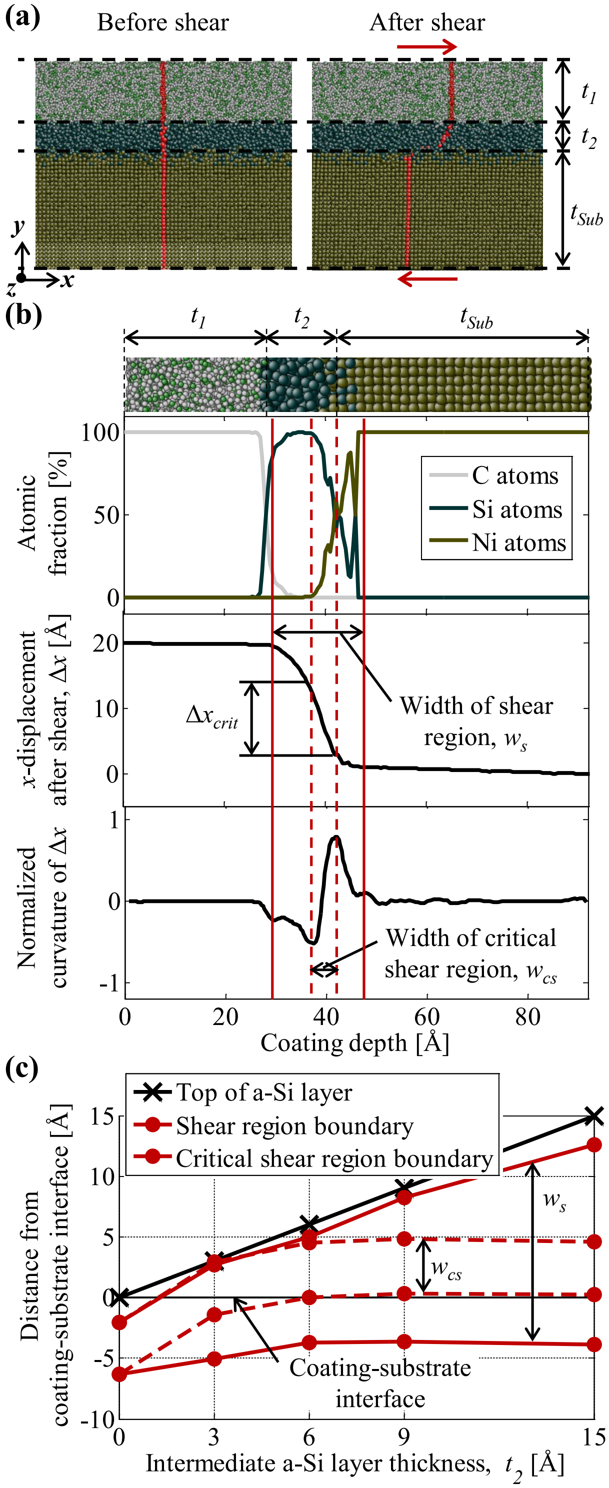

Figure 4.8 Shear failure region during shear loading. (a) Snapshot of shear simulation before and after shearing a type I coating with t_1 = 30 Å and t_2 = 15 Å. (b) Composition, *x*-displacement during shear, and curvature of *x*-displacement normalized by its maximum value as a function of coating depth. (c) Distance from coating-substrate interface of shear region and critical shear region as a function of intermediate a-Si layer thickness.

loading, as a function of coating depth. The sheared region consists of the top atomic layers of the Ni substrate and the entire intermediate a-Si layer apart from the upper portion of the layer that is strengthened by the presence of C atoms. In addition, a critical shear region is defined as the atomic layers of the coating that slip with respect to the stationary substrate due to shear loading. The corresponding displacement Δx_{crit} increases at a rate approximately equal to the shear velocity once the coating is loaded beyond F_{max}. This critical shear region is bound by the global minimum and maximum in the normalized curvature of the x-displacement.

Figure 4.8 (c) shows the distance between the coating-substrate interface and the top and bottom of the shear region and critical shear region as a function of the intermediate a-Si layer thickness. The distance between the top of the intermediate a-Si layer and the coating-substrate interface is also shown. We observe that the thickness of the shear region increases with increasing t_2 and that the thickness of the critical shear region is constant for all coatings investigated. Furthermore, we observe that the shear region and the critical shear region form increasingly deeper below the coating-substrate interface with decreasing t_2 and thus, are comprised increasingly of Ni atoms rather than Si atoms. In the case of $t_2 = 0$ Å, failure under shear loading occurs entirely in the Ni substrate in the region that has been distorted by the Ni-C bonds due to the lack of a stable FCC phase of Ni and C (see Figure 4.7). However, in the case of $t_2 = 3$ Å, the presence of an intermediate a-Si layer of even minimal thickness reduces the Ni lattice distortion at the coating-substrate interface. Thus, the penetration of the critical shear region into the substrate strengthens the critical shear region compared to coatings with $t_2 \geq 3$ Å, and the coating with $t_2 = 3$ Å resists shear and tension loading best of all coatings we have evaluated (see Figure 4.6). The critical shear region makes up a decreasing portion of the total shear region with increasing t_2, and the deformation of the coating under shear loading is increasingly dominated by the properties of a-Si itself and not by the surrounding materials. We observe that the location of coating separation during tension loading occurs at the same location within the coating in which the critical shear region occurs. Furthermore, imperfections in the Ni lattice before loading such as dislocations or grain boundaries, while not modeled in this study, reduce the stress necessary for plastic deformation in the Ni substrate but are not expected to have significant effects on the qualitative behavior of local bonding between ta-C and Ni compared to a-Si and Ni observed in this study.

Continuum mechanisms, in addition to the atomistic mechanisms shown in Figures 4.7 and 4.8, also play a role in the deformation of ultra-thin multilayer DLC coatings and their ability to protect the substrate from plastic deformation. Increasing the thickness of an intermediate layer that has a lower hardness and stiffness than the ta-C layer reduces the hardness and stiffness of the entire multilayer coating, as previously documented via nanoindentation simulations of ultra-thin multilayer DLC coatings in Chapter 2 ([65]). This increases the deformation that occurs in the coating while reducing the deformation that occurs in the substrate and at the coating-substrate interface for a constant external load. Thus, increasing t_2 prevents damage to the substrate caused by an external load. Figure 4.9 (a) shows the percent difference in critical mean shear strain γ_{crit} of a type I, II, or III coating compared to the critical mean shear strain in a coating of the same type without an intermediate a-Si or a-C layer as a function of intermediate layer thickness t_2. We observe that γ_{crit} increases with increasing t_2 for all coating and substrate

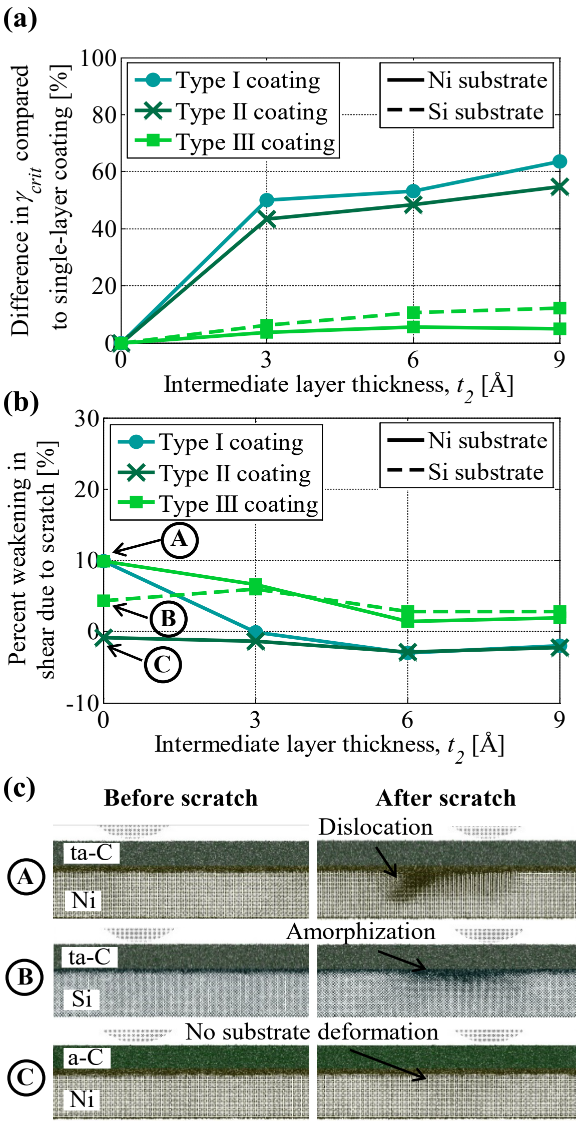

Figure 4.9 Effect of intermediate layer thickness on coating's ability to protect the substrate. (a) Percent difference in critical mean shear strain of type I, II, and III coatings compared to the critical mean shear strain in a single-layer coating of the same type as a function of intermediate layer thickness. (b) Percent weakening under shear loading due to a scratch as a function of intermediate layer thickness. (c) Snapshots of three nanoscratch simulations before and after the scratch for three cases labeled in (b).

combinations evaluated. This is because the a-Si and a-C intermediate layer materials display lower stiffness than ta-C under shear and tension loading [66,67] and thus, the stiffness of the coatings decreases with increasing t_2. Similar behavior is observed for all coatings under tension loading. Figure 4.9 (b) shows the percent weakening under shear loading after performing a nanoscratch simulation, as a function of intermediate layer thickness t_2. Figure 4.9 (c) shows before and after snapshots of the nanoscratch simulations for the cases indicated in Figure 4.9 (b). We observe that the percent weakening under shear loading due to the scratch decreases with increasing t_2, except for the type II coatings, for which a single scratch is insufficient to cause measurable damage with respect to separation of the coating from the substrate. Type II coatings, which consist of a-C and a-Si, are the softest and least stiff of the coatings evaluated and thus, best protect the substrate and coating-substrate interface from plastic deformation, even without an intermediate a-Si layer, as observed in case C of Figure 4.9 (c). This is in agreement with experimental results, which show that coating durability is increased with decreasing stiffness of the intermediate coating layer [59]. Indeed, the scratch slightly compresses the a-Si layer, which increases its density and results in a slight increase of F_{max} under shear loading after the scratch. For type I coatings, the presence of even 3 Å of a-Si is sufficient to protect the substrate from deformation such that no dislocations are emitted from the coating-substrate interface due to the scratch, such as occurs without an intermediate a-Si layer as seen in case A of Figure 4.9 (c). With the addition of a-C rather than a-Si as an intermediate layer, type III coatings with Ni substrates (III-A) do not entirely protect the substrate or coating-substrate interface from plastic deformation over the range of design parameters tested, although the percent weakening due to a scratch decreases with increasing thickness of the a-C layer. In nanoscratch simulations of a type III coating with Si substrate (III-B) we observe amorphization of the Si substrate near the coating-substrate interface, shown in case B of Figure 4.9 (c), which weakens the coatings under both shear and tension loading. The amorphization of the substrate decreases with increasing thickness of the intermediate a-C layer, but we observe from Figure 4.9 (b) that the case with $t_2 = 0$ Å is weakened less by the scratch than the case with $t_2 = 3$ Å. This cannot be explained using continuum theory, but is due to differences between the atomic structure of a-C and ta-C as described below. Furthermore, we note that while decreased hardness and stiffness of DLC coatings may help prevent or postpone delamination from the substrate, the wear rate and friction coefficient of DLC coatings increase with decreasing hardness and stiffness [68], thus a balance must be found based on the design requirements and expected loading conditions of a particular coating. Maximizing the hardness of the outmost coating layer and using intermediate coating layer(s) to improve its adhesion to the substrate appears to be the best way to protect the substrate, similar to findings by Choy and Felix [69].

Figure 4.10 (a) shows the difference between F_{max} of a type III coating and F_{max} of the same coating type without an intermediate a-C layer under shear and tension loading, as a function of the thickness of the intermediate a-C layer. We observe that the force required to separate the coating from the substrate under tension loading is independent of the thickness of the intermediate a-C layer, but that the force required to separate the coatings under shear loading increases with increasing t_2 for type III coatings on Si substrates (III-B) and decreases with increasing t_2 for type III coatings on Ni substrates (III-A). Thus, although the a-C layer increases the elasticity of the coating and prevents

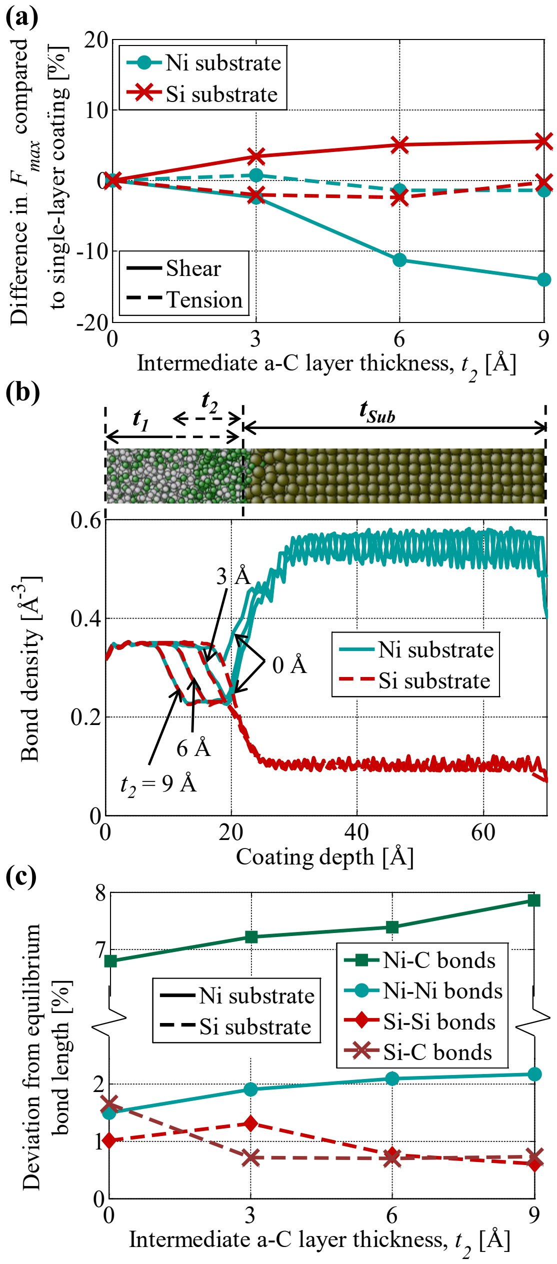

Figure 4.10 Effect of intermediate layer composition on coating adhesion to the substrate. (a) Difference between F_{max} of a type III coating and F_{max} of the same coating type without an intermediate a-C layer under shear and tension loading as a function of the thickness of the intermediate a-C layer. (b) Bond density in type III coatings as a function of coating depth. (c) Deviation from equilibrium of the bond lengths for the interfacial and substrate bonds within 5 Å of the coating-substrate interface for type III coatings before any external loading has been applied.

damage to the substrate due to the scratch for all type III coatings (see Figure 4.9), the presence of the a-C layer reduces the adhesion of ta-C to the Ni substrate under shear loading compared to the single-layer ta-C coating. This is due to differences in the atomic structure of the coating and substrate materials. Figure 4.10 (b) shows the bond density in type III coatings as a function of coating depth. We observe that the bond density is greater in the ta-C layer compared to the a-C layer, due to the higher mass density and average coordination of C atoms in ta-C compared to a-C [38]. Furthermore, we observe that the bond density of ta-C is closer to that of Ni than Si and that the bond density of a-C is closer to that of Si than Ni. Thus, the local atomic structure near the interface is strained more to accommodate bonding between a-C and Ni than between ta-C and Ni, and is strained more to accommodate bonding between ta-C and Si than between a-C and Si. Figure 4.10 (c) shows the deviation from equilibrium of the bond lengths for the interfacial (Ni-C and Si-C) and substrate (Ni-Ni and Si-Si) bonds within 5 Å of the coating-substrate interface for type III coatings (III-A and III-B, respectively) before any external loading has been applied. We observe that the Si-C bond length is independent of t_2 and the deviation from equilibrium of the Si-Si bond length decreases with increasing t_2 except for the case without intermediate a-C layer. In the case of $t_2 = 0$ Å the interfacial strain occurs between Si-C rather than Si-Si bonds. Thus, the substrate is stronger than it would be if the interfacial strain occurred between Si-Si bonds rather than Si-C bonds, and we observe less weakening in the amorphized Si substrate due to the scratch (see Figure 4.9 (b)). We also observe that the Ni-Ni and Ni-C bonds show increasing deviation from their equilibrium bond length with increasing t_2 for type III-A coatings. Thus, the presence of the intermediate a-C layer weakens the adhesion between a ta-C coating and Ni substrate but strengthens that between a ta-C coating and Si substrate. Much experimental data have been obtained for coatings comprised of ta-C and a-C multilayers on a Si substrate, which agrees qualitatively with the behavior we have observed for Si substrates [10,23,25,70–72]. Some authors have studied ta-C and a-C multilayers on metallic substrates including stainless steel and Ti_6Al_4V [71,73], but a decrease in adhesion due to the presence of intermediate a-C layer(s) was not observed in these cases. However, the coatings are orders of magnitude thicker than the coatings in this study, thus, the inclusion of an intermediate a-C layer may improve adhesion of ta-C to Ni substrates by reducing the stress in the coating [10] for thicker coatings and thus with higher intrinsic stress than the coatings modeled in this study.

4.4 Conclusions

We have performed simple shear and tension loading and nanoscratch simulations of ultra-thin multilayer DLC coatings for a range of coating layer thicknesses and coating and substrate compositions including ta-C (70% sp^3 fraction DLC), a-C (30% sp^3 fraction DLC), and a-Si coating layers on crystalline Ni or Si substrates. We have determined the effect of the coating design parameters on the force required to separate the coating from the substrate under shear and tension loading both before and after a scratch and described the mechanisms by which different coating design parameters improve or degrade the adhesion between the coating and the substrate.

We conclude that the presence of an intermediate a-Si layer is critical for improving adhesion of ta-C and a-C coatings to Ni substrates. The bonding between Ni and C atoms at the coating-substrate interface forces the Ni atoms near the interface away from their equilibrium lattice positions and lowers the force necessary to separate layers of Ni atoms in the distorted lattice compared to an undistorted lattice when subjected to shear and tension loading. Thus, DLC coatings without an intermediate a-Si layer fail below the DLC coating in the Ni substrate under both shear and tension loading. Si and Ni form a stable FCC phase near the interface, and bonding of the Si and Ni atoms causes minimal distortion of the Ni lattice. Thus, failure occurs in the intermediate a-Si layer rather than a distorted Ni substrate, and the force necessary to separate the coating from the substrate under shear and tension loading increases when compared to coatings without an intermediate a-Si layer.

Furthermore, we conclude that there is an optimal thickness of the intermediate a-Si layer for improving adhesion of ta-C coatings on Ni substrates. The a-Si layer is softer than the ta-C layer and the Ni substrate, thus, plastic deformation of the a-Si layer during shear loading, tension loading, and scratching increases with increasing thickness of the intermediate a-Si layer. Minimizing the thickness of the intermediate a-Si layer minimizes the amount of a-Si available to plastically deform and forces the critical failure region under shear and tension loading further into the substrate. This increases the force necessary to separate the coating from the substrate, provided enough Si is present to bond to the substrate in place of the DLC and thus prevent distortion of the Ni lattice.

We also conclude that decreasing the hardness and stiffness of the coating by increasing the fraction of the coating comprised of a-Si or a-C and decreasing the fraction comprised of ta-C increases the maximum strain observed in the coating during separation of the coating from the substrate under shear and tensile loading and protects the substrate from damage caused by a scratch. However, the adhesion between the coating and the substrate measured during shear loading as the shear force necessary to separate the coating from the substrate, depends on the atomic structure of the coating and substrate materials. Thus, an intermediate a-C layer improves adhesion of ta-C coatings to Si substrates but not to Ni substrates because the bond density of FCC Ni more closely matches that of ta-C than a-C, and that of crystalline Si more closely matches that of a-C than ta-C.

4.5 References

[1] R. Jacobs, J. Meneve, G. Dyson, D.G. Teer, N.M. Jennett, P. Harris, J. von Stebut, C. Comte, P. Feuchter, A. Cavaleiro, H. Ronkainen, K. Holmberg, U. Beck, G. Reiners, C.D. Ingelbrecht, A certified reference material for the scratch test, Surf. Coatings Technol. 174–175 (2003) 1008–1013, http://dx.doi.org/10.1016/S0257-8972.

[2] S.J. Bull, E.G. Berasetegui, An overview of the potential of quantitative coating adhesion measurement by scratch testing, Tribol. Int. 39 (2006) 99–114, http://dx.doi.org/10.1016/S0167-8922(06)80043-X.

[3] T.H. Zhang, Y. Huan, Nanoindentation and nanoscratch behaviors of DLC coatings on different steel substrates, Compos. Sci. Technol. 65 (2005) 1409–1413, http://dx.doi.org/10.1016/j.compscitech.2004.12.011.

[4] L.Y. Huang, K.W. Xu, J. Lu, B. Guelorget, Nano-scratching process and fracture mechanism of amorphous carbon films, Wear. 254 (2003) 1032–1036, http://dx.doi.org/10.1016/S0043-1648(03)00309-0.

[5] X.G. Ma, K. Komvopoulos, D. Wan, D.B. Bogy, Y.S. Kim, Effects of film thickness and contact load on nanotribological properties of sputtered amorphous carbon thin films, Wear 254 (2003) 1010–1018, http://dx.doi.org/10.1016/S0043-1648(03)00307-7.

[6] P. Bruno, G. Cicala, A.M. Losacco, P. Decuzzi, Mechanical properties of PECVD hydrogenated amorphous carbon coatings via nanoindentation and nanoscratching techniques, Surf. Coatings Technol. 180–181 (2004) 259–264, http://dx.doi.org/10.1016/j.surfcoat.2003.10.035.

[7] N. Yasui, H. Inaba, K. Furusawa, M. Saito, N. Ohtake, Characterization of head overcoat for 1 Tb/in2 magnetic recording, IEEE Trans. Magn. 45 (2009) 805–809, http://dx.doi.org/10.1109/TMAG.2008.2010636.

[8] W.J. MoberlyChan, D.P. Adams, M.J. Aziz, G. Hobler, T. Schenkel, Fundamentals of Focused Ion Beam Nanostructural Processing: Below, At, and Above the

Surface, MRS Bull. 32 (2007) 424–432, http://dx.doi.org/10.1557/mrs2007.66.

[9] P.W. Shum, Z.F. Zhou, K.Y. Li, Optimisation of carbon implantation pre-treatments on the adhesion strength of amorphous carbon coatings on AISI 440C steel substrates, Surf. Coatings Technol. 166 (2003) 213–220, http://dx.doi.org/10.1016/S0257-8972(02)00820-4.

[10] M. Gioti, S. Logothetidis, C. Charitidis, Stress relaxation and stability in thick amorphous carbon films deposited in layer structure, Appl. Phys. Lett. 73 (1998) 184–186, http://dx.doi.org/10.1063/1.121749.

[11] P.J. Fallon, V.S. Veerasamy, C.A. Davis, J. Robertson, G.A.J. Amaratunga, W.I. Milne, J. Koskinen, Properties of filtered-ion-beam-deposited diamondlike carbon as a function of ion energy, Phys. Rev. B. 48 (1993) 4777–4782, http://dx.doi.org/10.1103/PhysRevB.48.4777.

[12] F. Zhao, H.X. Li, L. Ji, Y.F. Mo, W.L. Quan, H.D. Zhou, J.M. Chen, Structural, mechanical and tribological characterizations of a-C : H : Si films prepared by a hybrid PECVD and sputtering technique, J. Phys. D. Appl. Phys. 42 (2009) 165407, http://dx.doi.org/10.1088/0022-3727/42/16/165407.

[13] M. Chhowalla, Y. Yin, G.A.J. Amaratunga, D.R. McKenzie, T. Frauenheim, Highly tetrahedral amorphous carbon films with low stress, Appl. Phys. Lett. 69 (1996) 2344, http://dx.doi.org/10.1063/1.117519.

[14] a. C. Ferrari, B. Kleinsorge, N. a. Morrison, a. Hart, V. Stolojan, J. Robertson, Stress reduction and bond stability during thermal annealing of tetrahedral amorphous carbon, J. Appl. Phys. 85 (1999) 7191, http://dx.doi.org/10.1063/1.370531.

[15] W.-J. Wu, M.-H. Hon, The effect of residual stress on adhesion of silicon-containing diamond-like carbon coatings, Thin Solid Films. 345 (1999) 200–207, http://dx.doi.org/10.1016/S0040-6090(98)01052-9.

[16] M.J. Carey, S. Maat, S. Chandrashekariaih, J.A. Katine, W. Chen, B. York, J.R. Childress, Co2MnGe-based current-perpendicular-to-the-plane giant-magnetoresistance spin-valve sensors for recording head applications, J. Appl. Phys. 109 (2011) 93912, http://dx.doi.org/10.1063/1.3563578.

[17] Y. Pauleau, F. Thièry, V. V. Uglov, V.M. Anishchik, A.K. Kuleshov, M.P. Samtsov, Tribological properties of copper/carbon films formed by microwave plasma-assisted deposition techniques, Surf. Coatings Technol. 180–181 (2004) 102–107, http://dx.doi.org/10.1016/j.surfcoat.2003.10.028.

[18] Y. Pauleau, F. Thièry, Deposition and characterization of nanostructured metal/carbon composite films, Surf. Coatings Technol. 180–181 (2004) 313–322, http://dx.doi.org/10.1016/j.surfcoat.2003.10.077.

[19] A.A. Voevodin, J.S. Zabinski, Supertough wear-resistant coatings with “chameleon” surface adaptation, Thin Solid Films. 370 (2000) 223–231, http://dx.doi.org/10.1016/S0040-6090(00)00917-2.

[20] C. Srisang, P. Asanithi, K. Siangchaew, A. Pokaipisit, P. Limsuwan, Characterization of SiC in DLC/a-Si films prepared by pulsed filtered cathodic arc using Raman spectroscopy and XPS, Appl. Surf. Sci. 258 (2012) 5605–5609, http://dx.doi.org/10.1016/j.apsusc.2012.02.036.

[21] A. a. Voevodin, S.D. Walck, J.S. Zabinski, Architecture of multilayer nanocomposite coatings with super-hard diamond-like carbon layers for wear protection at high contact loads, Wear. 203–204 (1997) 516–527, http://dx.doi.org/10.1016/S0043-1648(96)07425-X.

[22] K.W. Chen, J.F. Lin, The study of adhesion and nanomechanical properties of DLC films deposited on tool steels, Thin Solid Films. 517 (2009) 4916–4920, http://dx.doi.org/10.1016/j.tsf.2009.03.124.

[23] S. Logothetidis, S. Kassavetis, C. Charitidis, Y. Panayiotatos, A. Laskarakis, Nanoindentation studies of multilayer amorphous carbon films, Carbon N. Y. 42 (2004) 1133–1136, http://dx.doi.org/10.1016/j.carbon.2003.12.054.

[24] J. Meneve, E. Dekempeneer, W. Wegener, J. Smeets, Low friction and wear resistant a-C:H/a-$Si_{1-x}C_x$:H multilayer coatings, Surf. Coatings Technol. 86–87 (1996) 617–621, http://dx.doi.org/10.1016/S0257-8972(96)02998-2.

[25] S. Anders, D.L. Callahan, G.M. Pharr, T.Y. Tsui, C. Singh Bhatia, Multilayers of amorphous carbon prepared by cathodic arc deposition, Surf. Coatings Technol. 94–95 (1997) 189–194, http://dx.doi.org/10.1016/S0257-8972(97)00346-0.

[26] L. Wang, S. Wan, S.C. Wang, R.J.K. Wood, Q.J. Xue, Gradient DLC-based nanocomposite coatings as a solution to improve tribological performance of aluminum alloy, Tribol. Lett. 38 (2010) 155–160, http://dx.doi.org/10.1007/s11249-010-9585-5.

[27] K.Y. Li, Z.F. Zhou, C.Y. Chan, I. Bello, C.S. Lee, S.T. Lee, Mechanical and tribological properties of diamond-like carbon films prepared on steel by ECR-CVD process, Diam. Relat. Mater. 10 (2001) 1855–1861, http://dx.doi.org/10.1016/S0925-9635(01)00459-9.

[28] E.J. Sandoz-Rosado, O.A. Tertuliano, E.J. Terrell, An atomistic study of the abrasive wear and failure of graphene sheets when used as a solid lubricant and a comparison to diamond-like-carbon coatings, Carbon N. Y. 50 (2012) 4078–4084, http://dx.doi.org/10.1016/j.carbon.2012.04.055.

[29] J.N. Glosli, M.R. Philpott, J. Belak, Molecular Dynamics Simulation of Mechanical Deformation of Ultra-Thin Amorphous Carbon Films, Mater. Res. Soc. Symp. Proc. 383 (1995) 431–435.

[30] J. Song, S. Lee, J. Lee, C.D. Yeo, Atomic Degradation and Wear of Thin Carbon Films under High-Speed Sliding Contact Using Molecular Dynamics Simulation, Tribol. Lett. 60 (2015), http://dx.doi.org/10.1007/s11249-015-0577-3.

[31] G.T. Gao, P.T. Mikulski, J. a Harrison, Molecular-Scale Trobology of Amorphous Carbon Coatings: Effects of Film Thickness, Adhesion, and Long-Range Interactions, J. Am. Chem. Soc. 124 (2002) 7202–7209.

[32] T.-B. Ma, Y.-Z. Hu, H. Wang, Molecular dynamics simulation of shear-induced graphitization of amorphous carbon films, Carbon N. Y. 47 (2009) 1953–1957, http://dx.doi.org/10.1016/j.carbon.2009.03.040.

[33] L. Pastewka, S. Moser, M. Moseler, Atomistic insights into the running-in, lubrication, and failure of hydrogenated diamond-like carbon coatings, Tribol. Lett. 39 (2010) 49–61, http://dx.doi.org/10.1007/s11249-009-9566-8.

[34] M.I. Baskes, J.E. Angelo, C.L. Bisson, Atomistic calculations of composite interfaces, Model. Simul. Mater. Sci. Eng. 2 (1999) 505–518, http://dx.doi.org/10.1088/0965-0393/2/3A/006.

[35] J.E. Angelo, M.I. Baskes, Interfacial Studies Using the EAM and MEAM, Interface Sci. 63 (1996) 47–63, http://dx.doi.org/10.1007/BF00200838.

[36] T. Iwasaki, H. Miura, Molecular dynamics analysis of adhesion strength of interfaces between thin films, J. Mater. Res. 16 (2001) 1789–1794, http://dx.doi.org/10.1557/PROC-594-377.

[37] T.H. Fang, J.H. Wu, Molecular dynamics simulations on nanoindentation mechanisms of multilayered films, Comput. Mater. Sci. 43 (2008) 785–790, http://dx.doi.org/10.1016/j.commatsci.2008.01.066.

[38] J. Robertson, Diamond-like amorphous carbon, Mater. Sci. Eng. R Reports. 37 (2002) 129–281, http://dx.doi.org/10.1016/S0927-796X(02)00005-0.

[39] V. Prabhakaran, F.E. Talke, Wear and hardness of carbon overcoats on magnetic recording sliders, Wear. 243 (2000) 18–24, http://dx.doi.org/10.1016/S0043-1648(00)00392-6.

[40] D. Song, R. Kvitek, D. Schnur, Inspection of pole tip diamondlike carbon wear due to heater-induced head-disc contact, J. Appl. Phys. 99 (2006) 2004–2007, http://dx.doi.org/10.1063/1.2176308.

[41] H. Deng, K.M. Minor, J. a. Barnard, Comparison of mechanical and tribological properties of permalloy and high moment fetan thin films for tape recording heads, IEEE Trans. Magn. 32 (1996) 3702–3704, http://dx.doi.org/10.1109/20.538809.

[42] Z. Ma, S. Long, Y. Pan, Y. Zhou, Creep Behavior and Its Influence on the Mechanics of Electrodeposited Nickel Films, J. Mater. Sci. Technol. 25 (2009) 90–

94, http://dx.doi.org/10.3321/j.issn:1005-0302.2009.01.012 %W 北京万方数据股份有限公司.

[43] C.P. Frick, B.G. Clark, S. Orso, a. S. Schneider, E. Arzt, Size effect on strength and strain hardening of small-scale [1 1 1] nickel compression pillars, Mater. Sci. Eng. A. 489 (2008) 319–329, http://dx.doi.org/10.1016/j.msea.2007.12.038.

[44] E. Klokholm, J. a. Aboaf, The saturation magnetostriction of permalloy films, J. Appl. Phys. 52 (1981) 2474–2476, http://dx.doi.org/10.1063/1.328971.

[45] M.I. Baskes, Modified embedded-atom potentials for cubic materials and impurities, Phys. Rev. B. 46 (1992) 2727–2742, http://dx.doi.org/10.1103/PhysRevB.46.2727.

[46] W. Xiao, M.I. Baskes, K. Cho, MEAM study of carbon atom interaction with Ni nano particle, Surf. Sci. 603 (2009) 1985–1998, http://dx.doi.org/10.1016/j.susc.2009.03.009.

[47] J. Tersoff, New empirical model for the structural properties of silicon, Phys. Rev. Lett. 56 (1986) 632–635, http://dx.doi.org/10.1103/PhysRevLett.56.632.

[48] W.C.D. Cheong, L.C. Zhang, Molecular dynamics simulation of phase transformations in silicon monocrystals due to nano-indentation, Nanotechnology. 11 (2000) 173–180, http://dx.doi.org/10.1088/0957-4484/11/3/307.

[49] S. Plimpton, Fast Parallel Algorithms for Short-Range Molecular Dynamics, J. Comput. Phys. 117 (1995) 1–19, http://dx.doi.org/10.1006/jcph.1995.1039.

[50] N. Wang, K. Komvopoulos, Nanomechanical and friction properties of ultrathin amorphous carbon films studied by molecular dynamcs analysis, in: STLE/ASME 2010 Int. Jt. Tribol. Conf., 2010: pp. 393–395.

[51] a. Noreyan, J.G. Amar, Molecular dynamics simulations of nanoscratching of 3C SiC, Wear. 265 (2008) 956–962, http://dx.doi.org/10.1016/j.wear.2008.02.020.

[52] Y. Gao, C. Lu, N.N. Huynh, G. Michal, H.T. Zhu, a. K. Tieu, Molecular dynamics simulation of effect of indenter shape on nanoscratch of Ni, Wear. 267 (2009) 1998–2002, http://dx.doi.org/10.1016/j.wear.2009.06.024.

[53] R. Wood, Future hard disk drive systems, J. Magn. Magn. Mater. 321 (2009) 555–561, http://dx.doi.org/10.1016/j.jmmm.2008.07.027.

[54] R. Komanduri, N. Chandrasekaran, L.M. Raff, MD simulation of indentation and scratching of single crystal aluminum, Wear. 240 (2000) 113–143, http://dx.doi.org/10.1016/S0043-1648(00)00358-6.

[55] Y. Yan, T. Sun, S. Dong, Y. Liang, Study on effects of the feed on AFM-based nano-scratching process using MD simulation, Comput. Mater. Sci. 40 (2007) 1–5,

http://dx.doi.org/10.1016/j.commatsci.2006.10.020.

[56] Y.C. Liang, J.X. Chen, M.J. Chen, Y.L. Tang, Q.S. Bai, Integrated MD simulation of scratching and shearing of 3D nanostructure, Comput. Mater. Sci. 43 (2008) 1130–1140, http://dx.doi.org/10.1016/j.commatsci.2008.03.012.

[57] Q.K. Li, M. Li, Atomic scale characterization of shear bands in an amorphous metal, Appl. Phys. Lett. 88 (2006) 98–101, http://dx.doi.org/10.1063/1.2212059.

[58] X.W. Zhou, J.A. Zimmerman, E.D. Reedy, N.R. Moody, Molecular dynamics simulation based cohesive surface representation of mixed mode fracture, Mech. Mater. 40 (2008) 832–845, http://dx.doi.org/10.1016/j.mechmat.2008.05.001.

[59] T. Sato, T. Saito, S. Fujita, Mechanism of Diamond-Like Carbon (DLC) Delamination under Rolling Contact Condition, Tribol. Online. 3 (2008) 337–341, http://dx.doi.org/10.2474/trol.3.337.

[60] M.R. Price, A. Ovcharenko, R. Thangaraj, B. Raeymaekers, Deformation of Ultra-Thin Diamond-Like Carbon Coatings Under Combined Loading on a Magnetic Recording Head, Tribol. Lett. 57 (2015) 3:1-9, http://dx.doi.org/10.1007/s11249-014-0449-2.

[61] H. Holleck, V. Schier, Multilayer PVD coatings for wear protection, Surf. Coatings Technol. 76–77 (1995) 328–336, http://dx.doi.org/10.1016/0257-8972(95)02555-3.

[62] G. Voronoi, Nouveles applications des parametres continus a la theorie des formes quadratiques, J. Reine. Angew. Math. 134 (1908) 198–287, http://dx.doi.org/10.1515/crll.1909.136.67.

[63] W. Yang, S. Rehman, X. Chu, Y. Hou, S. Gao, Transition Metal (Fe, Co and Ni)Carbide and Nitride Nanomaterials:S tructure, Chemical Synthesis and Applications, ChemNanoMat. 13 (2015) 76–398, http://dx.doi.org/10.1002/cnma.201500073.

[64] Z.L. Schaefer, K.M. Weeber, R. Misra, P. Schiffer, R.E. Schaak, Bridging hcp-Ni and Ni3C via a Ni3C 1-x solid solution: Tunable composition and magnetism in colloidal nickel carbide nanoparticles, Chem. Mater. 23 (2011) 2475–2480, http://dx.doi.org/10.1021/cm200410s.

[65] M.R. Price, A. Ovcharenko, B. Raeymaekers, Qualitative Evaluation of Ultra-thin Multi-layer Diamond-Like Carbon Coatings Using Molecular Dynamics Nanoindentation Simulations, Tribol. Lett. 62 (2016) 1–10, http://dx.doi.org/10.1007/s11249-016-0655-1.

[66] D.M. Follstaedt, J. a. Knapp, S.M. Myers, Mechanical properties of ion-implanted amorphous silicon, J. Mater. Res. 19 (2004) 338–346, http://dx.doi.org/10.1557/jmr.2004.19.1.338.

[67] C. Casiraghi, J. Robertson, A.C. Ferrari, Diamond-like carbon for data and beer storage, Mater. Today. 10 (2007) 44–53, http://dx.doi.org/10.1016/S1369-7021(06)71791-6.

[68] J. Veverkova, S. V. Hainsworth, Effect of temperature and counterface on the tribological performance of W-DLC on a steel substrate, Wear. 264 (2008) 518–525, http://dx.doi.org/10.1016/j.wear.2007.04.003.

[69] K.L. Choy, E. Felix, Functionally graded diamond-like carbon coatings on metallic substrates, Mater. Sci. Eng. a-Structural Mater. Prop. Microstruct. Process. 278 (2000) 162–169, http://dx.doi.org/10.1016/S0921-5093(99)00569-9.

[70] C. Charitidis, S. Logothetidis, M. Gioti, A comparative study of the nanoscratching behavior of amorphous carbon films grown under various deposition conditions, Surf. Coatings Technol. 125 (2000) 201–206, http://dx.doi.org/10.1016/S0257-8972(99)00546-0.

[71] S. Zhang, X.L. Bui, Y. Fu, D.L. Butler, H. Du, Bias-graded deposition of diamond-like carbon for tribological applications, Diam. Relat. Mater. 13 (2004) 867–871, http://dx.doi.org/10.1016/j.diamond.2003.10.043.

[72] C. Mathioudakis, P. Kelires, Y. Panagiotatos, P. Patsalas, C. Charitidis, S. Logothetidis, Nanomechanical properties of multilayered amorphous carbon structures, Phys. Rev. B. 65 (2002) 1–14, http://dx.doi.org/10.1103/PhysRevB.65.205203.

[73] D.R. McKenzie, R.N. Tarrant, M.M.M. Bilek, T. Ha, J. Zou, W.E. McBride, D.J.H. Cockayne, N. Fujisawa, M. V. Swain, N.L. James, J.C. Woodard, D.G. McCulloch, Multilayered carbon films for tribological applications, Diam. Relat. Mater. 12 (2003) 178–184, http://dx.doi.org/10.1016/S0925-9635(03)00020-7.

CHAPTER 5

CONCLUSIONS AND FUTURE WORK

5.1 Conclusions

Based on the results of the MD simulations of a multilayer DLC coating consisting of stacked layers of DLC and a-Si on a Ni substrate documented in this dissertation, we draw the following conclusions:

1. We conclude that the hardness and Young's modulus of a multilayer DLC coating increases with increasing DLC layer thickness and decreasing a-Si layer thickness, similar to experimental results documented in the literature. DLC and a-Si are the hardest and softest material layers of the multilayer coating, respectively, and increasing the thickness of either layer increases its fraction of the total thickness of the multilayer coating, thus affecting its mechanical properties.
2. Furthermore, we observe that external loading causes plastic deformation that occurs preferentially in the softest material layers. Thus, for constant coating thickness and external loading, plastic deformation of the Ni substrate increases with decreasing a-Si layer thickness because there is less a-Si present to plastically deform, and thus, plastic deformation of the Ni substrate is increasingly preferential to plastic deformation of the coating. However, the presence of an a-Si layer is critical for improving the adhesion of a DLC coating to a Ni substrate and thus, an optimum thickness of the a-Si layer exists. In the absence of an a-Si layer, the bonding between Ni and C atoms at the coating-substrate interface forces the Ni atoms near the interface away from their equilibrium lattice positions and lowers the force necessary to separate layers of Ni atoms in the distorted lattice compared to an undistorted

lattice when subjected to shear and tension loading. When an intermediate a-Si layer is present, the Ni and Si atoms form a stable FCC phase near their interface, greatly reducing the distortion of the Ni lattice in the substrate and increasing the force necessary to separate neighboring atomic layers compared to the Ni-C interface. However, because of the low hardness of a-Si compared to DLC and Ni and the increase in plastic deformation due to external loading that occurs in the a-Si layer with increasing thickness, minimizing the thickness of the intermediate a-Si layer minimizes the amount of a-Si available to plastically deform and forces the critical failure region under shear and tension loading from the a-Si layer into the undistorted Ni substrate. This increases the force necessary to separate the coating from the substrate, provided enough Si is present to bond to the substrate in place of the DLC and thus, prevent distortion of the Ni lattice.

3. Plastic deformation of the Ni substrate increases with increasing sp^3 fraction of the DLC layer. Increasing hardness of the DLC layer causes plastic deformation to be increasingly preferential to the material layers below the DLC layer, and the DLC layer bends like a plate into the plastically deformed a-Si layer and Ni substrate. Hence, to prevent plastic deformation of the substrate, the fraction of the coating comprised of a-Si should be increased or the hardness of the DLC layer should be decreased, for instance by decreasing its fraction of sp^3 hybridized carbon-carbon bonds. This will cause the coating rather than the substrate to deform plastically under mechanical loading.

4. Plastic deformation of the Ni substrate decreases for a coating consisting of stacked layers of ta-C (70% sp^3 fraction DLC) and a-C (30% sp^3 fraction DLC) compared to a single-layer coating of ta-C of the same thickness under identical loading. However, increasing the plastic deformation of the coating by decreasing its hardness may degrade its wear resistance and thus, a balance exists between obtaining the desired hardness and Young's modulus to decrease wear of the coating, and minimizing the plastic deformation of the substrate under mechanical loading.
5. Adhesion between the coating and substrate, measured as the shear force necessary to separate the coating from the substrate, is more significantly affected by the atomic structure of the materials that comprise the coating and substrate layers than the mechanical properties of the coating and substrate materials. We observe that less strain is required to compensate for bonding between ta-C and Ni than between a-C and Ni, and less strain is required to compensate for bonding between a-C and Si than between ta-C and Si. Thus, an intermediate a-C layer improves adhesion of ta-C coatings to Si substrates but not to Ni substrates because the bond density of FCC Ni more closely matches that of ta-C than a-C, and that of crystalline Si more closely matches that of a-C than ta-C.

5.2 Future work

Several avenues of future work may be useful for further validating and expanding upon the results and conclusions presented in this dissertation. These avenues include modeling a wider range of materials, design parameters, and loading conditions, experimentally validating the behaviors predicted by the MD simulations, and expanding the length and time scales of the simulations.

5.2.1 Materials, design parameters, and loading conditions

We have investigated the effect of coating design parameters, including number of layers, layer thickness, layer composition, and DLC *sp*^{3} fraction on the resistance of an ultra-thin multilayer DLC coating to plastic deformation and delamination. However, a greater range over those design parameters or modeling the effect of additional design parameters would expand the range of coatings to which these results are applicable. For example, we have modeled only a small subset of materials and their combinations as substrate and coating layers, and a larger selection of materials used as coating layers would allow one to determine which design recommendations from this study are applicable to DLC coatings with different substrates or intermediate adhesion layers, and what additional deformation mechanisms might play an important role in those coatings. The primary challenge that must be overcome when modeling additional materials is the development of multicomponent interatomic potential parameters for the desired chemical interactions, or limiting the study to the cases for which those parameters have already been developed. With greater computational resources, larger volumes could be modeled, allowing one to model thicker coatings or the effect of additional coating layers.

In addition to expanding the range of design parameters modeled, one could investigate the effect of crystal defects including voids, dislocations, grain boundaries, and impurities on a coating’s mechanical properties and deformation mechanisms. Modeling crystal defects such as voids, dislocations, and grain boundaries can be done without the need for additional interatomic potential parameters, as has been described by others [1–4]; furthermore, preliminary simulations that we ran with randomly-located voids in the Ni substrate showed a negligible effect on the simulation results for defect densities similar to those reported to us experimentally by our collaborators at Western Digital Corp., but a more rigorous study could be implemented. However, modeling grain boundaries would require modeling only the region near the grain boundary, modeling very small grains, or would require a much larger simulation volume and thus much more computation (see, e.g., [5,6]). Finally, modeling impurities, as with adding layers of different material to the simulation, is often limited by the choice of multicomponent interatomic potential parameters available.

Additionally, surface effects such as surface roughness, atomic structure of the outermost atomic layers near the surface, the presence of lubricant, and lubricant design parameters have all been shown to be significant in determining the behavior of ultra-thin coatings when contacting another body [7,8]. We negate these effects by ensuring the surfaces of the DLC coatings compared in this study are equivalent to each other, but have not attempted to explain their effect on the mechanical properties or behavior of the coating under external loading, except to quantify uncertainty in hardness and Young's modulus as described in Chapter 2. These considerations would be particularly important if attempting to model wear mechanisms of DLC coatings.

Furthermore, although we have simulated a range of external loading conditions of the DLC coating, these loading conditions were chosen to characterize the coating in a specific way, e.g. nanoindentation, or to represent a load experienced by a multilayer DLC coating in an HDD. Other loading conditions may more accurately represent loads experienced by DLC coatings in different engineering applications, and thus, could be modeled in order to verify the applicability of the conclusions of this study for the desired application.

5.2.2 Experimental validation

Although the primary motivation for this work is the difficulty of experimentally obtaining the desired results, we have compared our results to similar experimental results where possible, as well as to previously-published MD results, and observed good qualitative agreement and where data are directly comparable, good quantitative agreement. However, the previous studies to which we have compared our results are often results from simulations with coatings comprised of different materials, or from experiments on coatings at different time and length scales compared to our simulations. Thus, additional experimental results from coatings equivalent to the coatings modeled in this study would be greatly beneficial in further validating the results and conclusions we have shown. Yu et al. [9] developed a load-displacement transducer with 0.5 Å displacement resolution and 3-nm force resolution for performing nanoindentation and nanoscratch tests, which has been used to perform indentations as small as 1 nm deep by Lee et al. [10]. They characterized multilayer DLC coatings on magnetic disks, and measured the mechanical properties as a function of indentation depth but not for different coatings to evaluate the effect of coating design parameters. Using a similar experimental setup, it would be possible to perform nanoindentation and nanoscratch experiments on coatings that match as closely as possible the coatings evaluated in this study, which would involve using either actual HDD recording heads or depositing coatings of desired composition and thickness directly on Ni and Si substrates. However, although nanoindentation and nanoscratch results can indicate a coating's wear resistance, wear tests should also be performed in cases for which wear is a concern [10]. Lee et al. [10], Miyake et al. [11], and Yasui et al. [12] describe using nanoindenter or AFM tools to perform wear tests of thin films, although when performing wear tests on hard-on-soft coatings with large hardness mismatch between material layers, such as on HDD recording heads, deformation may occur as wear of the coating or by bending the coating into a soft substrate. Thus, one must ensure that the maximum load is selected such that plastic deformation of the substrate is avoided.

Finally, to validate the effect of coating design parameters on the adhesion of the coating to the substrate observed in this study, nanoscratch experiments could be performed on coatings equivalent to those modeled in this study. A relevant study was published by Yasui et al. [12], who performed nanoscratch experiments of ultra-thin single-layer DLC coatings on Ni and Si substrates. One would have to modify their procedure to create multilayer DLC coatings with intermediate a-Si or a-C layers. Additionally, they identified a critical load at coating failure, but did not characterize how the coatings failed, hence, additional postscratch surface characterization steps should be taken to determine if the coatings failed by delamination, cracking, or some other mechanism(s).

5.2.3 Larger-scale simulations

The largest simulations presented in this study had a maximum size of 26 nm or less in each dimension and the longest time scale simulated was approximately 1 ns. These are near the practical limits of MD simulation using today's available supercomputer resources, although some multimillion atom MD simulations have been achieved [13], and even larger simulations can be done with greatly simplified material models, e.g. by using short-range pairwise interatomic potentials [14]. Much longer time scales can be simulated using specialized hardware, software, and integration algorithms [15,16]. However, fully modeling deformation and delamination of ultra-thin multilayer DLC coatings when indented, scratched, or loaded by realistic bodies requires larger length scales and longer time scales than is currently feasible using MD. Multiscale modeling techniques, such as coarse-graining [17], extended finite-element-analysis [18], and internal state variable theory [19], could thus be used to model loading conditions at more realistic scales while still modeling important atomistic behaviors such as bond-breaking at delaminated material interfaces, local atomic rearrangement near indenter-coating contact, or crystal defects and dislocation motion in the crystalline substrate.

5.3 References

[1] Cheng D., Yan Z. J., and Yan L., 2007, "Misfit Dislocation Network in Cu/Ni Multilayers and Its Behaviors During Scratching," Thin Solid Films, **515**(7–8), pp. 3698–3703.

[2] Zhou X. W., and Wadley H. N. G., 2004, "Misfit Dislocations in Gold/Permalloy Multilayers," Philos. Mag., **84**(2), pp. 193–212.

[3] Shao S., and Medyanik S. N., 2010, "Dislocation-Interface Interaction in Nanoscale FCC Metallic Bilayers," Mech. Res. Commun., **37**(3), pp. 315–319.

[4] Hasnaoui a., Derlet P. M., and Van Swygenhoven H., 2004, "Interaction Between Dislocations and Grain Boundaries Under An Indenter – a Molecular Dynamics Simulation," Acta Mater., **52**(8), pp. 2251–2258.

[5] Ma X.-L., and Yang W., 2003, "Molecular Dynamics Simulation on Burst and Arrest of Stacking Faults in Nanocrystalline Cu Under Nanoindentation," Nanotechnology, **14**(11), pp. 1208–1215.

[6] Saraev D., and Miller R. E., 2005, "Atomistic Simulation of Nanoindentation Into Copper Multilayers," Model. Simul. Mater. Sci. Eng., **13**(7), pp. 1089–1099.

[7] Szlufarska I., Chandross M., and Carpick R. W., 2008, "Recent Advances in

Single-Asperity Nanotribology," J. Phys. D. Appl. Phys., **41**(12), p. 123001.

[8] Marchon B., 2009, "Lubricant Design Attributes For Subnanometer Head-Disk Clearance," IEEE Trans. Magn., **45**(2), pp. 872–876.

[9] Yu N., Bonin W. A., and Polycarpou A. A., 2005, "High-Resolution Capacitive Load-Displacement Transducer and Its Application in Nanoindentation and Adhesion Force Measurements," Rev. Sci. Instrum., **76**(4).

[10] Lee K. M., Yeo C. D., and Polycarpou a. a., 2007, "Nanomechanical Property and Nanowear Measurements for Sub-10-nm Thick Films in Magnetic Storage," Exp. Mech., **47**(1), pp. 107–121.

[11] Miyake S., Saito T., Wang M., and Watanabe S., 2006, "Tribological Properties of Extremely Thin Protective Carbon Nitride Films Deposited on Magnetic Discs by Complex Treatment," J. Eng. Tribol., **220**(7), pp. 587–595.

[12] Yasui N., Inaba H., Furusawa K., Saito M., and Ohtake N., 2009, "Characterization of Head Overcoat For 1 Tb/in^2 Magnetic Recording," IEEE Trans. Magn., **45**(2), pp. 805–809.

[13] Walsh P., Omeltchenko A., Kalia R. K., Nakano A., Vashishta P., and Saini S., 2003, "Nanoindentation of Silicon Nitride: a Multimillion-Atom Molecular Dynamics Study," Appl. Phys. Lett., **82**(1), pp. 118–120.

[14] Glaser J., Nguyen T. D., Anderson J. A., Lui P., Spiga F., Millan J. A., Morse D. C., and Glotzer S. C., 2015, "Strong Scaling of General-Purpose Molecular Dynamics Simulations on GPUs," Comput. Phys. Commun., **192**, pp. 97–107.

[15] Krieger E., and Vriend G., 2015, "New Ways to Boost Molecular Dynamics Simulations," J. Comput. Chem., **36**(13), pp. 996–1007.

[16] Shaw D. E., Grossman J. P., Bank J. A., Batson B., Butts J. A., Chao J. C., Deneroff M. M., Dror R. O., Even A., Fenton C. H., Forte A., Gagliardo J., Gill G., Greskamp B., Ho C. R., Ierardi D. J., Iserovich L., Kuskin J. S., Larson R. H., Layman T., Lee L. S., Lerer A. K., Li C., Killebrew D., Mackenzie K. M., Mok S. Y. H., Moraes M. A., Mueller R., Nociolo L. J., Peticolas J. L., Quan T., Ramot D., Salmon J. K., Scarpazza D. P., Ben Schafer U., Siddique N., Snyder C. W., Spengler J., Tang P. T. P., Theobald M., Toma H., Towles B., Vitale B., Wang S. C., and Young C., 2014, "Raising the Bar For Performance and Programmability in a Special-Purpose Molecular Dynamics Supercomputer," International Conference for High Performance Computing, Networking, Storage and Analysis.

[17] Budarapu P. R., Gracie R., Yang S. W., Zhuang X., and Rabczuk T., 2014, "Efficient Coarse Graining in Multiscale Modeling of Fracture," Theor. Appl. Fract. Mech., **69**, pp. 126–143.

[18] Talebi H., Silani M., Bordas S. P. A., Kerfriden P., and Rabczuk T., 2014, "A

Computational Library For Multiscale Modeling of Material Failure," Comput. Mech., **53**(5), pp. 1047–1071.

[19] Spearot D. E., Jacob K. I., and McDowell D. L., 2004, "Non-Local Separation Constitutive Laws For Interfaces and Their Relation to Nanoscale Simulations," Mech. Mater., **36**(9), pp. 825–847.

APPENDIX

INTERATOMIC POTENTIAL PARAMETERS

Table A.1 Tersoff potential parameters used in this study. All values are taken directly from [1,2] and as implemented in LAMMPS [3], except for the underlined entries which were added for this study.

3-body interaction	m	γ	λ_3	c	d	$\cos\theta_0$	n	β	λ_2	B	R	D	λ_1	A
C-C-C	3.0	1.0	0.0	38049	4.3484	-0.57058	0.72751	1.5724e-7	2.2119	346.7	1.95	0.15	3.4879	1393.6
Si-Si-Si	3.0	1.0	0.0	100390	16.217	-0.59825	0.78734	1.1e-6	1.7322	471.18	2.85	0.15	2.4799	1830.8
Si-Si-C	3.0	1.0	0.0	100390	16.217	-0.59825	0.0*	0.0*	0.0*	0.0*	2.36	0.15	0.0*	0.0*
Si-C-C	3.0	1.0	0.0	100390	16.217	-0.59825	0.78734	1.1e-6	1.9721	395.13	2.36	0.15	2.9839	1597.3
C-Si-Si	3.0	1.0	0.0	38049	4.3484	-0.57058	0.72751	1.5724e-7	1.9721	395.13	2.36	0.15	2.9839	1597.3
C-Si-C	3.0	1.0	0.0	38049	4.3484	-0.57058	0.0*	0.0*	0.0*	0.0*	1.95	0.15	0.0*	0.0*
C-C-Si	3.0	1.0	0.0	38049	4.3484	-0.57058	0.0*	0.0*	0.0*	0.0*	2.36	0.15	0.0*	0.0*
Si-C-Si	3.0	1.0	0.0	100390	16.217	-0.59825	0.0*	0.0*	0.0*	0.0*	2.85	0.15	0.0*	0.0*
Si-Si-Ni	3.0	1.0	0.0	100390	16.217	-0.59285	0.0*	0.0*	0.0*	0.0*	2.85	0.15	0.0*	0.0*
C-C-Ni	3.0	1.0	0.0	38049	4.3484	-0.57058	0.0*	0.0*	0.0*	0.0*	2.36	0.15	0.0*	0.0*
Si-C-Ni	3.0	1.0	0.0	100390	16.217	-0.59825	0.0*	0.0*	0.0*	0.0*	2.85	0.15	0.0*	0.0*
C-Si-Ni	3.0	1.0	0.0	38049	4.3484	-0.57058	0.0*	0.0*	0.0*	0.0*	2.36	0.15	0.0*	0.0*
Remaining†	3.0	1.0	0.0	1.0	1.0	-0.59825	0.0	0.0	0.0	0.0	2.85	0.15	0.0	0.0

* 2-body interactions are defined in LAMMPS using the data from the entry in which the second and third elements are equivalent, e.g. Si-Si pair terms are defined using the entry for Si-Si-Si and, thus, n, β, λ_2, B, λ_1, and A are ignored for the Si-Si-C and Si-Si-Ni entries, etc.

† 27 distinct 3-body interaction types are possible for a 3-component system and must therefore be defined in LAMMPS. All remaining entries involve Ni pair interactions and are set to zero by setting $A = 0$ and $B = 0$. Thus, the other parameters have no effect and can be set arbitrarily.

Table A.2 AIREBO potential parameters used in this study that were set to 0 to remove C-C pair interactions. All remaining parameter values are unchanged compared to [4] and as implemented in LAMMPS [3].

AIREBO parameter	Original value	Modified value
A_CC	10953.54	0
BIJc_CC1	12388.79	0
BIJc_CC2	17.5674	0
BIJc_CC3	30.7149	0
epsilon_CC	0.0028437	0
epsilon_CCCC	0.307885	0
epsilon_CCCH	0.178660	0
epsilon_HCCH	0.124975	0

Table A.3 MEAM potential parameters used in this study for individual elements. Two parameterizations of Ni are shown, one that has been parameterized for Ni-Si interactions [5] and is used for the coating models with DLC, Si, and Ni, and another that has been parameterized for Ni-C interactions [6] and is used for the coating models without Si.

Element	*lat*	z	Z	m	α	b_0	b_1	b_2	b_3	a	E_0	A_0	t_0	t_1	t_2	t_3	ρ_0	i
Ni (Ni-Si)	‘fcc’	12	28	58.71	4.99	2.45	2.20	6.0	2.20	3.52	4.45	1.10	1	3.57	1.60	2.70	1	0
Ni (Ni-C)	‘fcc’	12	28	58.71	4.99	2.45	1.50	6.0	1.50	3.52	4.45	1.10	1	5.79	1.60	3.70	1	0
Si	‘dia’	4	14	28.086	4.87	4.40	5.50	5.5	5.50	5.43	0	0	1	3.13	4.47	-1.80	1	0
C	‘dia’	4	6	12.011	4.20	4.20	4.20	4.8	4.18	3.57	0	0	1	4.50	0.45	-3.80	6	0

Table A.4 MEAM potential parameters used in this study for multicomponent systems. The notation (1) or (2) indicates MEAM parameter values that replace the respective single-element parameter value from Table A3. The notation (1,2) indicates terms for the cross-species pairwise interactions between elements 1

Components	Element 1	Element 2	ρ_0 (1)	ρ_0 (2)	E_c (1,2)	α (1,2)	r_e (1,2)	*lat* (1,2)	Screening parameters*		
									Elements	C_{min}	C_{max}
Ni-Si [5]	Ni	Si	1	1	4.855	6.00	2.408	‘l12’	(1,1,2)	0.36	2.8
									(2,2,1)	1.21	2.8
									(1,2,2)	0.7225	2.8
									(1,2,1)	0.7225	2.8
Ni-C [6]	Ni	C	1	1	4.9438	4.921	2.04	‘b1’	(2,2,2)	0.8	2.8

* The 3-body terms not shown have $C_{min} = 2.0$ and $C_{max} = 2.8$

A.1 References

[1] Tersoff J., 1989, "Modeling Solid-State Chemistry: Interatomic Potentials For Multicomponent Systems," Phys. Rev. B, **39**(8), pp. 5566–5568.

[2] Tersoff J., 1990, "Erratum: Modeling Solid-State Chemistry: Interatomic Potentials For Multicomponent Systems," Phys. Rev. B, **41**(5), p. 3248.

[3] Plimpton S., 1995, "Fast Parallel Algorithms for Short-Range Molecular Dynamics," J. Comput. Phys., **117**(1), pp. 1–19.

[4] Stuart S., Tutein A., and Harrison J., 2000, "A Reactive Potential For Hydrocarbons with Intermolecular Interactions," J. Chem. Phys., **112**(14), pp. 6472–6486.

[5] Baskes M. I., Angelo J. E., and Bisson C. L., 1999, "Atomistic Calculations of Composite Interfaces," Model. Simul. Mater. Sci. Eng., **2**, pp. 505–518.

[6] Xiao W., Baskes M. I., and Cho K., 2009, "MEAM Study of Carbon Atom Interaction with Ni Nano Particle," Surf. Sci., **603**(13), pp. 1985–1998.